

BOSTON UNIVERSITY
COLLEGE OF ENGINEERING

Dissertation

**OPTICAL MIMO COMMUNICATION SYSTEMS UNDER
ILLUMINATION CONSTRAINTS**

by

PANKIL M. BUTALA

B.E., University of Mumbai, 2006
M.S., University of California, Los Angeles, 2007

Submitted in partial fulfillment of the

requirements for the degree of

Doctor of Philosophy

2015

© 2015 by
PANKIL M. BUTALA
All rights reserved

Approved by

First Reader

Thomas D.C. Little, Ph.D.
Professor of Electrical and Computer Engineering
Professor of Systems Engineering

Second Reader

Jeffrey Carruthers, Ph.D.
Associate Professor of Electrical and Computer Engineering

Third Reader

Bobak Nazer, Ph.D.
Assistant Professor of Electrical and Computer Engineering
Assistant Professor of Systems Engineering

Fourth Reader

Valencia Joyner Koomson, Ph.D.
Associate Professor of Electrical and Computer Engineering
Tufts University

“ Δv - v for velocity, Δ for change. In space, this is the measure of change in velocity required to get from one place to another, thus a measure of the energy required to do it. Everything is moving already but to get something from the moving surface of the Earth into orbit around it requires a minimum Δv of 10 km/s. To leave Earth’s orbit and fly to Mars requires a minimum Δv of 3.6 km/s and to orbit Mars and land on it requires a Δv of about 1 km/s. The hardest part is leaving Earth behind, for that is by far the deepest gravity well involved.”

Kim Stanley Robinson
Red Mars (2.2.99)

Acknowledgments

Dad, Mom and Anuja – This work is as much your accomplishment as mine because of your numerous sacrifices, unconditional love and support.

Prof. Little – You have been a wonderful mentor throughout my doctoral studies. Your constant advice, guidance and support has been invaluable from inception to completion of this dissertation.

Dr. Elgala – Your constructive criticism and discussion have helped me effectively shape my research ideas.

Prof. Carruthers, Prof. Nazer and Prof. Koomson – Your review and feedback has enriched this dissertation.

This work was supported primarily by the Engineering Research Centers Program of the National Science Foundation under NSF Cooperative Agreement No. EEC-0812056.

Thank you,
Pankil

OPTICAL MIMO COMMUNICATION SYSTEMS UNDER ILLUMINATION CONSTRAINTS

PANKIL M. BUTALA

Boston University, College of Engineering, 2015

Major Professor: Thomas D.C. Little, Ph.D.

Professor of Electrical and Computer Engineering
Professor of Systems Engineering

ABSTRACT

Technology for wireless information access has enabled innovation of ‘smart’ portable consumer devices. These have been widely adopted and have become an integral part of our daily lives. They need ubiquitous connectivity to the internet to provide value added services, maximize their functionality and create a smarter world to live in. Cisco’s visual networking index currently predicts wireless data consumption to increase by 61% per year. This will put additional stress on the already stressed wireless access network infrastructure creating a phenomenon called ‘spectrum crunch’.

At the same time, the solid state devices industry has made remarkable advances in energy efficient light-emitting-diodes (LED). The lighting industry is rapidly adopting LEDs to provide illumination in indoor spaces. Lighting fixtures are positioned to support human activities and thus are well located to act as wireless access points. The visible spectrum (380 nm – 780 nm) is yet unregulated and untapped for wireless access. This provides unique opportunity to upgrade existing lighting infrastructure and create a dense grid of small cells by using this additional ‘optical’ wireless bandwidth. Under the above model, lighting fixtures will service dual missions of

illumination and access points for optical wireless communication (OWC).

This dissertation investigates multiple-input multiple-output (MIMO) optical wireless broadcast system under unique constraints imposed by the optical channel and illumination requirements. Sample indexed spatial orthogonal frequency division multiplexing (SIS-OFDM) and metameric modulation (MM) are proposed to achieve higher spectral efficiency by exploiting dimensions of space and color respectively in addition to time and frequency. SIS-OFDM can provide significant additional spectral efficiency of up to $(N_{sc}/2 - 1) \times k$ bits/symbol where N_{sc} is total number of subcarriers and k is number of bits per underlying spatial modulation symbol. MM always generates the true requested illumination color and has the potential to provide better color rendering by incorporating multiple LEDs. A normalization framework is then developed to analyze performance of optical MIMO imaging systems. Performance improvements of up to 45 dB for optical systems have been achieved by decorrelating spatially separate links by incorporating an imaging receiver. The dissertation also studies the impact of visual perception on performance color shift keying as specified in IEEE 802.15.7 standard. It shows that non-linearity for a practical system can have a performance penalty of up to 15 dB when compared to the simplified linear system abstraction as proposed in the standard. Luminous-signal-to-noise ratio, a novel metric is introduced to compare performance of optical modulation techniques operating at same illumination intensity. The dissertation then introduces singular value decomposition based OWC system architecture to incorporate illumination constraints independent of communication constraints in a MIMO system. It then studies design paradigm for a multi-colored wavelength division multiplexed indoor OWC system.

Contents

1	Introduction	1
1.1	Motivation	1
1.2	Related work	5
1.2.1	Enhancing LED bandwidth	5
1.2.2	Enhancing spectral efficiency	6
1.2.3	Experimental prototypes	7
1.2.4	IEEE 802.15 task group 7	8
1.3	Summary of accomplishments	8
2	Overview of an optical SISO system	11
2.1	Coordinate systems	11
2.2	Common terminology	12
2.3	The optical signal chain	14
2.4	Optical SISO channel	18
2.5	Modulation techniques	22
2.5.1	On-off keying	22
2.5.2	Pulse amplitude modulation	23
2.5.3	Pulse position modulation	24
2.5.4	Optical orthogonal frequency division multiplexing	25
3	Optical spatial MIMO: System using imaging receiver	29
3.1	Optical imaging MIMO channel	29
3.2	Imaging receiver normalization framework	34

3.3	Optical SM and SMP modulation techniques	36
3.4	SM and SMP system performance with imaging receiver	38
4	Optical spatial MIMO: Sample indexed spatial orthogonal frequency division multiplexing	50
4.1	SIS-OFDM system outline	52
4.2	SIS-OFDM system performance	55
5	Optical color MIMO: Impact of visual perception on CSK	62
5.1	IEEE 802.15.7 - PHY III	63
5.2	CSK system outline	67
5.3	Linear system model	70
5.4	Non-linear system model	75
5.5	CSK system performance under illumination constraints	82
6	Optical color MIMO: Metameric modulation	88
6.1	Metamerism	88
6.2	MM system outline	90
6.3	MM system performance	94
7	Optical wireless broadcast system design	101
7.1	Singular value decomposition based OWC system	101
7.1.1	Native SVD system	102
7.1.2	SVD-VLC system outline	104
7.1.3	SVD-VLC system performance	107
7.2	Multi-wavelength OWC system	114
7.2.1	WDM system outline	114
7.2.2	WDM system performance	117
8	Conclusions	126

References **129**

Resume **134**

List of Tables

4.1	Example SIS-OFDM data streams using ACO-OFDM	54
4.2	Example SIS-OFDM subcarrier and luminaire assignment	54
5.1	Color bands as outlined in IEEE 802.15.7	64
5.2	Color bands combinations as outlined in IEEE 802.15.7	65
5.3	Design rules to compute constellation points for M -ary CSK	66
6.1	MM symbol mapping	93
7.1	SVD-VLC system configuration parameters	108
7.2	SVD-VLC simulation illumination constraints	112
7.3	SVD-VLC simulation illumination results	112

List of Figures

1·1	Cisco VNI forecast	2
1·2	Total cumulative worldwide socket penetration	3
2·1	Global and receiver coordinate systems	12
2·2	OWC downlink block diagram	14
2·3	Optical OOK signals	22
2·4	Optical PAM signals	23
2·5	Optical PPM signals	24
2·6	Optical OFDM block diagram	26
3·1	Optical MIMO system with imaging receiver	30
3·2	Schematic of an imaging receiver	31
3·3	SM and SMP implementation block diagram	37
3·4	SM and SMP performance comparison	40
3·5	Spots on the sensor for different α_s	42
3·6	BER vs SNR for different α_s	43
3·7	Spots on sensor for different η_s	44
3·8	BER vs SNR for different η_s	45
3·9	Spots on sensor for different μ_s	47
3·10	BER vs SNR for different μ_s	48
4·1	SIS-OFDM system block diagram	51
4·2	SNR vs DC Offset for SIS-OFDM	57

4.3	SIS-OFDM and SISO-OFDM performance comparisons	59
4.4	Performance of SIS-OFDM spatial and OFDM streams	60
5.1	Color band centers on CIE-CS	64
5.2	M -ary CSK (normalized) constellation design rules	68
5.3	CSK signal chain block diagram	70
5.4	CSK linear model BER vs SNR performance for all CBCs	73
5.5	Received symbols for CSK linear model with and without clipping .	74
5.6	CIE 1931 XYZ color matching functions	76
5.7	CSK non-linear model BER vs SNR performance for all CBCs . . .	79
5.8	Received symbols for CSK non-linear model without clipping	80
5.9	Received symbols for CSK non-linear model with clipping	81
5.10	CSK BER vs LSNR performance for all CBCs	85
6.1	Typical photopic relative luminous efficiency function	89
6.2	Normalized absorbance of photons by rods and cones	90
6.3	Example gamuts for MM with $D = 4$, $K = 3$ and $M = 2$	91
6.4	MM example timing diagram	94
6.5	MM block diagram using IEEE 802.15.7 CBCs	95
6.6	BER vs SNR for different combinations of CBC	97
6.7	BER vs LSNR for different combinations of CBC	99
7.1	Native SVD system block diagram	103
7.2	SVD-VLC system block diagram	106
7.3	Spectral efficiency upper bound vs dimming	109
7.4	Spectral efficiency upper bound vs link distance	109
7.5	Spots on sensor at different link distances	111
7.6	Generation and maintenance of illumination state by SVD-VLC . .	113

7.7	Transmitting element normalized spectral power distribution	118
7.8	Filter transmittance for FWHM = 40 nm	119
7.9	Receiver quantum efficiency and responsivity	120
7.10	SNR vs CCT for multi–color system	121
7.11	SNR vs transmitter SPD spread for multi–color system	123
7.12	SNR vs filter FWHM for multi–color system	124

List of Abbreviations

ACO	Asymmetrically Clipped Optical
APD	Avalanche Photo Diode
AWGN	Additive White Gaussian Noise
CCT	Correlated Color Temperature
CIE	Commission Internationale de l'Eclairage
CIE-CS	CIE 1931 XYZ Color Space
CMOS	Complementary Metal Oxide Semiconductor
CP	Carrier Prefix
CSI	Channel State Information
CSK	Color Shift Keying
DCO	DC biased Optical
DMT	Discrete Multi-Tone
E/O	Electrical to Optical
FEC	Forward Error Correction
FFT	Fast Fourier Transform
FOV	Field Of View
FWHM	Full Width at Half Maximum
GCS	Global Coordinate System
ICI	Inter Channel Interference
IEEE	Institute of Electrical and Electronics Engineers
IFFT	Inverse Fast Fourier Transform
IID	Independent and Identically Distributed
IM/DD	Intensity Modulation / Direct Detection
IR	Infra-Red
ISI	Inter Symbol Interference
LED	Light Emitting Diode
LOS	Line Of Sight
LSNR	Luminous Signal to Noise Ratio
MAC	Medium Access Control
MIMO	Multiple Input Multiple Output
ML	Maximum Likelihood
MM	Metameric Modulation
MSM	Multiple Subcarrier Modulation
NLOS	Non Line Of Sight

NN	Nearest Neighbor
NRZ	Non-Return to Zero
O/E	Optical to Electrical
OFDM	Orthogonal Frequency Division Multiplexing
O-OFDM	Optical-OFDM
OOK	On-Off Keying
PAM	Pulse Amplitude Modulation
PCS	Primary Color Space
PD	Photo Diode
PHY	Physical layer
PIN	P-I-N Junction
PPM	Pulse Position Modulation
PWM	Pulse Width Modulation
QAM	Quadrature Amplitude Modulation
RCS	Receiver Coordinate System
RF	Radio Frequency
RZ	Return to Zero
RGB	Red, Green and Blue
SD	Standard Deviation
SISO	Single Input Single Output
SIS	Sample Indexed Spatial
SM	Spatial Modulation
SMP	Spatial Multiplexing
SNR	Signal to Noise Ratio
SPD	Spectral Power Distribution
SSK	Spatial Shift Keying
SVD	Singular Value Decomposition
TIA	Trans-Impedance Amplifier
UCS	Universal Color Space
UV	Ultra-Violet
VCS	Visual Color Space
VLC	Visible Light Communication
VNI	Visual Networking Index
VPPM	Variable Pulse Position Modulation
WDM	Wavelength Division Multiplexing

Chapter 1

Introduction

1.1 Motivation

The demand for wireless capacity to access the internet has greatly increased with rise in use of mobile computing devices including, laptops, tablets, and phones. We are increasingly using the internet to access articles, financial services, social networking, shopping, multimedia applications, gaming etc to name a few. There is ongoing research and increasing commercial activity in the field of smart spaces where everything from appliances, gadgets, power grid to home security are networked via cloud based services. These devices have been widely adopted and have become an integral part of our daily lives. The Cisco visual networking index (VNI) forecast (Cisco VNI, 2014) illustrated in Figure 1.1 predicts increase in networked traffic at a cumulative rate of 61% per year – thus network traffic shall double every two years.

With increase in use of mobile devices to access online services, wireless is increasingly the preferred method for internet access. This is currently being accomplished using the electromagnetic radiation within the radio frequency (RF) spectrum. The RF spectrum is a limited resource and the existing spectral allocations limit the ability to increase the system capacity thus making it ever so difficult to keep up with the wireless demand. In contrast to RF, light-based communication, and particularly the visible spectrum, is underutilized, unregulated and has the potential to be exploited to provide extra capacity to meet the demand for wireless communications especially for indoor spaces.

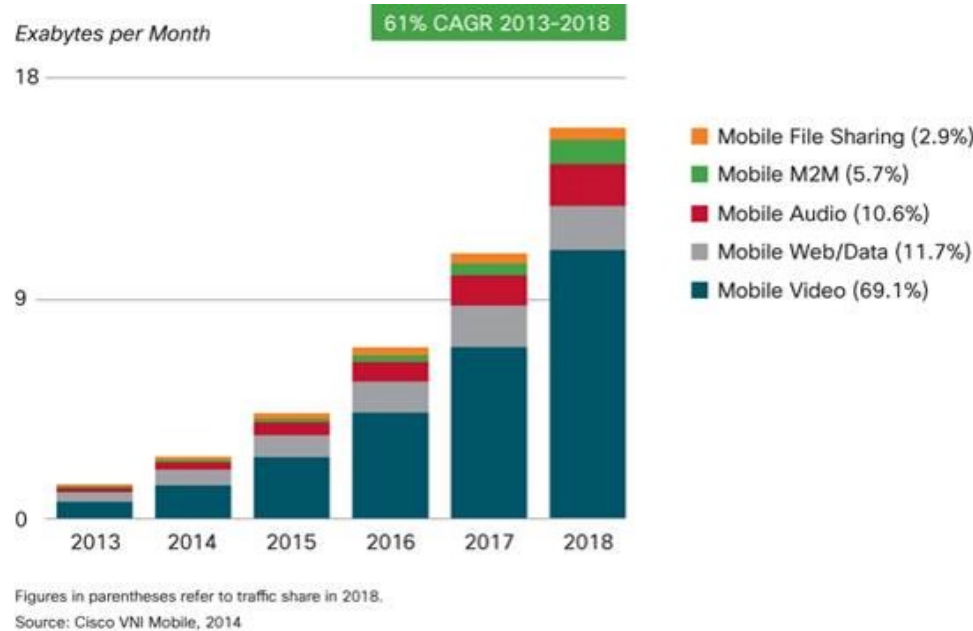


Figure 1·1: Cisco VNI forecast (Cisco VNI, 2014)

Advances in solid state lighting has revolutionized the lighting industry. The realized energy and cost savings are leading the adoption of light-emitting-diode (LED) as the preferred source of illumination. Figure 1·2 (Baribeau, 2011) predicts a worldwide socket penetration of at least 55% by year 2020. Lighting companies are now competing to replace all existing lighting fixtures with the new energy-efficient LED devices. Because lighting is well positioned to support human activities, it is also well positioned to serve as a highly localized wireless access vehicle by modulating the visible spectrum (380 nm – 780 nm). This model is called the ‘dual use’ of lighting and communication. In a practical implementation, overhead luminaires provide light and data downlink as an offload medium, being augmented by the availability of other media including RF as part of a heterogeneous network (Gancarz et al., 2013; Rahaim and Little, 2015).

The output luminous flux from an LED varies proportional to the current through the device. Information transmission can be achieved by modulating the current at

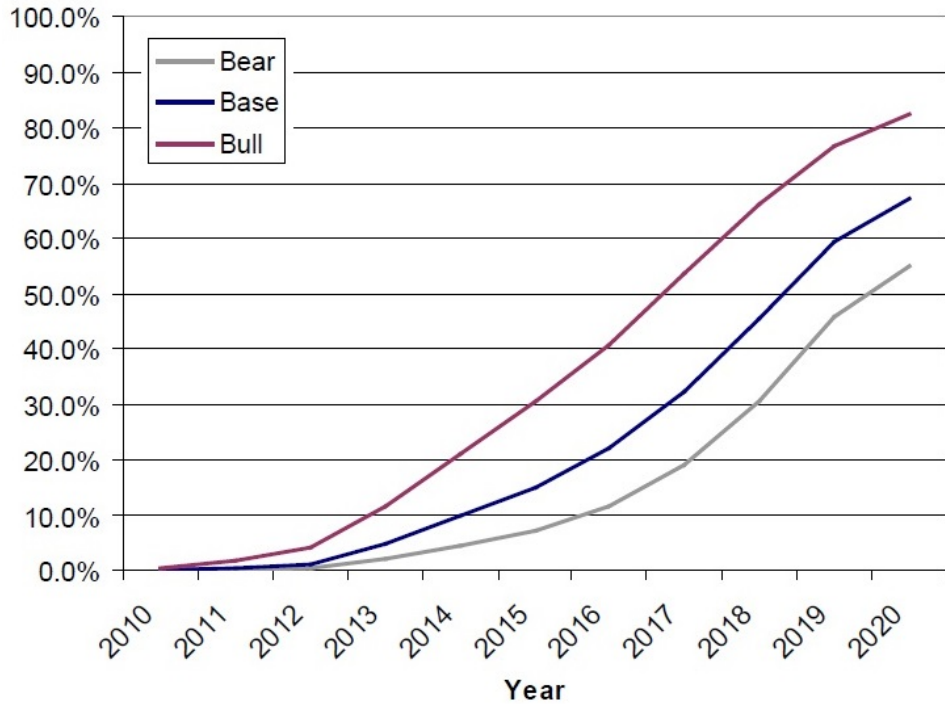


Figure 1·2: Total cumulative worldwide socket penetration (Baribeau, 2011)

a relatively high frequency (> 200 Hz), generating a corresponding luminous flux, whose fluctuations are imperceptible to human eye. An optical receiver can sense this fluctuating illumination pattern and extract the transmitted information. This form of information transfer is known as intensity modulation / direct detection (IM/DD) and is widely used for optical wireless communication (OWC). Under this model, each light in an indoor space can be deployed as a wireless access point while providing illumination. Directionality of light along with high attenuation while propagating through walls provides an extra layer of security for information exchange with light in indoor spaces. Deploying multiple devices within the indoor space can enable spatial reuse over non-overlapping cones of illumination thus providing high bandwidth density.

A simple OWC link can be established by incorporating an LED as a transmitter

and a photodiode (PD) as a receiver. The LED primarily services the function of providing illumination. At the same time, it can transmit information by rapidly changing its intensity. A typical illumination grade ‘white’ LED uses a blue LED as the primary source of photons. The blue LED is encased in a phosphorescent encapsulant that emits yellow photons when excited by the blue photons. The blue and the yellow photons combine to generate white light for illumination. Different shades of white can be generated by changing the concentration of phosphorescent material. Phosphorescence is a slow process and limits the signal bandwidth that can be achieved in such a system to about 1 MHZ – 2 MHz.

Different research groups have investigated optical signal bandwidth extension techniques. Techniques to improve achievable spectral efficiency of a single-input single-output (SISO) OWC system have also been well investigated. Spatial and wavelength based multiple-input multiple-output (MIMO) system proof of concepts have been reported in literature. Some of this research is summarized in the next section. The primary aim of the above enhancements was to demonstrate feasibility of optical spectrum to provide high speed wireless communication. Very little focus was given to given to achieve the primary function of a lighting fixture – illumination.

Incorporation of illumination targets while seamlessly providing wireless access is important for indoor OWC systems to be practically adopted. For OWC to be a viable candidate for mitigating ‘bottleneck’ on wireless downlink, the achievable data rates per user need to be at least of the same order as those using RF. Thus it is important to improve the performance of optical modulation techniques and achievable spectral efficiencies using the optical spectrum. To that end, this dissertation investigates MIMO OWC systems under illumination targets and improves upon the state of the art by better utilizing the spatial and color dimensions.

1.2 Related work

Research to improve the performance of OWC has gained traction in recent years. Wireless data rates are directly proportional to a function of achievable bandwidth and spectral efficiency of modulation techniques. Thus recent research efforts have been focused on improving these system features. Along the way, a few experimental prototypes have also been reported. Efforts to standardize visible light communication (VLC) has created the institute of electrical and electronics engineers (IEEE) 802.15.7 standard.

1.2.1 Enhancing LED bandwidth

At conventional office lighting illumination levels (400 lux), a SISO optical communication channel operates at a high signal-to-noise ratio (SNR) but is limited in its capacity due to the inherent low switching speeds of high brightness LEDs used for illumination (1 MHz – 2 MHz). In a phosphor converted white LED, while the blue LED can be modulated at higher frequencies, the phosphor conversion process is a relatively slow process thus limiting the bandwidth of the device. (Grubor et al., 2008) use a blue filter at the receiver to extract just the blue part of the incident spectrum and thus improve the modulation 3 dB bandwidth of the LED to about 20 MHz; however at the cost of the received signal power. In (Minh et al., 2008), the authors use resonance equalization at the transmitter to achieve an overall 3 dB bandwidth of about 25 MHz. In (Zeng et al., 2008), the authors use an equalizer at the receiver to extend the channel 3 dB bandwidth to about 50 MHz. In (Tsonev et al., 2014), μ LEDs have been shown to provide 3 dB bandwidth of 60 MHz. However, feasibility of μ LEDs for illumination purposes is yet to be tested. The LED device itself has a slow roll-off in its frequency response beyond its 3 dB attenuation point. This makes it possible to transmit information at higher frequencies using lower order

modulation techniques corresponding to lower achievable SNRs while maintaining a target bit error rate (BER).

1.2.2 Enhancing spectral efficiency

Another way to increase the datarate of OWC is to implement spectrally efficient modulation techniques. For this, orthogonal frequency division multiplexing (OFDM) or discrete multi-tone (DMT) modulation have been modified to meet the optical constraints (Vucic et al., 2009a; Mesleh et al., 2010b; Mesleh et al., 2010a; Dissanayake et al., 2011). In (Carruthers and Kahn, 1996), a multiple subcarrier modulation (MSM) technique is implemented by adding DC bias to a real valued time domain OFDM symbol to minimize signal clipping. This technique is also known as DCO-OFDM. While this technique does increase the spectral efficiency, it is power inefficient. In ACO-OFDM (Armstrong and Lowery, 2006), half the spectral efficiency of DCO-OFDM is sacrificed for power efficiency. In this technique, data is assigned to only the odd subcarriers and the time domain OFDM symbol is clipped below zero. Noise introduced due to clipping in this manner has been shown to be orthogonal to the signal. The entire symbol (with additive noise) can be reconstructed at the receiver and transmitted data can be recovered. Higher spectral efficiencies can be achieved by using multiple transmitting elements with multiple receiving elements in a MIMO system. Such a MIMO system can exploit additional dimensions of space and color. Spatial modulation (SM) (Mesleh et al., 2006) exploits the spatial dimension by encoding bits in the index of an active transmitter. Color shift keying (CSK) (IEEE 802.15.7, 2011) exploits the color dimension by encoding bits in the color of the transmitted flux.

1.2.3 Experimental prototypes

In (Vucic et al., 2010), the authors experimentally achieve 513 Mb/s data rates over a SISO link for $\text{BER} \leq 2 \times 10^{-3}$. The transmitter implemented DMT with 127 subcarriers within a bandwidth of 100 MHz (beyond the 3dB bandwidth); each modulated with different M -ary quadrature amplitude modulation (QAM) constellation based on bit and power loading. An equalizer was implemented at the receiver based on the estimated channel. The system was operated at 1000 lx illumination at the receiver. (Tsonev et al., 2014) implement optical OFDM techniques with 512 subcarriers, pre-equalization and bit and power loading along with gallium nitride μ LED front end to demonstrate feasibility of 3 Gb/s SISO link. In (Cossu et al., 2012), the authors experimentally achieve 1.5 Gb/s for a SISO link and 3.4 Gb/s data rates over a wavelength division multiplexed (WDM) MIMO link for $\text{BER} \leq 2 \times 10^{-3}$ using commercial red, green and blue (RGB) LED. In both cases, the transmitter implemented DMT with 512 subcarriers within a bandwidth of 250 MHz; each modulated with different M -QAM constellation based on bit and power loading. An equalizer was implemented at the receiver based on the estimated channel. The system was operated at 410 lx illumination at the receiver. For SM, a non-imaging receiver suffers from outages at symmetry points. At the same time the channel matrix is ill-conditioned (Zeng et al., 2009). While coverage can be improved using angle diversity receivers (Carruthers and Kahn, 2000), the performance can be enhanced remarkably by considering an imaging receiver to decorrelate the coefficients of the MIMO channel matrix (Djahani and Kahn, 2000). The imaging receiver architecture (Kahn et al., 1998) has the potential to provide the highest capacity for a VLC channel along being incorporated in a handheld device. A spatial multiplexing indoor MIMO technique for VLC technology using OFDM and a imaging receiver is considered in (Azhar et al., 2013). Here a 4x9 MIMO system is implemented. Here, the four transmitters implement

DCO-OFDM with 32 subcarriers within a bandwidth of 4 MHz; each modulated with M -QAM symbols. Blue filtering and equalization is implemented at the receiver. The authors experimentally achieve 1 Gb/s transmission with average BER $\leq 10^{-3}$ at an illumination of 1000 lx. Some research has been carried out to achieve low datarate optical communications using cameras in mobile devices. CamCom protocol (Roberts, 2013) is being developed by researchers at Intel to integrate OWC with existing portable devices equipped with cameras.

1.2.4 IEEE 802.15 task group 7

The IEEE 802.15.7 task group has drafted medium access control (MAC) and physical layer (PHY) standards to support free space optical communications (IEEE 802.15.7, 2011). These specifications enable high data rate communications along with dimming. The current LED infrastructure can support the PHY III specifications (Rajagopal et al., 2012). The standard outlines CSK with a linear system model to implement OWC with PHY III. In CSK, bits are encoded in the color that the luminaire produces. To transmit a bit sequence, the luminaire produces different colors which are averaged out by the human eye to produce the ‘white’ set point. The standard supports up to 16-CSK at 24 MHz clock rate which can provide data rates up to 96 Mb/s.

1.3 Summary of accomplishments

This dissertation investigates modulation techniques in conjunction with IM/DD for indoor optical wireless broadcast systems in presence of user requested illumination targets. In chapter 3, a novel framework is proposed to analyze performance of optical imaging MIMO systems. Performance improvements of up to 45 dB for optical systems have been achieved by decorrelating spatially separate links by incorporating an imaging receiver. In chapter 4, we propose sample indexed spatial orthogonal

frequency division multiplexing (SIS-OFDM) - a novel MIMO modulation technique that exploits the spatial, temporal and frequency dimensions in order to achieve high spectral efficiency of a MIMO OWC system while maintaining relatively low system complexity. SIS-OFDM can provide significant additional spectral efficiency of up to $(N_{sc}/2 - 1) \times k$ bits/symbol where N_{sc} is total number of subcarriers and k is number of bits per underlying SM symbol. Human visual perception can be characterized by the *commission internationale de l'eclairage* (CIE) 1931 XYZ color space. It is shown in chapter 5 that the non-linearity introduced by visual perception for a practical CSK system can have a performance penalty of up to 15 dB when compared to the simplified linear CSK system abstraction as proposed in the IEEE 802.15.7 standard. Luminous-signal-to-noise ratio (LSNR), a novel metric to compare performance of different signaling techniques operating at same illumination intensity levels, is also introduced. Metameric modulation (MM) is proposed in chapter 6 and is studied as a MIMO signaling technique that exploits the color dimension with multiple sets of LEDs to improve spectral efficiency. We show that MM always generates the true requested illumination color and has the potential to provide better color rendering by incorporating multiple LEDs. Chapter 7 then proposes a novel technique by using singular value decomposition (SVD) based OWC system architecture to incorporate illumination constraints independent of communication constraints in a MIMO system. It then provides a novel analysis to study performance of a multi-colored wavelength division multiplexed indoor OWC system under different system parameters.

As a part of the smart lighting engineering research center, during this dissertation, prototypes and proof-of-concept demonstrations have been developed in collaboration with partners at Tufts University and Rensselaer Polytechnic Institute. Specifications were generated to develop a 4×4 optical MIMO system with an imaging receiver to

operate it at 400 lx illumination level. A color sensor platform (CuSP) has also been developed to create a network of color sensor platforms in a smart space that support smart controls.

Chapter 2

Overview of an optical SISO system

An optical SISO link can be established between a single transmitting element and a single receiving element. This chapter outlines coordinate systems used for analysis in this work. An overview of common optical terminology and an optical signal chain is then provided. An outline of the SISO channel model is then provided along with a mathematical representation of different components involved in the system. An overview of frequently considered optical SISO channel modulation techniques is then provided.

2.1 Coordinate systems

Establishing a coordinate system convention helps to simplify mathematical representation of distances between different devices and signal propagation path lengths. Figure 2.1 illustrates the reference coordinate systems used for all analysis. $[\hat{\mathbf{X}} \hat{\mathbf{Y}} \hat{\mathbf{Z}}]$ and $[\hat{\mathbf{x}} \hat{\mathbf{y}} \hat{\mathbf{z}}]$ are the basis vectors for the global coordinate system (GCS) and the receiver coordinate system (RCS). A corner of the room in an indoor space is the origin of the GCS while the center of the aperture of the receiver is set as the origin of RCS. The receiver's basis vectors are assumed to always extend parallel to the length, width and surface normal of the sensor.

Let $[x_{tx} \ y_{tx} \ z_{tx}]$ be the location of centroid (C_{tx}) of the illumination surface of the transmitter and $[x_{rx} \ y_{rx} \ z_{rx}]$ be the location of the centroid of the receiver concentrator surface in the GCS. The optical axis is then defined by vector \mathbf{d} as calculated in Eq.

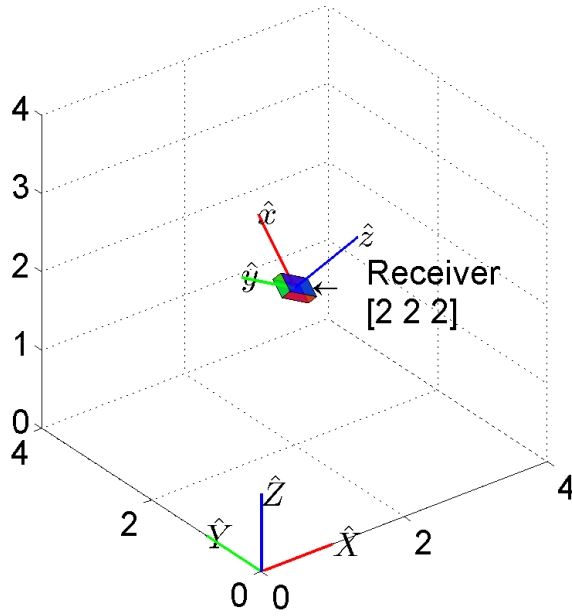


Figure 2·1: Global and receiver coordinate systems

(2.1) and the vertical displacement between the transmitter and receiver is given by \mathbf{d}^z as calculated in Eq. (2.2).

$$\mathbf{d} = \begin{bmatrix} x_{tx} \\ y_{tx} \\ z_{tx} \end{bmatrix} - \begin{bmatrix} x_{rx} \\ y_{rx} \\ z_{rx} \end{bmatrix} \quad (2.1)$$

$$\mathbf{d}^z = (\mathbf{d} \cdot \hat{\mathbf{z}}) \hat{\mathbf{z}} \quad (2.2)$$

2.2 Common terminology

This sub-section outlines optical terminology used in the rest of the text.

Radiant flux

Radiant flux is the amount of radiant energy emitted per unit time by an optical source. Let $P(\lambda)$ be the spectral power distribution (SPD) under consideration. The

radiant flux Φ_W corresponding to the SPD is given by

$$\Phi_W = \int_{\lambda_{\min}}^{\lambda_{\max}} P(\lambda) d\lambda \quad (2.3)$$

(Units: W).

Radiant intensity

Radiant intensity is the amount of radiant flux emitted per unit solid angle by an optical source. (Units: W/sr)

Irradiance

Irradiance is the amount of radiant flux received by a surface/device per unit area. (Units: W/m²)

Luminous flux

Luminous flux is the amount of luminous energy emitted per unit time by an optical source. Let $P(\lambda)$ be the SPD under consideration. The luminous flux Φ_{lm} corresponding to the SPD is given by (Grubor et al., 2008)

$$\Phi_{lm} = 683 \int_{380 \text{ nm}}^{780 \text{ nm}} P(\lambda) V(\lambda) d\lambda \quad (2.4)$$

where $V(\lambda)$ is the eye sensitivity function. (Units: lm).

Luminous intensity

Luminous intensity is the amount of luminous flux emitted per unit solid angle by an optical source. (Units: lm/sr)

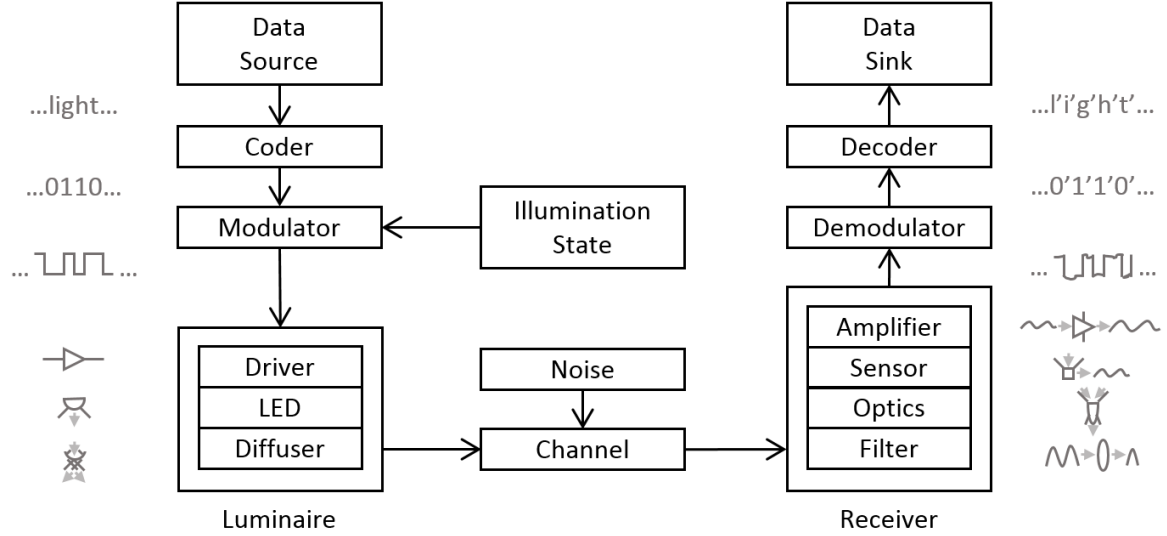


Figure 2.2: OWC downlink block diagram

Illuminance

Illuminance is the amount of luminous flux received by a surface/device per unit area.
(Units: lm/m²)

2.3 The optical signal chain

A practical OWC system operates under the hybrid wireless model paradigm using the VLC channel as the high capacity downlink and another medium for the uplink. This seems to be the accepted model and a reasonable assumption (Rahaim and Little, 2015). Figure 2.2 illustrates a block diagram for a typical downlink using the optical spectrum.

Data source

The source is an entity that, while performing its tasks, produces or replicates information that needs to be communicated to another entity.

Coder

The coder assigns a binary bit sequence to the information from the source. In this process, it may introduce redundancy to reduce the effect of noise and interference in the channel.

Illumination state

The illumination state sets the average output flux and the SPD to be produced by luminaire(s). This is a result of a number of factors such as (a) requested illumination level by users in the space (b) optimal energy usage (c) output of ‘smart’ applications such as circadian control, etc...

Modulator

The modulator, with the knowledge of requested flux, maps and converts the bit sequence into a corresponding waveform that drives the luminaire. The frequency of visible light is in the range of about 380 THz – 780 THz. The current state-of-art electronics cannot sample and process signals at that high speeds. Thus traditional modulation schemes which vary the amplitude, frequency or phase of the waveforms within the RF spectrum cannot be directly implemented within the visible spectrum. Instead, the average power (a.k.a flux/intensity) of the visible waveforms are modulated to transmit data. Optical sensors like PD produce output current proportional to the intensity of the incident radiation and not the waveform of the radiation itself. This signaling scheme is known as IM/DD. All optical modulation techniques are implemented in conjunction with IM/DD. This method introduces unique constraints that differentiate optical modulation techniques from RF modulation techniques.

Luminaire/Transmitter

The luminaire is composed of a driver, LEDs and diffuser optics. A simple LED driver is a trans-conductance amplifier whose input is the waveform produced by the modulator. The corresponding output current drives the LED which in turn generates light. A luminaire is made up of number of phosphor converted white LEDs or different narrow-band devices which produce different colors. A phosphor converted white LED is made by coating a blue LED with yellow phosphor. The blue light excites the yellow phosphor and together they produce white light. The diffuser scatters the light produced by the LED(s) to mix the different colors and output a relatively homogenous, glare-free light which makes the luminous surface appear softer and more pleasing to the eye. Different diffuser front ends generate different sizes of cones of emission. The most common emission pattern is the Lambertian pattern.

Channel

The channel is the medium through which information flows. It is made up of all the paths traveled by the light rays between the luminaire and the receiver. Depending on the number of transmitters, colors or number of receiving elements, the channel can be configured into various single/multiple input single/multiple output configurations. For the OWC downlink, the indoor space acts as the channel. In addition to the line-of-sight (LOS) path from the luminaire to the receiver, various reflected rays of light propagating over different path lengths may be incident on the receiver. In an RF system, such multi-paths cause inter-symbol-interference (ISI) that needs to be resolved for. In the indoor OWC system, due to poor reflectivity off various walls and directionality of receiving optics, optical signals propagating over such multi-paths have been shown to be heavily attenuated when incident on the active element of the

receiver. In addition, difference in path lengths between LOS and non-LOS (NLOS) propagation within indoor spaces is very small. This produces a small delay spread which is insignificant when compared to frequency of intensity modulation.

Receiver

A receiver is made up of an optical filter, refractive optics, an optical sensor like PD and an amplifier. Some high speed systems transmit data over a small range of wavelengths (ex blue (400 nm – 500 nm)) while the entire visible spectrum is used for illumination. In such cases, a blue filter is used to remove noise from parts of the optical spectrum that do not carry any information. For wavelength division multiplexed (WDM) systems where data is transmitted independently over different parts of the spectrum, multiple non-overlapping filters are used to decorrelate the different streams of information. For single pixel receivers, concentrator optics are used to increase the effective area of the sensor while keeping its capacitance at a minimum. A number of single pixel receivers can be configured in a matrix pattern to realize a non-imaging multiple element receiver. For imaging receivers, imaging optics are used to help decorrelate the multiple channels. Sensor devices such as p-i-n junction photodiode (PIN-PD), avalanche photodiode (APD) or complementary metal oxide semiconductor (CMOS) active pixel devices generate an electrical signal proportional to radiant flux incident on the sensor. This electrical signal is amplified and conditioned before it is processed to recover transmitted information. Randomness in photon arrival and sensing gives rise to shot noise within the system. Amplifiers such as trans-impedance amplifiers (TIA) introduce thermal noise into the system. This noise then distorts the signal waveform and can cause errors in information recovery.

Demodulator

With prior knowledge of the modulation scheme implemented, the demodulator makes an intelligent estimate of the transmitted signal waveform. After recovering the transmitted waveform, it de-maps it to recover the transmitted bit sequence. Significant noise that is not orthogonal to the signal waveform can introduce errors in the de-modulated sequence.

Decoder

The decoder, with prior knowledge of the coding scheme implemented, tries to recover the transmitted information from the bit stream. Redundancy introduced in the coded data can help the decoder to detect and rectify errors.

Data sink

Ideally, the data sink is the entity to which the information was transmitted to.

2.4 Optical SISO channel

A SISO VLC link can be established between a single luminaire broadcasting information over optical spectrum and a single receiver that can generate an electrical signal proportional to incident optical radiation. Let the radiant flux emitted by the transmitter be represented by x . Intensity modulation imposes a non-negativity constraint ($x \geq 0$) on the transmitted signal. The emitted radiant flux also provides illumination. Let P_{avg} be the average transmitted radiant flux to maintain user requested illumination levels. Thus mean of transmitted signal must equal P_{avg} .

The transmitted flux propagates through the indoor space and traverses over different paths arriving at the receiver. The received flux can be expressed as a convolution of the channel impulse response and transmitted flux waveform. Under the

‘luminaire as a transmitter’ model, the LOS component of the received flux is dominant over the NLOS component. In addition to free space path losses, the NLOS component of the received flux undergoes additional attenuation due to non-ideal reflectivity of the walls. The delay spread for the indoor channel is small when compared to frequency of intensity modulation. Under these circumstances, the channel can be treated as a LOS channel and the channel impulse response can be represented by a single tap with gain h .

At the receiver, additive noise independent of the signal is added to the received signal and represented by w . Let the total received signal and noise be represented by y . The SISO channel can then be modeled as in Eq. (2.5).

$$y = hx + w \quad (2.5)$$

The channel gain is a function of the radiant intensity of emitted flux, the free space square path loss, optical gains at receiver and receiver sensor responsivity. Let the radiant intensity emitted by the transmitter at any angle ϕ subtended between the transmitter surface normal and the optical axis be given by $L(\phi)$. Radiant intensity of a Lambertian transmitter of order m is given by

$$L(\phi) = \begin{cases} \frac{(m+1)}{2\pi} \cos^m(\phi) & ; -\pi/2 \leq \phi \leq \pi/2 \\ 0 & ; \text{else} \end{cases} \quad (2.6)$$

The SISO receiver optics comprises of an optical concentrator. Incorporating a concentrator helps increase the effective area of the sensor. This enables the receiver to incorporate a sensor with smaller dimensions thus reducing its capacitance and enabling a higher receiver bandwidth. Additionally sensor with smaller dimensions enables a compact form factor which can then enable its integration within portable devices. Let ψ be the angle between the receiver surface normal ($\hat{\mathbf{z}}$) and the optical axis (\mathbf{d}). Let η be the refractive index of the material of the concentrator and ψ_c be

the field of view of the concentrator. Then the optical concentrator gain is given by

$$G(\psi) = \begin{cases} \frac{\eta^2}{\sin^2(\psi_c)} & ; 0 \leq \psi \leq \psi_c \leq \frac{\pi}{2} \\ 0 & ; \psi > \psi_c \end{cases} \quad (2.7)$$

Let $S(\lambda)$ be the normalized SPD of the normalized emitted radiant flux such that area under curve is 1 W. Let $R(\lambda)$ be the responsivity of the PD. An optical filter can be incorporated within the receiver to provide selectivity to wavelengths of interest and reject unwanted optical radiation thus reducing noise. Depending on construction of optical filter, its transmittance is a function of angle of incidence and wavelength of radiation. Let the transmittance of the filter be given by $T(\psi, \lambda)$. Thus the effective responsivity of the receiver including the transmission and gains from all optical components is given by

$$R_e(\psi) = G(\psi) \int_{\lambda_{\min}}^{\lambda_{\max}} S(\lambda) T(\psi, \lambda) R(\lambda) d\lambda \quad (2.8)$$

where λ_{\min} to λ_{\max} span all the wavelengths of interest.

Let A be the active area of the PD. The overall channel gain h is a function of the parameters discussed above and is then given by

$$h = L(\phi) \frac{A}{||\mathbf{d}||^2} \cos(\psi) R_e(\psi) \quad (2.9)$$

Average flux incident on a PD introduces shot noise within the optical-to-electrical conversion process. In a typical SISO VLC link, shot noise from ambient illumination dominates over that from signal (Barry, 1994). Let q be the charge of an electron. Worst cast shot noise current density from isotropic ambient radiant flux $P_a(\lambda)$ is

then given by

$$\sigma_{\text{sh}}^2 = 2q < I > \quad (2.10)$$

$$\sigma_{\text{sh}}^2 = \frac{2qAG(\psi_c)}{\psi_c} \int_{\lambda_{\min}}^{\lambda_{\max}} \int_0^{\psi_c} P_a(\lambda) R(\lambda) T(\psi, \lambda) d\psi d\lambda \quad (2.11)$$

$< I >$ is the average current. Statistics of shot noise are typically Poisson in nature. For a large mean, a Poisson random variable can be approximated by a normal distribution with same variance. Thus, for the optical channel, shot noise is assumed to be distributed normally with variance σ_{sh}^2 .

The TIA is generally the first current to voltage amplifier stage after the PD. In the absence of significant ambient illumination, the TIA noise is the dominant source of noise (Kahn and Barry, 1997). The thermal noise from the TIA is considered as the dominant electronic noise component. It is typically additive, white and Gaussian and its noise current density is given by (Kahn and Barry, 1997),

$$\sigma_{\text{th}}^2 = \frac{4kT}{R_f} \quad (2.12)$$

where k is the Boltzmann's constant, T is the absolute temperature and R_f is the feedback resistance of the TIA.

Thus the total noise current density can be computed from the shot noise current density and thermal noise current density. It is modeled as additive, white and Gaussian and its variance is given by

$$\sigma_n^2 = \sigma_{\text{sh}}^2 + \sigma_{\text{th}}^2 \quad (2.13)$$

While P_{avg} is the average transmitted radiant flux and let B be the signal bandwidth. Using the parameters described above the SISO channel's SNR can be defined

by Eq. (2.14).

$$\text{SNR} \triangleq \frac{(hP_{\text{avg}})^2}{\sigma_n^2 B} \quad (2.14)$$

2.5 Modulation techniques

The optical carriers span the electromagnetic spectrum within 380 THz – 780 THz range. Lack of adequate electronics for passband transmission or reception at such high frequency range makes it impractical to implement coherent signaling schemes. However, it is possible to vary the intensity of such spectrum at the transmitter and detect it directly by radiant flux to electrical signal conversion at the receiver. Thus, modulation techniques are implemented in conjunction with IM/DD to transfer information using the optical spectrum. A number of different modulation techniques have been studied for RF wireless communications. Some of those have been adapted for OWC due to the unique constraints of the optical channel. This section provides a summary of the more popular SISO modulation techniques.

2.5.1 On-off keying

As the name suggests, OOK transmits information in the form of high intensity (on) or low intensity (off) of radiant flux. It is typically implemented under the non-return

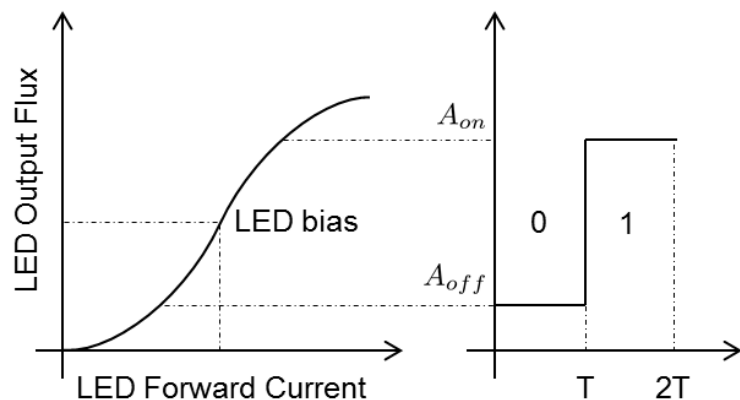


Figure 2.3: Optical OOK signals

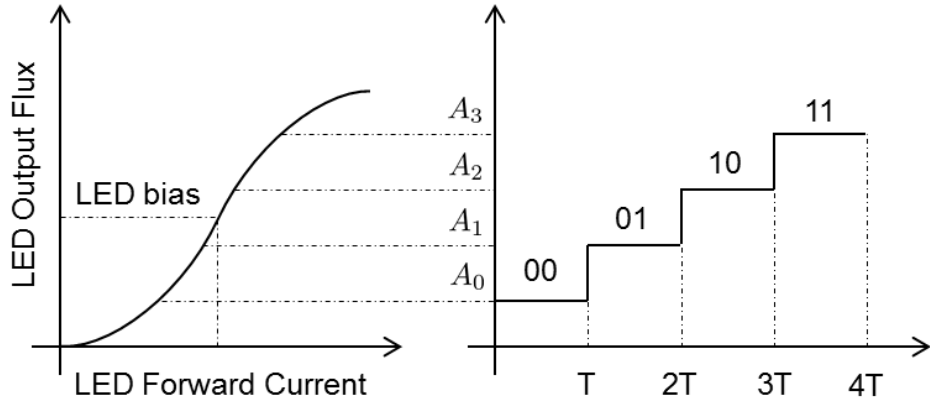


Figure 2.4: Optical 4-PAM signals

to zero (NRZ) model. To transmit bit ‘0’, the transmitter drives all LEDs at a low intensity level and to transmit bit ‘1’, it drives them all to a high intensity level. The on and off intensity levels can be set to achieve a desired average illumination level. Figure 2.3 illustrates the OOK signal waveforms. A_{off} is the low intensity radiant flux and A_{on} is the high intensity radiant flux emitted by the LEDs at the off and on levels. If p is the probability of transmitting bit ‘1’, the average transmitted flux given by $A_{\text{avg}} = (1 - p)A_{\text{off}} + pA_{\text{on}}$ is used to provide illumination whereas flux $A_{\text{com}} = p(A_{\text{on}} - A_{\text{off}})$ is used for communication. OOK-NRZ has a spectral efficiency of 2 bits/Hz. References (Komine and Nakagawa, 2004; Vucic et al., 2009b) have demonstrated feasibility of OWC in indoor spaces while providing illumination using OOK.

2.5.2 Pulse amplitude modulation

M -ary PAM can transfer information by varying the amplitude of each transmitted pulse. $\log_2(M)$ bits to transmit are mapped to one out of M possible pulse amplitudes. The transmitter then drives all LEDs to emit radiant flux corresponding to the mapped amplitude. Let A_{lo} be the lowest pulse amplitude and A_{hi} be the highest pulse amplitude, then the M different amplitude levels are given by

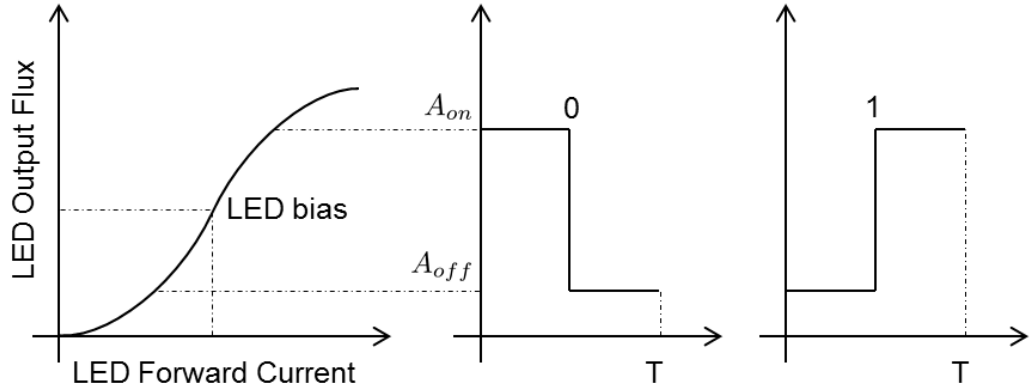


Figure 2.5: Optical 2-PPM signals with 50% duty cycle.

$A_i = A_{lo} + i \times (A_{hi} - A_{lo})(M - 1); 0 \leq i < M$. For equi-probable bits, flux given by $A_{avg} = (A_{lo} + A_{hi})/2$ is used to provide illumination whereas flux $A_{com} = (A_{hi} - A_{lo})/2$ is used for communication. Figure 2.4 illustrates the 4-PAM signal waveforms. References (Grubor et al., 2008) have demonstrated M -ary PAM for OWC in indoor spaces while providing illumination.

2.5.3 Pulse position modulation

M -ary PPM can transfer information by varying the temporal offset (position) for the low-to-high edge of each transmitted pulse. The amplitude and duty cycle of each pulse is kept constant. $\log_2(M)$ bits to transmit are mapped to one out of M possible pulse offsets. To transmit m bits, the transmitter drives all LEDs to emit a constant flux for a constant pulse on-time starting at a corresponding mapped temporal offset. Let A_{off} be the low intensity radiant flux emitted during the off time of each pulse period and A_{on} be the high intensity radiant flux emitted by the LEDs during the on time of each pulse period and let d be the pulse duty cycle. Then irrespective of the distribution on the information bits, flux given by $A_{avg} = (1 - d)A_{off} + dA_{on}$ is used to provide illumination whereas flux $A_{com} = d(A_{on} - A_{off})$ is used for communication. Figure 2.5 illustrates 2-PPM signal waveforms. References (Bai et al., 2010) have

demonstrated using PPM for illumination and communication. VPPM, a variation on PPM, has been proposed in IEEE 802.15.7 as a means to achieve dimming along with data communications. In M -ary VPPM, the information to transmit is still mapped to one out of M possible pulse off-to-on edge start offsets. However, the duty cycle of each pulse can be varied to control the average amount of flux emitted and thus illumination levels. Reference (Rajagopal et al., 2012) outlines using VPPM for illumination and communication.

2.5.4 Optical orthogonal frequency division multiplexing

OFDM is a spectrally efficient modulation technique and has been widely adopted for RF wireless communications. In OFDM, parallel streams of information are mapped over orthogonal frequency bins. Each bin is called a sub-carrier. Usually an M -ary QAM modulation is used to map information over each sub-carrier. An inverse fast Fourier transform (IFFT) operation multiplexes the parallel streams to generate a time domain OFDM symbol to transmit. To mitigate interference due to multi-path, usually a carrier prefix (CP) is appended to the symbol before transmitting it. At the receiver, after removing the CP, a fast Fourier transform (FFT) operation demultiplexes the OFDM symbol to recover the parallel sub-carriers. Each sub-carrier is then demodulated and decoded to recover the information. OFDM has been successfully adapted and widely used for spectrally efficient OWC as summarized in reference (Armstrong, 2009). For OWC, the time domain OFDM symbol is constrained to be real valued and unipolar. Ensuring Hermetian symmetry during symbol mapping over the orthogonal frequency bins generates a real valued time domain signal. Figure 2.6 illustrates signaling chain for optical OFDM (O-OFDM).

Let N_{sc} be the total number of sub-carriers for the O-OFDM frame. In DCO-OFDM, the information bits are mapped to $N_{dco}^d = (N_{sc}/2) - 1$ number of data sub-carriers. An M -QAM modulator then assigns an M -QAM symbol corresponding

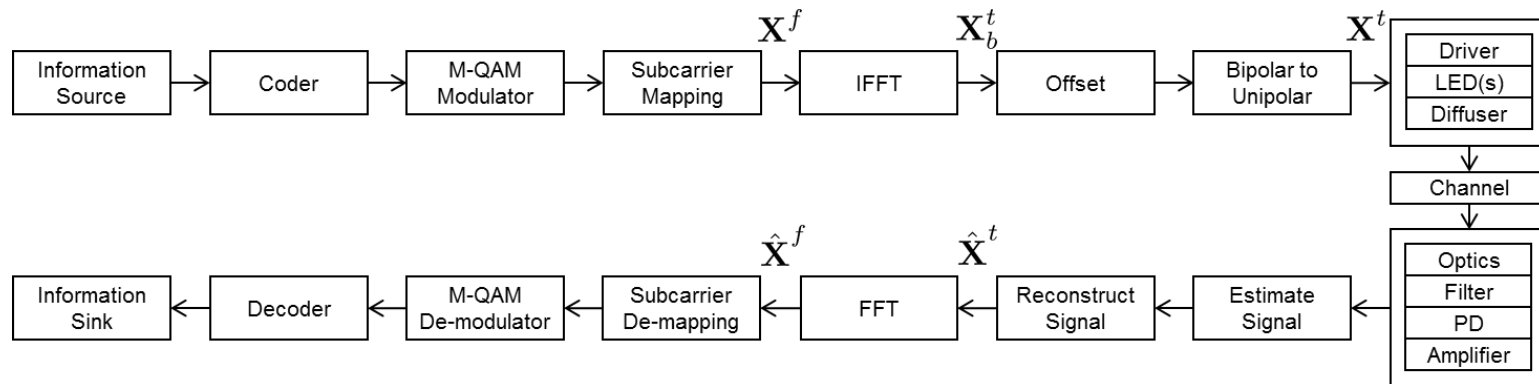


Figure 2·6: Optical OFDM block diagram

the mapped bits on the data sub-carriers. The remaining sub-carriers are assigned Hermetian symmetric M -QAM symbols to form the frequency domain DCO-OFDM frame as shown in Eq.(2.15).

$$\mathbf{X}^f = [0; x_1; \dots; x_{N_{dco}^d}; 0; x_{N_{dco}^d}^*; \dots; x_1^*] \quad (2.15)$$

Taking an IFFT over frame \mathbf{X}^f generates a bipolar time domain symbol \mathbf{X}_b^t . In DCO-OFDM the bipolar to unipolar conversion involves adding an offset to \mathbf{X}_b^t such that majority of the the time domain symbol is non-negative and the symbol can then be clipped at zero. For relatively large N_{sc} , the signal values in the time domain are distributed normally. Thus adding an offset of at least $3.2 \times$ standard deviation (SD) ensures that less than 0.1% of signal values get clipped at zero - thus significantly reducing signal distortion due to clipping at the transmitter.

In ACO-OFDM, only the odd indexed sub-carriers carry data symbols. Hermetian symmetry is then enforced to obtain real valued time domain symbol. The information bits are mapped to $N_{aco}^d = (N_{sc}/4)$ number of data sub-carriers. An M -QAM modulator then assigns an M -QAM symbol corresponding the mapped bits on the data sub-carriers. The frequency domain ACO-OFDM frame construction is shown in Eq.(2.16).

$$\mathbf{X}^f = [0; x_1; 0; x_2; \dots; x_{N_{aco}^d}; 0; x_{N_{aco}^d}^*; \dots; 0; x_2^*; 0; x_1^*] \quad (2.16)$$

Taking an IFFT over frame \mathbf{X}^f generates a bipolar time domain symbol \mathbf{X}_b^t . In ACO-OFDM bipolar to unipolar conversion is achieved by simply clipping the time domain symbol at zero. It has been shown in reference (Armstrong and Lowery, 2006) that this clipping introduces noise only on the non-data bearing even indexed sub-carriers. Thus by simple signal processing, an estimate of transmitted signal can be reconstructed. The N_{aco}^d data sub-carriers are then demodulated and decoded to recover transmitted information. Implementation and performance comparisons of ACO-OFDM and DCO-OFDM is shown in reference (Mesleh et al., 2011).

The performance of an optical SISO channel is constrained by the low modulation bandwidth of LEDs. At the same time, a typical SISO optical channel operates at high SNR levels. Performance gains can be obtained by improving the modulation bandwidth of LEDs and/or by distributing the signal power across multiple dimensions of space, color, polarization etc. to create an optical MIMO channel as explained in next few chapters.

Chapter 3

Optical MIMO system using imaging receiver

Spatial modulation (SM) and spatial multiplexing (SMP) are two MIMO techniques for transmitting data over an indoor optical wireless channel. Receivers for SM and SMP can be of the non-imaging type, in which case the channel matrix coefficients can be highly correlated, or of the imaging type, which can reduce the degree of correlation and improve overall system performance. In this chapter, we propose a novel framework to analyze the performance of imaging MIMO systems. This framework is applied to characterize the performance of SM and SMP under both imaging and non-imaging receivers. Results of our analysis indicate that imaging receivers can provide significant SNR improvements of up to 45 dB under SM and SMP as compared to the use of non-imaging receivers. Finally, the application of the proposed analysis framework indicates specific design principles to optimize imaging receiver parameters¹.

3.1 Optical imaging MIMO channel

In this section, an optical MIMO imaging system as illustrated in Figure 3.1 is considered. Multiple luminaires are located near the ceiling of an indoor space to provide illumination and act as transmitters for communication. Information to transmit is jointly coded across a set of luminaires within the field of view (FOV) of the re-

¹This work is published in peer-reviewed IEEE conference proceeding (Butala et al., 2014b).

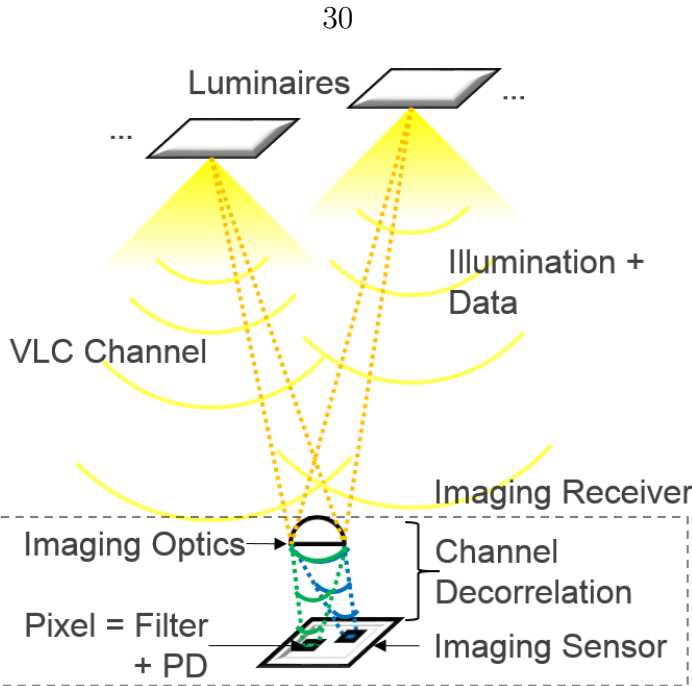


Figure 3·1: Optical MIMO system with imaging receiver

ceiver. User requested illumination state sets the average radiant flux emitted by the transmitters. Based on these inputs, the modulator generates drive signals for each luminaire. LEDs in the luminaire convert modulated data in the electrical domain into optical signals in the visible spectrum (E/O and conversely O/E conversion). These optical signals propagate through the indoor space and are incident on the receiver.

Figure 3·2 illustrates a schematic of an imaging receiver. An imaging receiver for OWC can be modeled as a sensor and imaging optics. The sensor is located at a focal distance f away from the optical center of the lens and is comprised of a grid of detector elements - each referred to as a ‘pixel’. Each pixel is comprised of a filter and optical detector. The imaging optics redirect light rays originating from different locations of an irradiating planar surface such that they are incident on corresponding different locations on the sensor. In other words, based on the angle and the location of incidence on the imaging optics, light rays are redirected on to a specific path due to refraction. Thus imaging optics can extract and isolate optical signals originating

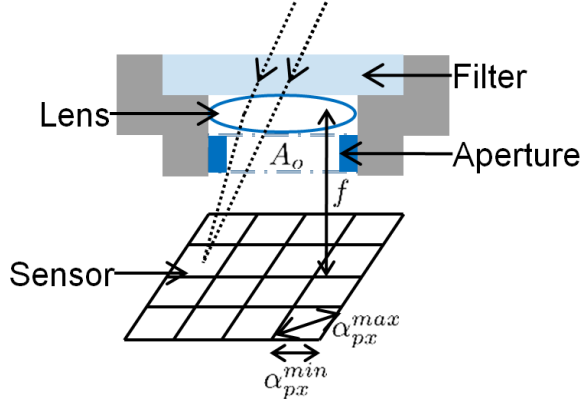


Figure 3.2: Schematic of an imaging receiver

from different spatial locations that get mixed while propagating through the indoor space. This helps to decorrelate signals received from spatially distinct transmitters and help significantly improve communication performance. Similarly, the ambient radiant flux incident at the aperture of the receiver is distributed among all pixels of the sensor. This helps to significantly reduce shot noise per pixel (Djahani and Kahn, 2000). The receiver uses all received streams to jointly decode and recover information.

Let N_{tx} represent number of luminaires using which information is broadcast and let N_{px} represent number of contiguous pixels comprising the sensor of an imaging receiver. The optical $N_{tx} \times N_{px}$ MIMO channel can be represented by

$$\mathbf{Y} = \mathbf{H}\mathbf{X} + \mathbf{W} \quad (3.1)$$

\mathbf{X} is an N_{tx} dimensional vector whose each element is the signal radiant flux emitted by each transmitter. The flux propagates over multiple paths before being incident on the imaging optics. As discussed in the SISO system, the LOS component of received flux is dominant over the NLOS component due to additional propagation and non-ideal reflection losses. \mathbf{H} is an $N_{px} \times N_{tx}$ dimensional channel gain matrix where each element or channel gain coefficient h_{ij} indicates the net channel gain from transmitter

j to pixel i . \mathbf{W} is an N_{px} dimensional noise vector. For imaging receivers, the shot noise at each pixel due to ambient illumination is severely diminished (Djahani and Kahn, 2000) and thus TIA input noise current is dominant source of noise (Kahn and Barry, 1997). For imaging receivers, $\mathbf{W} \sim \mathcal{N}(\mathbf{0}, \sigma_n^2 \mathbf{I})$ where σ_n^2 equals total noise current density. \mathbf{Y} is an N_{px} dimensional vector whose each element is the output signal current from each pixel.

For each individual link between transmitter j and pixel i , the free space gain is defined as the fraction of the radiant flux emitted by the transmitter that is incident on the receiver aperture. Let $[x_j \ y_j \ z_j]$ be the location of centroid C_j of the illumination surface of the j^{th} transmitter and $[x_{\text{rx}} \ y_{\text{rx}} \ z_{\text{rx}}]$ be the location of the centroid of the receiver aperture. Optical axis (\mathbf{d}_j) between transmitter j and receiver can be computed from Eq. (2.1). The free space channel gain is then given by

$$h_j^{\text{fs}} = L_j(\phi_j) \frac{A_o}{\|\mathbf{d}_j\|^2} \cos(\psi_j) \quad (3.2)$$

ϕ_j is the angle subtended between the optical axis and surface normal of the transmitter. $L_j(\cdot)$ is the Lambertian radiant intensity as given by Eq. (2.6). Let A_o be the area of the aperture opening. ψ_j is the angle between the optical axis and surface normal of the receiver.

The magnification property of imaging optics determines the point of incidence on the sensor for a ray of light originating from the irradiating surface of the transmitter. Using ray tracing methods for a point aperture, it can be mathematically represented by

$$M_{\text{im}} = \begin{cases} \frac{f}{\|\mathbf{d}_j\| - f} & ; \psi_j \leq \psi_c^{\text{rx}} \\ 0 & ; \psi_j > \psi_c^{\text{rx}} \end{cases} \quad (3.3)$$

f is the focal length of the imaging optics. ψ_c^{rx} is the FOV of the receiver. Depending on the sensor dimensions, this may be smaller than or equal to the FOV of imaging optics. Assuming the receiver is focused on the transmitter, the location of C_j as

projected in the RCS is given by

$$\begin{bmatrix} x_{\text{sp}} \\ y_{\text{sp}} \\ z_{\text{sp}} \end{bmatrix}_j = \begin{bmatrix} -M_{\text{im}}(\mathbf{d}_j, \hat{\mathbf{x}}) \\ -M_{\text{im}}(\mathbf{d}_j, \hat{\mathbf{y}}) \\ -f \end{bmatrix} \quad (3.4)$$

Assuming the mathematical model of the shape of the luminaire's illumination surface is known, the shape of its projected spot on the plane of surface of the sensor can be calculated. Depending on the geometry of the transmitters and receiver, a pixel may receive light from multiple spots. Accordingly, the system performance gets severely degraded due to the correlated channel matrix coefficients and inter channel interference (ICI). Non-polygonal shapes can be approximated to a polygon with very small error. Polygon intersection algorithms can be used to compute the shared area between a spot and pixel. The imaging channel gain (3.5) between transmitter j and pixel i is then given by the ratio of the fraction of the area of the spot j that is incident on pixel i to total area of the spot j .

$$h_{ij}^{\text{im}} = \frac{\text{Area}(\text{spot}_j \cap \text{pixel}_i)}{\text{Area}(\text{spot}_j)} \quad (3.5)$$

Let $S_j(\lambda)$ be the SPD of the flux over link j and $T_i(\lambda)$ and $R_i(\lambda)$ be the filter transmittance and responsivity at pixel i respectively. The optical filter transmittance in this case is assumed independent of the angle of incidence of the flux. Let Q be the transmittance of the imaging optics. The effective responsivity of pixel i over link j is given by

$$R_{ij} = Q \int_{\lambda_{\min}}^{\lambda_{\max}} S_j(\lambda) T_i(\lambda) R_i(\lambda) d\lambda \quad (3.6)$$

Thus the net channel gain matrix \mathbf{H} can be computed from the free space channel gain, the imaging channel gain and effective pixel responsivity by

$$\mathbf{H}(i, j) = h_{ij} = h_j^{\text{fs}} h_{ij}^{\text{im}} R_{ij} \quad (3.7)$$

where element h_{ij} is the net channel gain from transmitter j to pixel i .

3.2 Imaging receiver normalization framework

It is desired to analyze the effect of imaging receiver configuration on performance of optical MIMO modulation techniques. The system performance is dependent on how the transmitter images or ‘spots’ land on the sensor. Different system configurations can generate similar spot profiles on the sensor and thus similar communication performance. To analyze the OWC system performance independent of a specific system configuration, the following normalization parameters are defined.

Normalized luminaire side length

The normalized luminaire side length α_s is defined as the ratio of the length of the longest segment across a spot to side length of a pixel.

$$\alpha_s \triangleq \frac{M_{\text{im}} a_{\text{tx}}^{\max}}{a_{\text{px}}^{\min}} \quad (3.8)$$

where a_{tx}^{\max} is the length of longest segment across irradiating surface of the luminaire. α_s specifies the spot size relative to the sensor dimensions. For example, consider two similar systems which differ in only the luminaire diagonal and PD side lengths. If both parameters differ in scale by the same factor, α_s would remain the same for both systems. $\alpha_s \leq 1$ implies the spot size is at most as large as the size of a PD. If the centroid of the spot is aligned with the centroid of a PD, the spot will lie completely inside the PD.

Normalized luminaire pitch

The normalized luminaire pitch δ_s is defined as the ratio of the spot-spot pitch to the length of the longest segment across the pixel.

$$\delta_s \triangleq \frac{M_{\text{im}} P_{\text{tx}}}{\alpha_{\text{px}}^{\max}} \quad (3.9)$$

where P_{tx} is the luminaire-luminaire pitch. δ_s specifies the distance between the centroids of adjacent spots relative to the sensor dimensions. For example, consider two similar systems which differ in only the transmitter pitch and PD diagonal. If both parameters differ in scale by the same factor, δ_s would remain the same. $\delta_s > 1$ ensures that centroids of adjacent spots lie on different pixels. In the limit, if both transmitters were point sources, condition $\delta_s > 1$ would ensure that different pixels receive signals from neighboring transmitters, thus eliminating ICI.

Normalized luminaire edge-edge distance

The normalized luminaire edge-edge distance η_s is defined as the ratio of minimum distance between the edges of adjacent spots to the length of the pixel diagonal.

$$\eta_s \triangleq \frac{M_{\text{im}}(P_{\text{tx}} - \alpha_{\text{tx}}^{\max})}{\alpha_{\text{px}}^{\max}} \quad (3.10)$$

η_s specifies the minimum possible distance between the edges of adjacent spots relative to the sensor dimensions. For example, now consider two similar systems which differ in only the minimum possible distance between the edges of adjacent luminaires and PD diagonal. If both parameters scaled by the same factor, η_s would remain the same. $\eta_s > 1$ ensures that adjacent spots do not overlap on any pixel. η_s can be expressed in terms of α_s and δ_s as in (3.12). For square pixels, $l = 1/\sqrt{2}$.

$$l = \frac{\alpha_{\text{px}}^{\min}}{\alpha_{\text{px}}^{\max}} \quad (3.11)$$

$$\eta_s = \delta_s - l\alpha_s \quad (3.12)$$

Normalized magnification

Let M_0 be the magnification of the system when $\alpha_s = 1$. Normalized magnification is defined as the ratio of the magnification of the system to M_0 .

$$M_0 \triangleq \frac{\alpha_{\text{rx}}^{\min}}{\alpha_{\text{tx}}^{\max}} \quad (3.13)$$

$$\mu_s \triangleq \frac{M_{\text{im}}}{M_0} \quad (3.14)$$

Consider two similar systems that differ in distance between the luminaire plane and the receiver and also in the receiver focal lengths. μ_s for both systems is the same value when both parameters differ in scale by the same factor.

3.3 Optical SM and SMP modulation techniques

Optical SM was introduced in (Mesleh et al., 2006) as a low complexity modulation technique that enhances spectral efficiency by exploiting spatial dimension. SM encodes $k = \log_2(N_{\text{tx}})$ bits in the transmitter index in addition to $m = \log_2(M)$ bits using M -ary modulation. Thus SM transmits $r = k + m = \log_2(MN_{\text{tx}})$ bits per SM symbol. The encoded information stream is divided into r bits long contiguous segments. First m bits of each symbol are mapped to one of the M -ary constellation points while the last k bits of each symbol select the luminaire that transmits the selected constellation point. SM implementation is illustrated in Figure 3.3a for $N_{\text{tx}} = 4$ transmitters and 4-PAM. M -PAM intensity levels for SM are selected as in

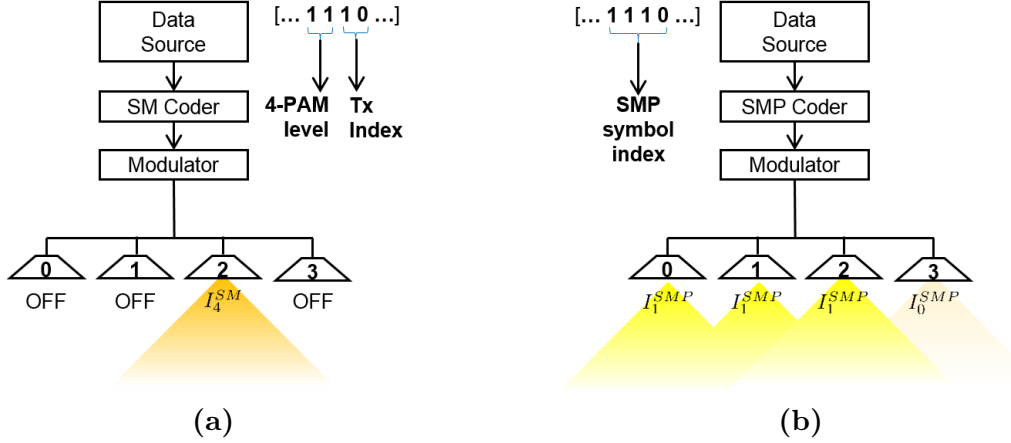


Figure 3.3: SM and SMP implementation block diagram for 4 bits/symbol (a) SM implementation with $N_{tx} = 4$ and $M = 4$ (b) SMP implementation with $N_{tx} = 4$ and $M = 2$

(3.15) where P_{avg}^{tx} is the average signal constraint to maintain desired illumination. Given a bit sequence forming a symbol [1 1 1 0], PAM level 3 (I_4^{SM}) is radiated using transmitter index 2.

$$P_x^{SM} = \frac{2P_{avg}^{tx}}{M+1} x; 1 \leq x \leq M \quad (3.15)$$

On the other hand, SMP uses M -ary modulation for each luminaire to transmit information. SMP with N_{tx} number of luminaires jointly generates $M^{N_{tx}}$ unique symbols. Each SMP symbol transmits $r = N_{tx} \log_2(M)$ bits. Each r bit long section of encoded information stream is then mapped to one of the $M^{N_{tx}}$ unique symbols. SMP for a setup with $N_{tx} = 4$ transmitters and 2-PAM is illustrated in Figure 3.3b. M -PAM intensity levels for SMP are selected as in (3.16) where P_{avg}^{tx} is the average signal constraint to maintain desired illumination. A bit sequence forming a symbol [1 1 1 0] is jointly mapped to the 15th out of $N_{tx} \log_2(M) = 16$ possible unique symbols.

$$P_x^{SMP} = \frac{2P_{avg}^{tx}}{M-1} x; 0 \leq x < M \quad (3.16)$$

For a channel with equally likely symbols, a maximum likelihood (ML) detector

is the optimal detector. If noise is AWGN, this reduces to nearest neighbor (NN) detection. Having observed \mathbf{Y} and knowing \mathbf{H} , estimated symbol $\hat{\mathbf{X}}$ is the symbol closest to observation \mathbf{Y} in Euclidean space. The signal detection can be written as

$$\begin{aligned}\hat{\mathbf{X}} &= \underset{\forall \mathbf{X}_i}{\operatorname{argmax}} p_{\mathbf{Y}|\mathbf{X}}(\mathbf{Y}|\mathbf{X}_i, \mathbf{H}) \\ &= \underset{\forall \mathbf{X}_i}{\operatorname{argmin}} \|\mathbf{Y} - \mathbf{H}\mathbf{X}_i\|_F\end{aligned}\quad (3.17)$$

where \mathbf{X}_i are the different symbols and $\|\cdot\|_F$ is the Frobenius norm.

In an indoor VLC system, luminaires need to maintain an average emitted radiant flux over different overlapping time windows so that the perceived illumination remains constant. Thus a fair performance comparison between different modulation schemes can be made when they emit the same radiant flux. Thus the SNR is defined as

$$\text{SNR} = \frac{(eP_{\text{avg}}^{\text{tx}})^2}{\sigma_n^2} \quad (3.18)$$

where $P_{\text{avg}}^{\text{tx}}$ is the average radiant flux emitted by a transmitter, e is the optical to electrical conversion factor ($\text{AW}^{-1}\Omega^{-2}$) and σ_n^2 is the noise power. Without loss of generality, $e = 1$ is assumed. This SNR definition is used in reference (Fath and Haas, 2013) and thus used here to demonstrate performance enhancement of SM and SMP systems with imaging receiver when compared to non-imaging receiver considered in the reference.

3.4 SM and SMP system performance with imaging receiver

The effects of varying transmitter array and imaging receiver configurations on the BER performance of SM and SMP systems are studied. An array of $N_{\text{tx}} = 4$ transmitters that are arranged on a regular grid with pitch P_{tx} is considered. To achieve 4 bits/sym, SM with $N_{\text{tx}} = 4$ and $M = 4$ -PAM and SMP with $N_{\text{tx}} = 4$ and $M = 2$ -

PAM are implemented. To achieve 8 bits/sym, SM with $N_{tx} = 4$ and $M = 64$ -PAM and SMP with $N_{tx} = 4$ and $M = 4$ -PAM are implemented. The vertical distance $\|\mathbf{d}_j^z\|$ between the transmitter and receiver planes is 2 m. Lambertian luminaires of order 1 are assumed to have a spectral power distribution that is approximated by a sum of Gaussians as in (Grubor et al., 2008). The effective responsivity of each pixel is equal to 0.4 A/W. Within this context, it is assumed that the pixel grid is large enough to ensure that each of the four spots fall on the sensor for each of the different configurations considered below.

Using the parameters specified above, the channel gains are of the order of 10^{-7} for all configurations. Thus the transmitted signal power is about 140 dB higher than the received signal power. Typically, the SNR is defined as the ratio of received signal power to noise power. However, given SNR as defined in Eq. (3.18), there is an offset of at least +140 dB over typical definition.

Imaging vs non-imaging receiver

Performance gains of using an imaging receiver over a non-imaging receiver are analyzed in this subsection. The transmitter and modulation parameters are the same as described above. For this analysis, $P_{tx} = 0.5$ m is considered. The non-imaging receiver is made up of 2×2 array of pixels; each with a side length of 1 mm and a pitch of 1 mm. Each pixel has a concentrator of refractive index 1.5 and FOV of 60 deg. For the imaging receiver, the sensor is modeled as 2×2 array of pixels with side length and pitch of 1 mm. The imaging lens is defined to have sufficient magnification to align the images of the four transmitters each with four pixels respectively. The FOV of the receiver changes with the sensor dimensions. The maximum FOV is defined as 60 deg; the same as in non-imaging receiver case. A fair performance comparison between the two receiver configurations can be made under the assumption that the same average signal radiant flux is incident on both. Thus, the aperture of

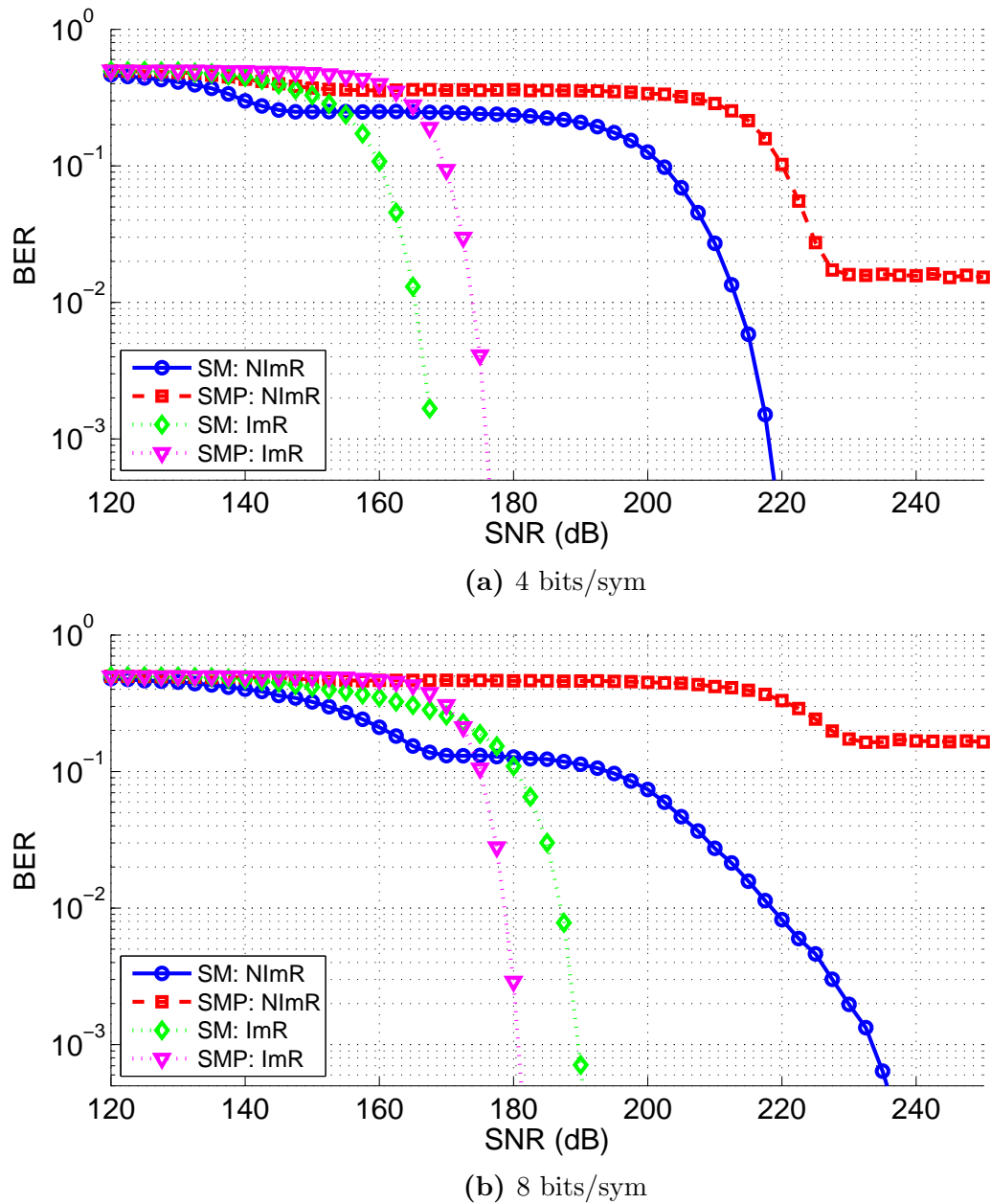


Figure 3·4: Performance comparison of SM and SMP using non-imaging (NImR) and imaging (ImR) receiver

the imaging receiver is modeled to have an area of 1 mm^2 .

BER vs SNR curves for SM and SMP using non-imaging receiver and imaging receiver are shown in Figure 3·4. At low average signal powers, using a non-imaging receiver, shot noise is the dominant source of noise. At high signal powers, ICI dominates the noise for the non-imaging receiver because the channel matrix coefficients are highly correlated (Zeng et al., 2009). This can be seen as two regions of the BER curves when using a non-imaging receiver. SM mitigates ICI and is thus more robust as compared to SMP in this scenario. BER achieved by SMP with non-imaging receiver are greater than 10^{-3} for the range of SNR considered and thus cannot be improved by forward error correction (FEC). SM needs a high transmit signal power to achieve $\text{BER} \leq 10^{-3}$ for both 4 and 8 bits/sym. Conversely, imaging receiver completely demultiplexes the four transmit signals while generating a diagonal channel matrix and thus avoids ICI under ideal setup. To achieve $\text{BER} = 10^{-3}$ at 4 bits/sym, SM with imaging receiver performs about 8 dB better than SMP with imaging receiver and about 45 dB better than SM with non-imaging receiver. SMP packs more bits spatially in transmitter location as compared to SM. Thus, to achieve higher spectral efficiency while keeping the number of transmitters the same, more M -ary PAM levels are needed for SM as compared to SMP thus quickly degrading SM's performance. To achieve $\text{BER} = 10^{-3}$ at 8 bits/sym, SMP with imaging receiver outperforms SM with imaging receiver by about 10 dB and SM with non-imaging receiver by about 52 dB. The channel matrix coefficient decorrelation afforded by imaging receiver provide huge SNR gains over non-imaging receiver for a given BER.

Varying α_s

For this analysis, α_s is varied while keeping δ_s and μ_s fixed. As illustrated in Figure 3·5, α_s affects only the spot size. As α_s increases, spots on the sensor overlap increasingly more number of pixels degrading the BER performance. Increasing the number

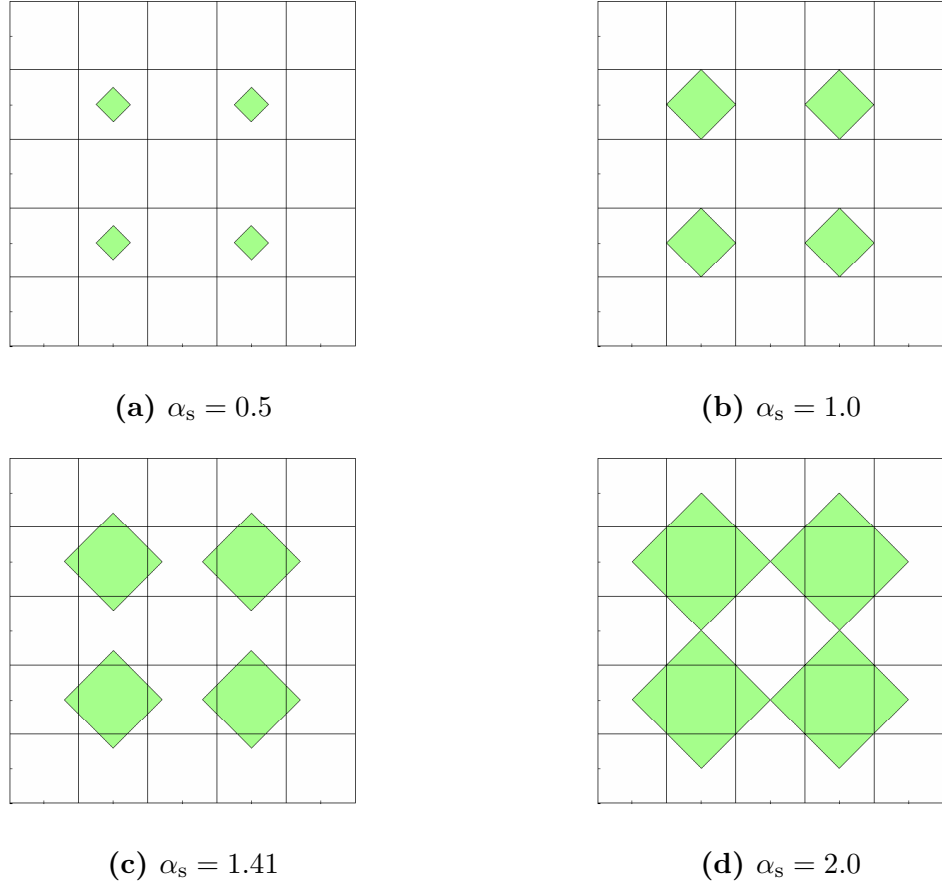


Figure 3.5: Spots on the sensor for different α_s

of pixels per spot also increases the noise for each link thus causing the drop in performance. Very small pixel sizes or very large transmitter sizes also cause increase in α_s . A smaller pixel size does enable the system to pack more channels provided α_s is relatively small. On the other hand, having very small pixel sizes or alternately large transmitter illumination surface tend to increase α_s and force the system to operate in a suboptimal configuration.

BER vs SNR curves for SM and SMP for different values of α_s are shown in Figure 3.6. To achieve $\text{BER} \leq 10^{-3}$ at 4 bits/sym, SNRs of about [168, 168, 170, 173] dB and [176, 176, 178, 181] dB are needed for $\alpha_s = [0.5, 1, 1.41, 2]$ with SM and SMP respectively. To achieve $\text{BER} \leq 10^{-3}$ at 8 bits/sym, SNRs of about [190, 190, 192,

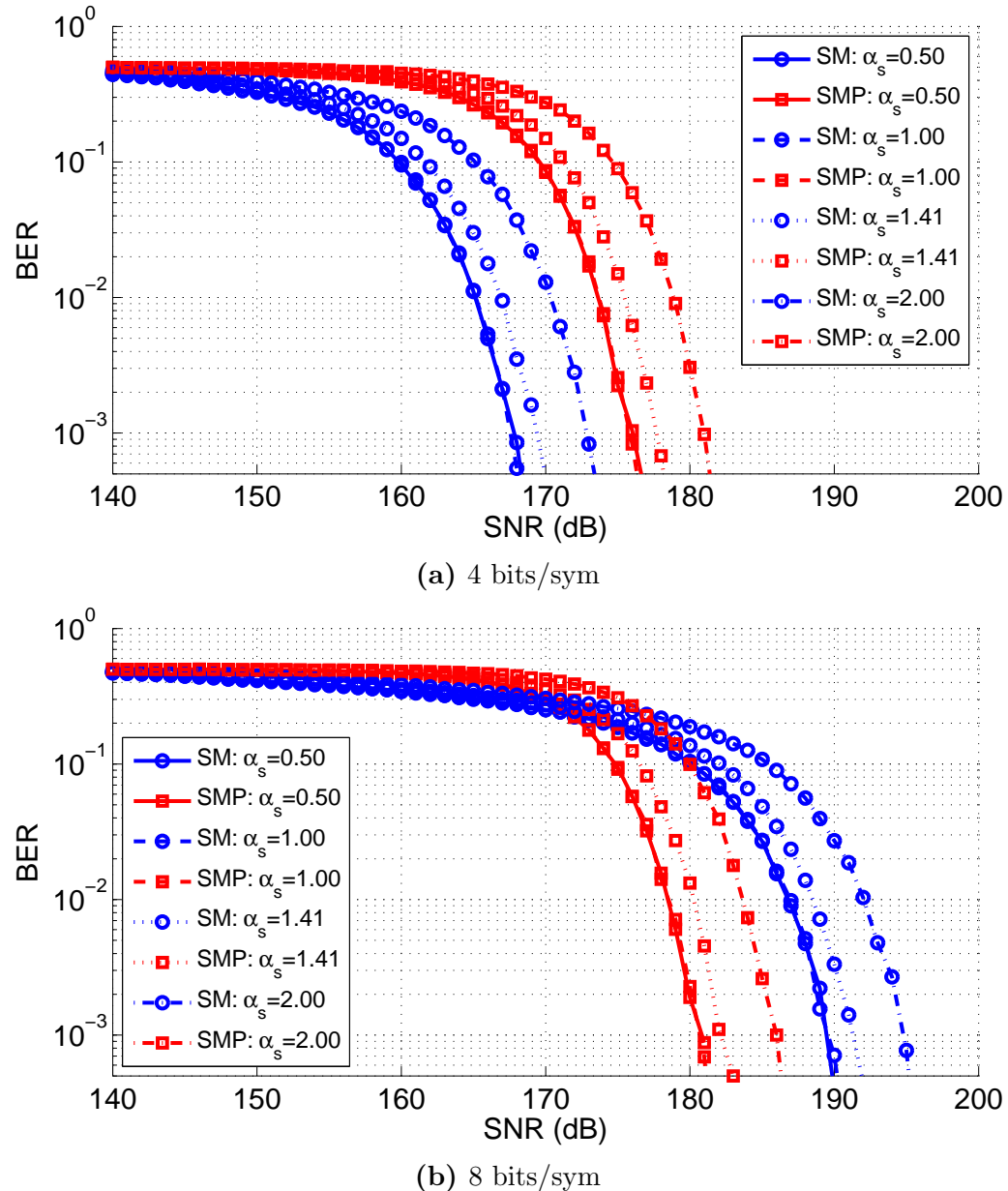


Figure 3.6: BER vs SNR for different α_s

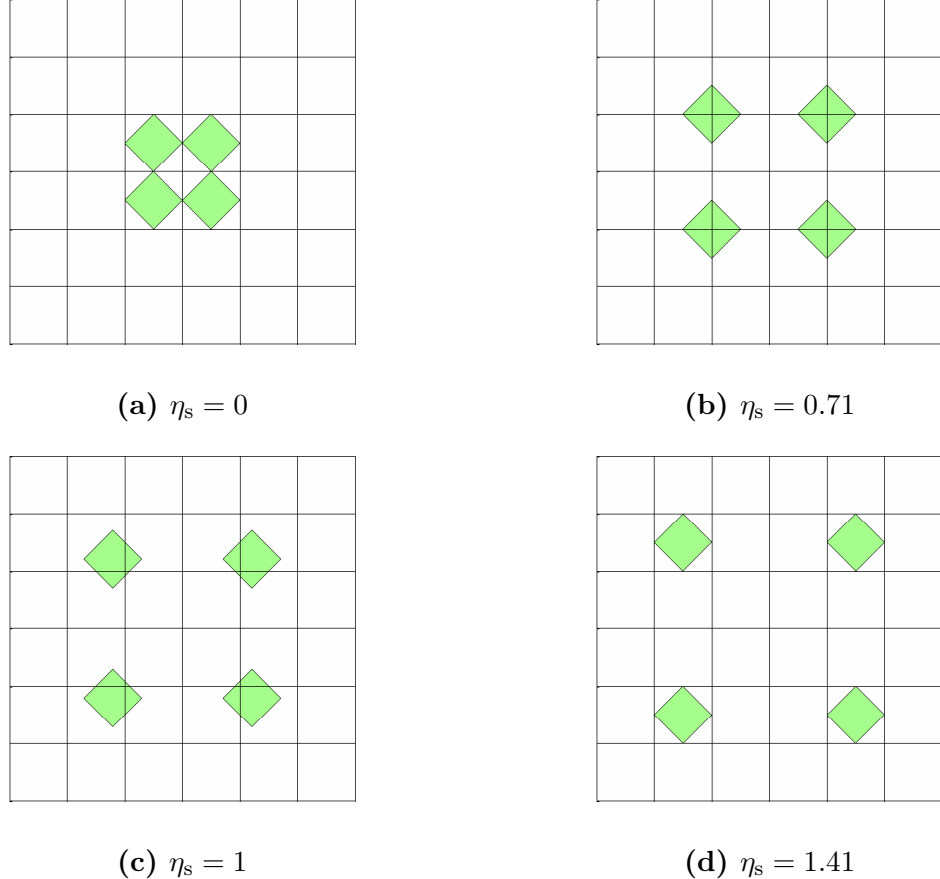


Figure 3.7: Spots on sensor for different η_s

195] dB and [181, 181, 183, 186] dB are needed for $\alpha_s = [0.5, 1, 1.41, 2]$ with SM and SMP respectively. Thus there is about a 2 dB SNR penalty for system operating at $\alpha_s = 1.41$ and 5 dB SNR penalty for system operating at $\alpha_s = 2$ as compared to that at $\alpha_s = 1$.

Varying η_s

For this analysis, η_s (alternately δ_s) is varied while keeping α_s and μ_s fixed. Thus only the effect of change in spot pitch affects the BER performance. As illustrated in Figure 3.7, as η_s increases, distance between the spots on the sensor increases as they push further apart.

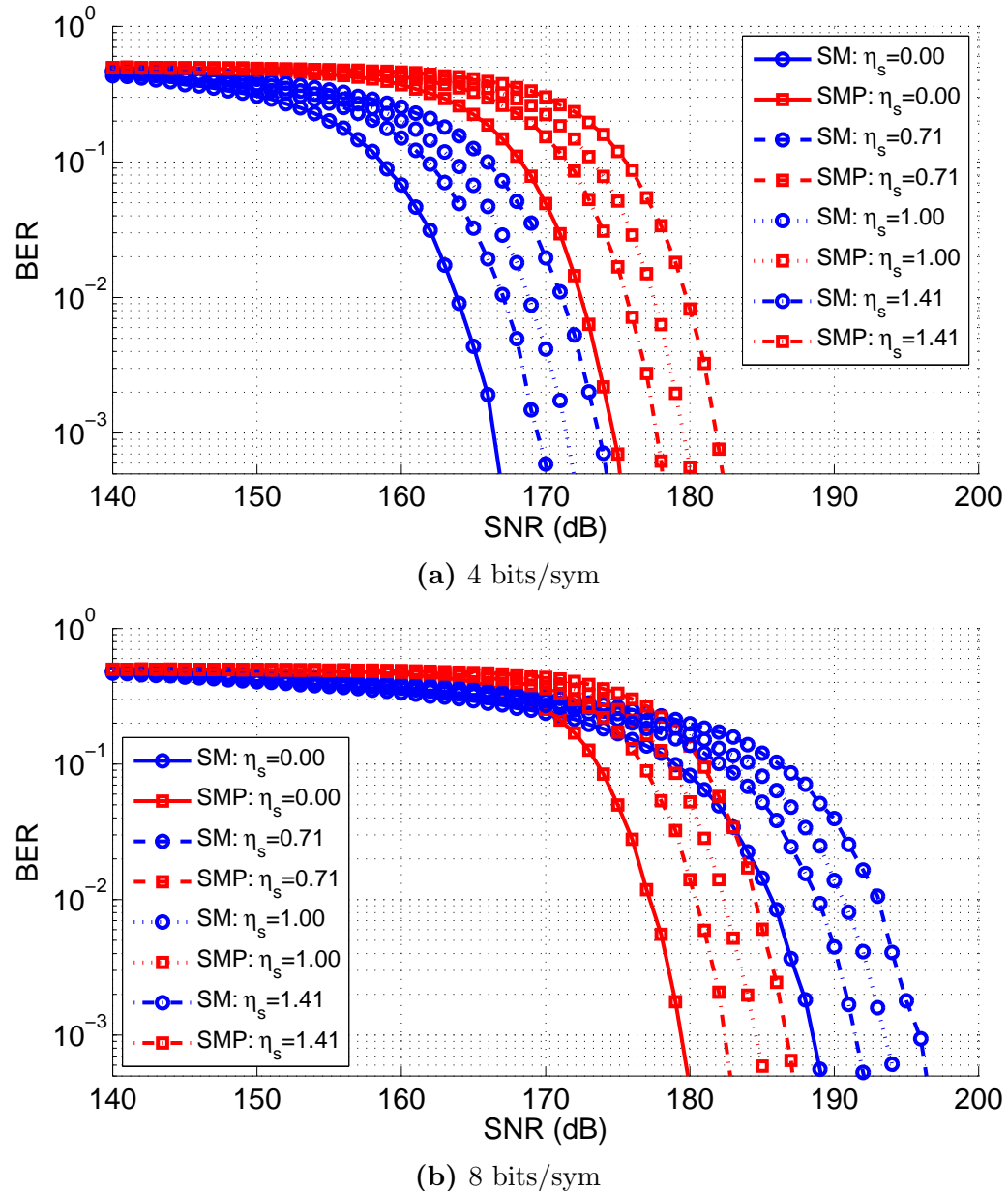


Figure 3.8: BER vs SNR for different η_s .

BER vs SNR curves for SM and SMP for different values of η_s are shown in Figure 3.8. To achieve $\text{BER} \leq 10^{-3}$ at 4 bits/sym, SNRs of about [167, 174, 172, 170] dB and [175, 182, 180, 178] dB are needed for $\eta_s = [0, 0.71, 1, 1.41]$ with SM and SMP respectively. To achieve $\text{BER} \leq 10^{-3}$ at 8 bits/sym, SNRs of about [189, 196, 194, 192] dB and [180, 187, 185, 183] dB are needed for $\eta_s = [0, 0.71, 1, 1.41]$ with SM and SMP respectively. We see that the BER performance is best when the spot overlaps minimum number of pixels and worst when the spot is centered at a corner of a pixel thus maximizing the number of pixels it overlaps with. In this setup, for $\text{BER} = 10^{-3}$, there is an SNR penalty of about 7 dB between the best and worst cases. The slight drop in performance for $\eta_s = 1.4$ as compared to $\eta_s = 0$ can be attributed to drop in free-space gain caused by the larger distance per link as a result of increased transmitter pitch.

Varying μ_s

In this analysis, μ_s is varied by varying focal length f . Alternately, it can be varied by changing length of optical axis $\|\mathbf{d}_j^z\|$. Varying μ_s affects both α_s and η_s simultaneously. This captures their combined impact on the BER performance. We see from Figure 3.9 that increasing μ_s not only increases the spot size but also pushes the spots away from each other. Note unlike in previous case, the transmitter pitch remains constant ($P_{tx} > 0$).

BER vs SNR curves for SM and SMP for different values of μ_s are shown in Figure 3.10. To achieve $\text{BER} = 10^{-3}$ at 4 bits/sym, SNRs of about [167, 173, 169, 173] dB and [175, 181, 177, 181] dB are needed for $\mu_s = [0.5, 1, 1.41, 2]$ with SM and SMP respectively. To achieve $\text{BER} = 10^{-3}$ at 8 bits/sym, SNRs of about [189, 195, 191, 195] dB and [180, 186, 182, 186] dB are needed for $\mu_s = [0.5, 1, 1.41, 2]$ with SM and SMP respectively.

The best performance is obtained for $\mu_s \leq 0.5$. This is because at this value of

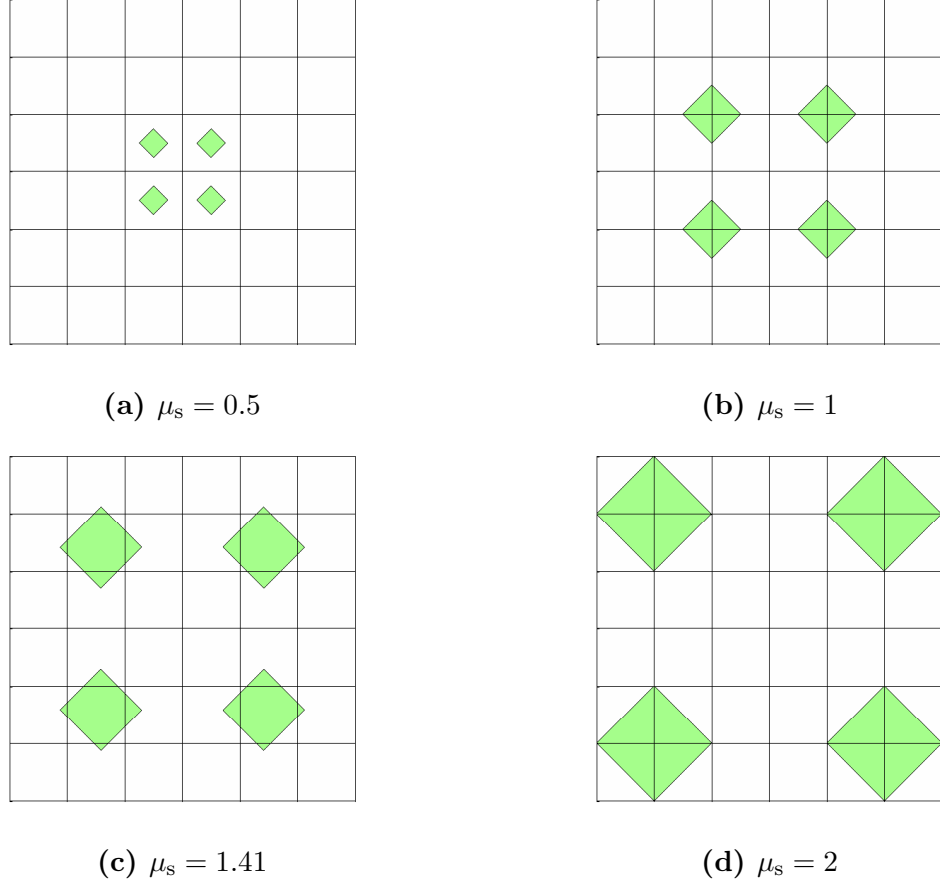


Figure 3.9: Spots on sensor for different μ_s

$\mu_s, \alpha_s < 1$ and η_s is such that all spots lie on different adjacent pixels. It can also be inferred that given enough transmitters in the room, at $\mu = 0.5$, every single pixel could get signal from a single transmitter thus greatly improving the capacity of the channel.

At lower bit rates, SM benefits from having higher transmit power per symbol at lower M -PAM level. To achieve higher bit-rates, higher M -PAM levels push the constellations closer to each other thus quickly degrade the SM performance as compared to SMP. As shown in Figure 3.6, Figure 3.8 and Figure 3.10, to achieve $\text{BER} = 10^{-3}$, at 4 bits/sym, SM performs 8-10 dB better while at 8 bits/sym, SMP performs 8-10 dB better.

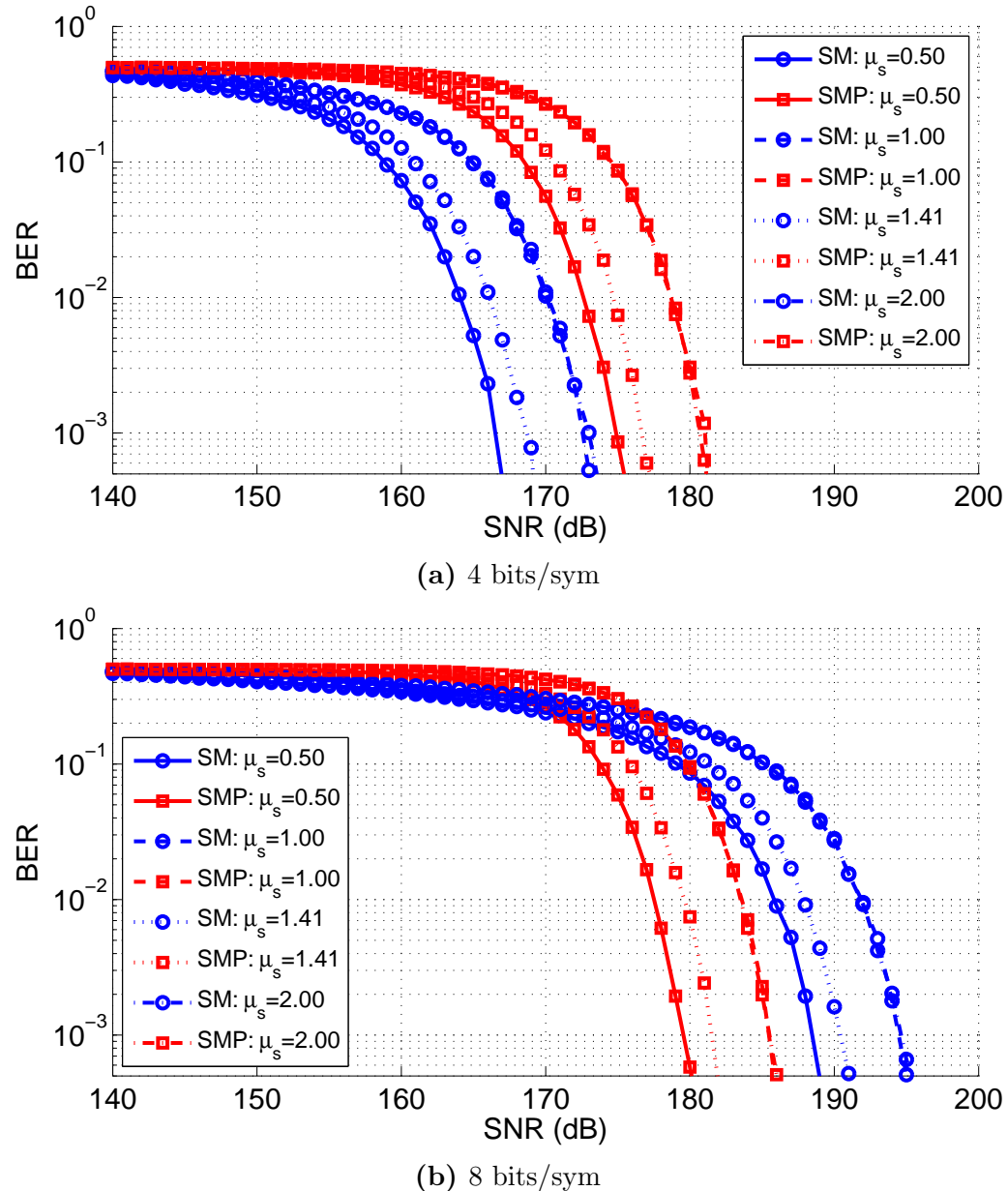


Figure 3.10: BER vs SNR for different μ_s

In this chapter, we investigated the use of SM and SMP with both imaging and non-imaging receivers in a MIMO VLC system. This effort was achieved via the creation of an analysis framework and normalization approach to enable performance characterization between systems. The results show that an imaging receiver provides significant SNR (≈ 45 dB) gains over non-imaging receiver for SM and SMP in a practical indoor scenario. For lower spectral efficiencies (4 bits/sym), SM performs 8-10 dB better than SMP while at higher spectral efficiencies (8 bits/sym), SMP gives 8-10 dB performance improvement. This is because the imaging receiver helps decorrelate the parallel channel gains as compared to non-imaging receiver. To achieve ideal performance for a given indoor configuration, parameters α_s , η_s and μ_s should be carefully selected. From the simulations we can conclude that the imaging MIMO system performs best when a spot is completely enveloped by a single pixel and adjacent spots each lie on adjacent pixels. For the simulation cases considered, $\alpha_s \leq 1$, $\eta_s = 0$ and $\mu_s = 0.5$ were found to provide the best system performance.

Chapter 4

Sample indexed spatial orthogonal frequency division multiplexing

SM is a multiple-transmitter technique that can provide higher data rates with low system complexity as compared with SISO systems. OFDM is widely implemented to achieve better spectral efficiency in wireless channels. An approach to combine SM and traditional OFDM is proposed in reference (Ganesan et al., 2006). In this chapter, sample indexed spatial OFDM (SIS-OFDM)¹ is proposed to combine SM and O-OFDM in a novel way and achieve significant performance gain. By assigning time-domain samples of the O-OFDM transmit symbol to different transmitters, SIS-OFDM achieves much better spectral efficiency and reduces computational complexity at the transmitter as compared with previous work in reference (Zhang et al., 2012) that combines SM with O-OFDM in the frequency domain. We also consider the impact of optical source biasing on overall performance, and the relative performance of imaging receiver versus non-imaging receiver design for our proposed SIS-OFDM technique. Results indicate that for an $N_{\text{tx}} \times N_{\text{rx}}$ where $N_{\text{tx}} = N_{\text{rx}} = 4$, SIS-OFDM using imaging receiver can achieve up to 135 dB of SNR gain over comparable system using a non-imaging receiver. Also, using N_{sc} number of O-OFDM subcarriers provides up to $N_{\text{sc}} \times \log_2(N_{\text{tx}})$ additional bits/symbol of spectral efficiency over techniques that combine SM and O-OFDM in the frequency domain.

¹This work is published in peer-reviewed article (Butala et al., 2014a).

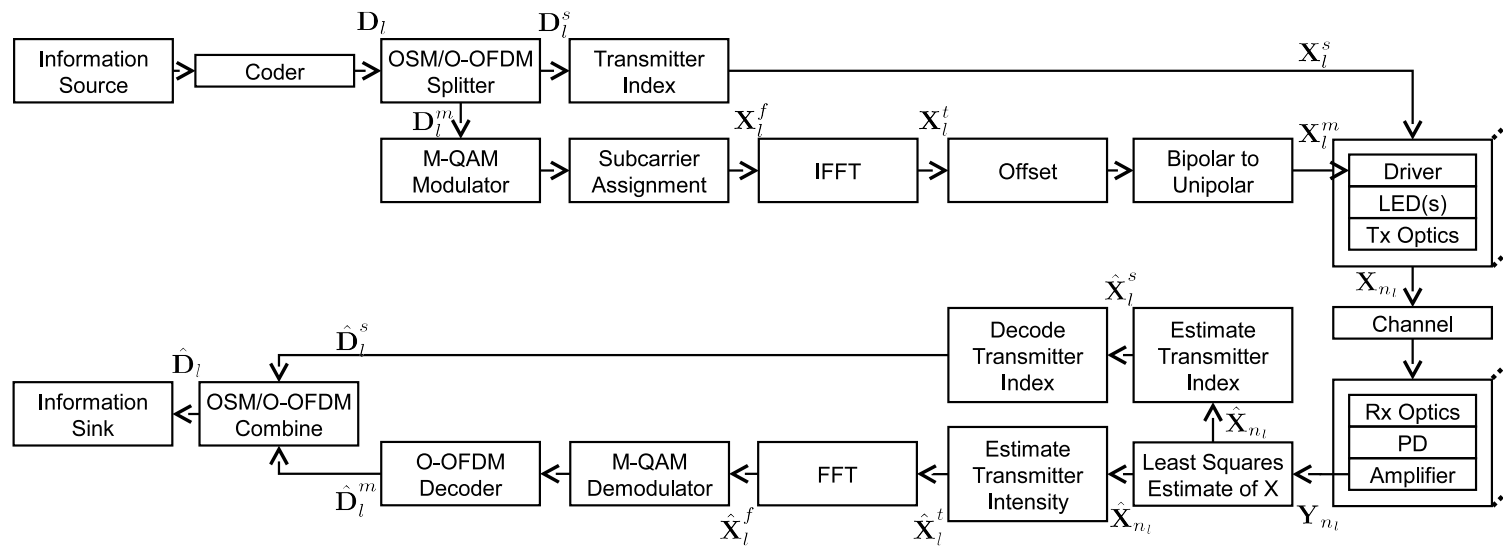


Figure 4.1: SIS-OFDM system block diagram

4.1 SIS-OFDM system outline

Here, an encoded information stream is divided into O-OFDM and SM streams. Data from O-OFDM stream is assigned to different subcarriers to form the frequency domain O-OFDM symbol. SM is then implemented in the frequency domain where each data subcarrier is assigned to a transmitter determined by the encoded SM stream. An IFFT operation is implemented at each transmitter to multiplex the data before transmission. Spectral efficiency of this scheme is then proportional to the number of data subcarriers. In comparison, the spectral efficiency of SISO OFDM is proportional to the number of total subcarriers which is equal to at least double the number of data subcarriers. Additionally, the SIS-OFDM system requires a single IFFT operation, independent of the number of transmitters and thus maintains a computational complexity equal to that of SISO OFDM transmission. SIS-OFDM using an imaging receiver achieves much better power efficiency as compared to equivalent system using non-imaging receiver.

Implementation of SISO O-OFDM system is outlined in subsection 2.5.4. The number of data subcarriers, N_{sc}^d , equals $(N_{sc}/4)$ for ACO-OFDM and $(N_{sc}/2 - 1)$ for DCO-OFDM where N_{sc} is the total number of subcarriers. The number of transmitted bits per O-OFDM symbol is given by $R^m = N_{sc}^d \times \log_2(M)$. Figure 4.1 illustrates the block diagram of a system implementing SIS-OFDM. The source generates the information to transmit. The coder encodes the information into a binary bit-stream \mathbf{D} which is divided into consecutive segments of $R^{ms} = R^m + R^s$ bits where $R^s = N_{sc} \times k = N_{sc} \times \log_2(N_{tx})$ is the number of spatial bits. Let the l^{th} such segment be denoted by \mathbf{D}_l . The first R^m bits of \mathbf{D}_l are collected in a vector \mathbf{D}_l^m and are mapped to an M -QAM modulator. The generated QAM symbols are then assigned to subcarriers (based on the O-OFDM signal format, *i.e.* DCO-OFDM or ACO-OFDM) to generate a frequency domain O-OFDM symbol \mathbf{X}_l^f of length N_{sc} . An IFFT operation is applied

on \mathbf{X}_l^f to produce a real-valued bipolar time domain O-OFDM symbol \mathbf{X}_l^t of the same length N_{sc} . The latter R^s bits of \mathbf{D}_l are collected in a vector \mathbf{D}_l^s and are mapped to N_{sc} length transmitter index vector denoted by \mathbf{X}_l^s . Let \mathbf{X}_l^m denote the real unipolar baseband signal after biasing and/or clipping, and $0 \leq n_l \leq (N_{sc} - 1)$ indicate the relative time index for the next SIS-OFDM symbol to be transmitted. At each time instance, an O-OFDM signal value from \mathbf{X}_l^m is transmitted from a luminaire indexed by \mathbf{X}_l^s . Let \mathbf{X}_{n_l} be this N_{tx} length transmission vector at time instant n_l . Thus the j^{th} element of this vector is then given by

$$\mathbf{X}_{n_l}(j) = \begin{cases} \mathbf{X}_l^m(n_l) & ; j = \mathbf{X}_l^s(n_l) \\ 0 & ; \text{else} \end{cases} \quad (4.1)$$

The SIS-OFDM symbol and transmit vector generation is explained using the following example which considers ACO-OFDM with $N_{sc} = 8$, 4-QAM subcarrier modulation and $N_{tx} = 2$. Here, $R^m = 4$ and $R^s = 8$, *i.e.* $R^{ms} = 4 + 8 = 12$ bits per SIS-OFDM symbol. The randomly generated example bits forming one SIS-OFDM symbol \mathbf{D}_l are shown in Table 4.1. Table 4.2 then illustrates the data to subcarrier and transmitter index assignments. In this example, the transmitters would jointly transmit vector $\mathbf{X}_{n_l} = [0 \sqrt{2}]^T$ at relative time index $n_l = 2$.

The indoor optical MIMO channel is modeled as,

$$\mathbf{Y}_{n_l} = \mathbf{H}\mathbf{X}_{n_l} + \mathbf{W}_{n_l} \quad (4.2)$$

where \mathbf{X}_{n_l} is the instantaneous transmit vector. \mathbf{H} is the channel matrix and can be computed as in Eq. (3.7). \mathbf{Y}_{n_l} is the received signal vector and \mathbf{W}_{n_l} is zero-mean AWGN vector.

The pseudo-inverse of channel matrix is given by $(\mathbf{H}^*\mathbf{H})^{-1}\mathbf{H}^*$. Using this, the

Stream	Bits
\mathbf{D}_l	$[1\ 1\ 0\ 0\ 0\ 1\ 1\ 0\ 0\ 0\ 1\ 1]^T$
\mathbf{D}_l^m	$[1\ 1\ 0\ 0]^T$
\mathbf{D}_l^s	$[0\ 1\ 1\ 0\ 0\ 0\ 1\ 1]^T$

Table 4.1: Example SIS-OFDM data streams using ACO-OFDM

n_l	OFDM bits	\mathbf{X}_l^f	\mathbf{X}_l^t	\mathbf{X}_l^m	SM bits	\mathbf{X}_l^s
0	-	0	0	0	0	1
1	1 1	$-1 - j$	-1	0	1	2
2	-	0	$\sqrt{2}$	$\sqrt{2}$	1	2
3	0 0	$1 + j$	1	1	0	1
4	-	0	0	0	0	1
5	-	$1 - j$	1	1	0	1
6	-	0	$-\sqrt{2}$	0	1	2
7	-	$-1 + j$	-1	0	1	2

Table 4.2: Example SIS-OFDM subcarrier and luminaire assignment

least squares estimate of transmitted vector \mathbf{X}_{n_l} can be computed as

$$\hat{\mathbf{X}}_{n_l} = (\mathbf{H}^* \mathbf{H})^{-1} \mathbf{H}^* \mathbf{Y}_{n_l} \quad (4.3)$$

In SIS-OFDM, only one luminaire emits radiant flux at a given time instance. Thus the maximum element of $\hat{\mathbf{X}}_{n_l}$ is estimated as the transmitted signal flux $\hat{x}_{n_l}^m$.

$$\hat{x}_{n_l}^m = \max_{\forall j} (x_j) ; x_j \in \hat{\mathbf{X}}_{n_l} \quad (4.4)$$

The index of $\hat{x}_{n_l}^m$ within $\hat{\mathbf{X}}_{n_l}$ provides the estimate of the active luminaire. Thus the instantaneous luminaire index $\hat{x}_{n_l}^s$ is estimated as

$$\hat{x}_{n_l}^s = \operatorname{idxmax}_{\forall j} (x_j) ; x_j \in \hat{\mathbf{X}}_{n_l} \quad (4.5)$$

A SIS-OFDM symbol is transmitted over N_{sc} time slots. $\hat{x}_{n_l}^m$ and $\hat{x}_{n_l}^s$ are estimated for each time slot n_l and collected in vectors $\hat{\mathbf{X}}_l^m$ and $\hat{\mathbf{X}}_l^s$ respectively. $\hat{\mathbf{X}}_l^m$ is subject

to signal processing similar to SISO O-OFDM reception techniques to recover the transmitted O-OFDM signal in $\hat{\mathbf{X}}_l^t$. An FFT process then demultiplexes the data and estimates the transmitted O-OFDM symbol in $\hat{\mathbf{X}}_l^f$. ML estimation is performed on the received symbols over the N_{sc}^d data subcarriers to estimate the bits transmitted and collected in $\hat{\mathbf{D}}_l^m$. The transmitter indexes estimated in $\hat{\mathbf{X}}_l^s$ are subject to decimal to k -length binary conversion to decode the spatial bits as $\hat{\mathbf{D}}_l^s$. The estimated SM and O-OFDM bits are then combined to estimate the transmitted l^{th} bit-stream as $\hat{\mathbf{D}}_l$.

The SIS-OFDM scheme explained above can provide up to R^s additional bits per symbol over equivalent SISO O-OFDM techniques. The system explored in (Zhang et al., 2012) can transmit $(N_{sc}^d \times k)$ spatial-bits per symbol as compared to $(N_{sc} \times k)$ spatial-bits per symbol in SIS-OFDM. Thus using SIS-OFDM provides additional spectral efficiency gain of $(3 \times N_{sc} \times k/4)$ bits per symbol while using ACO-OFDM and $((N_{sc}/2 - 1) \times k)$ bits per symbol while using DCO-OFDM.

4.2 SIS-OFDM system performance

Two comparable 4×4 MIMO systems implementing SIS-OFDM with ACO-OFDM and DCO-OFDM are considered to evaluate the system performance using imaging and non-imaging receiver. The $N_{tx} = 4$ lambertian transmitters of order 1 are assumed located on the ceiling of a room, facing vertically down, and at 0.5 m pitch. The transmitters are assumed to have a linear E/O conversion and transmit the upper peak signals without clipping. A 4-pixel imaging receiver with 1 mm pixel side length is assumed to have optics with 5 mm focal length, aperture of 1 mm² area and arranged in a 2×2 grid. A 4-element non-imaging receiver is modeled to have 4 photodiodes of side length 1 mm, pitch of 1 mm, and a concentrator with 1.5 refractive index arranged in a 2×2 grid. The receivers are assumed located in the

center, facing upwards, and at a distance of 2 m from the transmitter plane. The transmitter side length is assumed small enough that its image lies entirely inside the corresponding pixel of the imaging receiver. Additionally, these MIMO systems are compared against an equivalent SISO system that receives the same amount of average optical flux as in the MIMO systems.

In an indoor VLC environment, the propagation delay of light rays from luminaires to receiver is of the order of a few nano-seconds whereas the modulation bandwidth is of the order of few tens of mega-Hertz. Additionally, the multipath reflected signals undergo path-loss of the order of 100 dB as compared to LOS signals. Thus only LOS signals are considered. In such scenario, channel matrix \mathbf{H} for the described system setup with the imaging receiver is given by Eq. (4.6a), with non-imaging receiver is given by Eq. (4.6b) and for the SISO system is 0.8979×10^{-7} . Note, in SIS-OFDM, since only 1 luminaire is active at a given time, the average transmitted flux per luminaire is assumed same as in the SISO system. Since all systems must receive the same amount of flux at same illumination levels, the point-to-point channel gains in each case are similar.

$$\mathbf{H} = 10^{-7} \times \begin{bmatrix} 0 & 0 & 0 & 0.8979 \\ 0 & 0 & 0.8979 & 0 \\ 0 & 0.8979 & 0 & 0 \\ 0.8979 & 0 & 0 & 0 \end{bmatrix} \quad (4.6a)$$

$$\mathbf{H} = 10^{-7} \times \begin{bmatrix} 0.8981 & 0.8979 & 0.8979 & 0.8977 \\ 0.8979 & 0.8981 & 0.8977 & 0.8979 \\ 0.8979 & 0.8977 & 0.8981 & 0.8979 \\ 0.8977 & 0.8979 & 0.8979 & 0.8981 \end{bmatrix} \quad (4.6b)$$

As mentioned before, for indoor VLC, transmitters must perform dual function of providing wireless data communication while maintaining appropriate average illu-

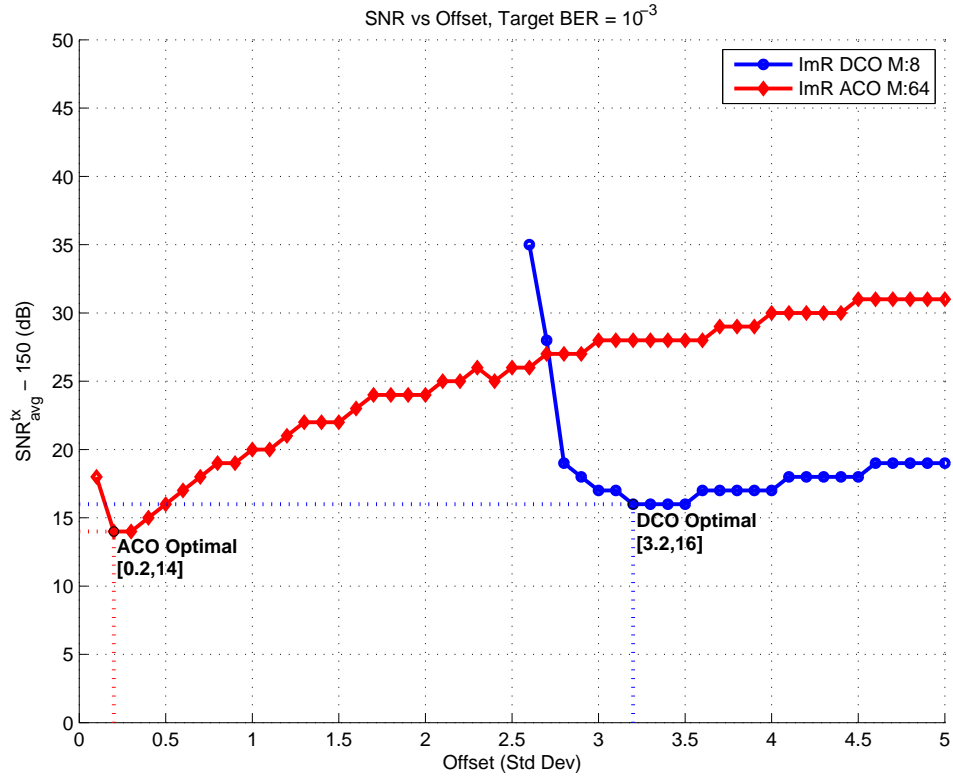


Figure 4.2: SNR vs DC Offset for target $\text{BER} = 10^{-3}$ using an imaging receiver

mation level. Thus, to perform a fair comparison between SIS-OFDM systems implementing ACO-OFDM and DCO-OFDM, both techniques are compared at the same average emitted flux levels while maintaining almost equal bit-rates. For this work SNR is defined as in Eq. (3.18). Given the channel matrix in (4.6), the definition of SNR in (3.18) has an SNR offset of ≈ 150 dB over received signal power to noise power ratio. Using $N_{\text{sc}} = 64$, performance of ACO-OFDM with 16-QAM and 64-QAM is compared to that of DCO-OFDM with 4-QAM and 8-QAM respectively. This results in 192, 224, 190, and 221 bits per symbol respectively for the four configurations.

The effect of DC bias on system performance is studied using SNR vs DC offset curves to achieve a target $\text{BER} = 10^{-3}$ and is illustrated in Figure 4.2. The DC offset

is set as a multiple of the SD of the O-OFDM signal; similar to SISO O-OFDM techniques. In ACO-OFDM, all time-domain samples are clipped at zero thus increasing the probability of having active luminaires which don't emit any radiant flux. In this case, the receiver cannot identify the active luminaire, introducing significant errors in spatial-bit estimation. To deal with this issue, we apply a DC offset to ensure active luminaires emit a minimum radiant flux corresponding to the chosen offset. As the offset increases, the minimum flux received from the active transmitter progressively increases and thus improving error performance in determining the luminaire index. The optimal offset is empirically estimated to be $0.2 \times \text{SD}$ for ACO-OFDM with 64-QAM subcarrier modulation. Further increasing the offset value quickly gives diminishing returns in luminaire index detection. For DCO-OFDM, noise induced due to clipping of negative samples is not orthogonal to data subcarriers. Thus at small offsets, a large proportion of signal gets clipped causing significant bit errors. The simulations confirm that an offset of $3.2 \times \text{SD}$ is needed to sustain a link using DCO-OFDM.

Different SIS-OFDM systems are compared at their optimal DC offsets as empirically determined from Figure 4·2. BER vs SNR curves at optimal DC offsets equal to $0.2 \times \text{SD}$ for ACO-OFDM with 64-QAM subcarrier modulation and $3.2 \times \text{SD}$ for DCO-OFDM with 8-QAM subcarrier modulation using imaging receiver and non-imaging receiver are illustrated in Figure 4·3. It is shown that using imaging receiver can provide significant SNR gain (≈ 135 dB) over non-imaging receiver for $\text{BER} = 10^{-3}$. For the non-imaging receiver, each PD receives significant signal from each of the 4 luminaires and thus high ICI is expected. The imaging receiver provides channel decorrelation thus significantly improving the system performance. As seen from the figure, it is impractical to achieve ≈ 150 dB SNR for SIS-OFDM with non-imaging receiver. The above SIS-OFDM configurations are compared with reference SISO

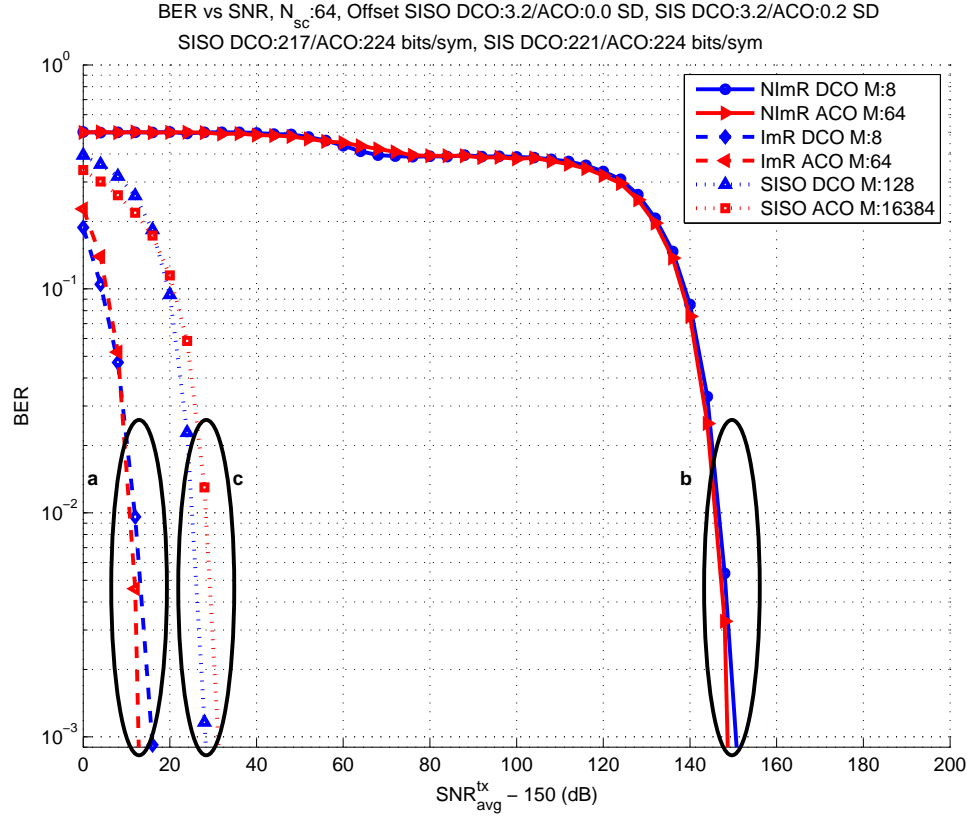


Figure 4.3: BER vs SNR performance comparisons for (a) SIS-OFDM with imaging receiver (b) SIS-OFDM with non-imaging receiver (c) SISO-OFDM

O-OFDM systems. To achieve nearly the same bits/symbol as in the SIS-OFDM systems, DCO-OFDM with 128-QAM subcarrier modulation and ACO-OFDM with 128^2 -QAM subcarrier modulation yielding 217 and 224 bits/symbol are required. With small form factor SISO receivers, it is nearly impractical to achieve ≈ 30 dB SNR to achieve target BER performance at comparable spectral efficiencies for SISO O-OFDM systems with higher order subcarrier modulation. The SIS-OFDM system with imaging receiver not only provides better spectral efficiency but also achieves the target BER at lower transmit powers. Additionally, the imaging receiver considered has practical dimensions and can be incorporated in portable devices.

BER vs SNR curves for individual O-OFDM and SM streams for the SIS-OFDM

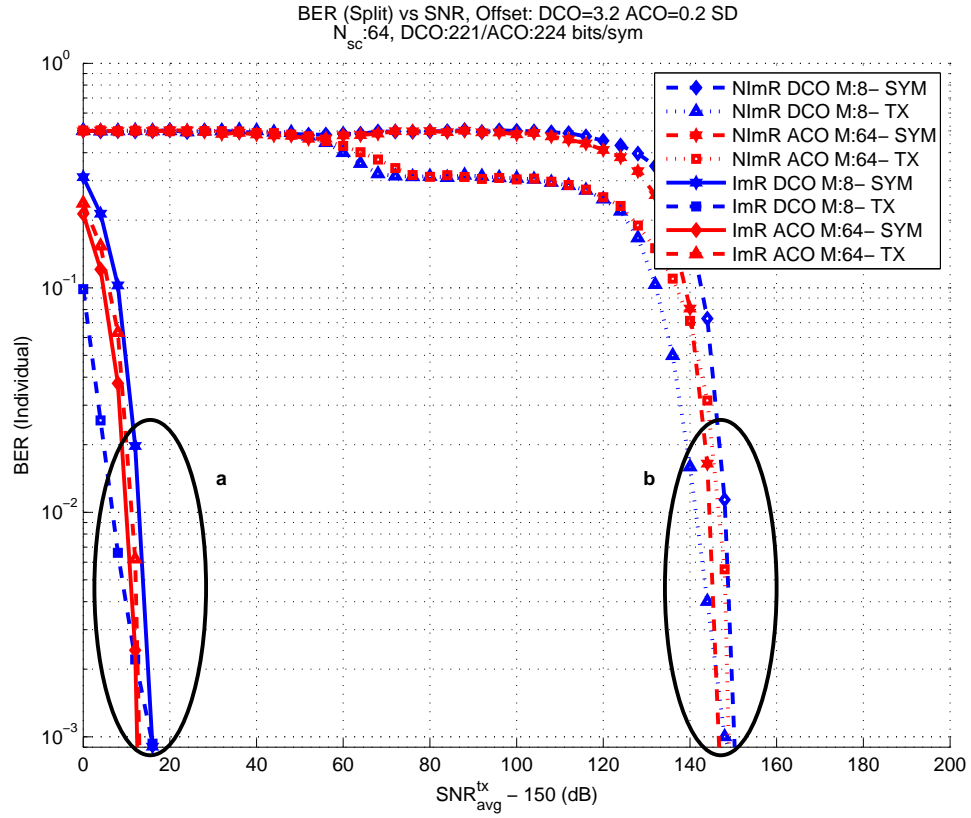


Figure 4.4: BER vs SNR performance comparison of SIS-OFDM spatial (TX) and OFDM (SYM) streams with (a) imaging receiver and (b) non-imaging receiver

systems considered are shown in Figure 4.4. At low SNR, bit errors are dominated by errors in luminaire index detection. Errors in luminaire index leads to choosing a different signal value for decoding the O-OFDM signal, thus introducing additional errors in O-OFDM signal decoding. As the SNR increases, errors in transmitter index detection significantly decrease and errors in O-OFDM symbol decoding dominates the BER. As the SNR is further increased, errors in the O-OFDM symbol decoding decrease thus reducing the overall BER.

In conclusion, it is shown that a system implementing SIS-OFDM can achieve additional $R^s = N_{sc} \times \log_2(N_{tx})$ bits per symbol of spectral efficiency as compared to SISO O-OFDM systems. Results indicate that the use of an imaging receiver provides

additional channel decorrelation and can help achieve up to 130 dB improvement in SNR when compared to system performance using a non-imaging receiver. At significantly lower computational complexity, the SIS-OFDM can provide an additional $(3 \times N_{sc} \times k/4)$ bits per symbol for ACO-OFDM and $((N_{sc}/2 - 1) \times k)$ bits per symbol for DCO-OFDM over recently proposed approaches that combine SM with O-OFDM.

Chapter 5

Impact of visual perception on CSK

As seen in previous chapter, imaging receivers have the potential to provide significant performance gains for a spatial MIMO OWC system. To incorporate these in portable devices, they must address challenges of being low powered, have fast sampling rates while incorporating optics, sensor and electronics in a small form factor.

The IEEE 802.15.7 standard defines specifications for short-range OWC using visible light. The standard specifies CSK as the preferred modulation scheme for indoor OWC while simultaneously providing illumination. This chapter considers the performance of M -ary CSK under the linear system model as specified in the standard. In light of illumination requirements, human eye's optical perception introduces unique non-linearities in the CSK signaling chain. It is shown that these non-linearities introduce performance penalties of more than 15 dB, 10 dB, and 5 dB for $M = 4$, 8, and 16 CSK respectively. A new metric called LSNR is also introduced to fairly compare performance of any two OWC signaling schemes operating at a user defined illumination intensity level and is used to compare performance of M -ary CSK implemented with different colored sources. At a target BER $\leq 10^{-3}$, simulation results indicate that clipping negative receiver output does not have an impact on M -ary CSK performance.

5.1 IEEE 802.15.7 - PHY III

LED based luminaires are energy efficient and are thus being widely adopted in indoor spaces to provide illumination. In order to dynamically control the rendered illumination spectrum, luminaires contain multiple elements of at least three colors of LEDs. Different SPDs can be rendered by mixing different ratios of radiant flux emitted from the multiple LEDs comprising a luminaire. Each resulting SPD realizes a different color mix to the human eye.

Any SPD within the visible range of electromagnetic spectrum can produce a stimulus when incident on the sensors of the human eye (rod and cones) and has a color associated with it. This color can also be represented by its intensity, hue and saturation. While intensity is a measure of the total power comprising the SPD, hue and saturation are subjective parameters analogous to mean and spread of the wavelengths comprising the SPD and are quantified by a chromaticity coordinate. The *commission internationale de l'éclairage* (CIE) has specified the CIE 1931 XYZ color space (CIE-CS) that provides a mathematical model to represent the chromaticity of radiation in the visible range as a point in a 2-dimensional plane. Let a luminaire be comprised of three types of LEDs, namely LED_n ; $n \in \{i, j, k\}$. The chromaticity of each LED can be represented by a coordinate (x_n, y_n) on the CIE-CS. When different intensities of radiant flux emitted by three types of LEDs are combined, the chromaticity coordinate of the resultant SPD will lie inside the triangle formed by coordinates of the LEDs themselves.

The IEEE standard for short-range OWC using visible light specifies CSK as the modulation technique of choice under the PHY III specifications (IEEE 802.15.7, 2011). For the rest of this chapter, the noun ‘standard’ shall imply the IEEE 802.15.7 standard, specifically chapter 12 on PHY III specifications. The standard outlines linear system configurations with M -ary CSK to achieve up to 96 Mb/s data rate.

CB_u	Band (nm)	Center (nm)	x	y
CB_0	380 - 478	429	0.169	0.007
CB_1	478 - 540	509	0.011	0.733
CB_2	540 - 588	564	0.402	0.597
CB_3	588 - 633	611	0.669	0.331
CB_4	633 - 679	656	0.729	0.271
CB_5	679 - 726	703	0.734	0.265
CB_6	726 - 780	753	0.734	0.265

Table 5.1: Color bands as outlined in IEEE 802.15.7

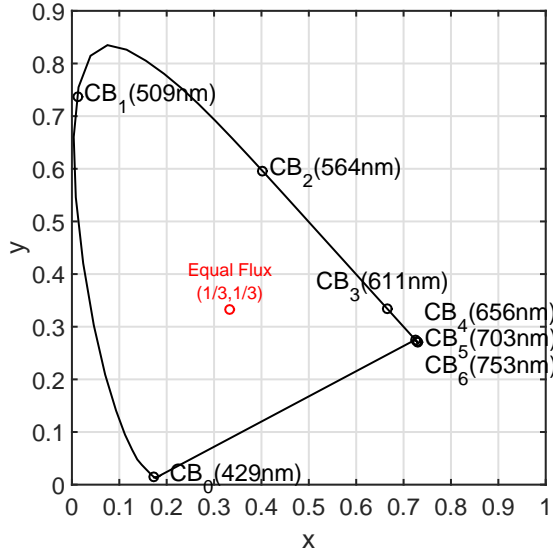


Figure 5.1: Color band centers on CIE-CS

Reference (Rajagopal et al., 2012) provides an overview of modulation and dimming techniques specified within the standard while reference (Singh et al., 2013) studies select color bands for CSK.

CSK is a modulation technique in which information is transmitted through changes in chromaticity coordinates. This can be achieved by varying the intensities of LED_n over time. To select sources for CSK implementation, the standard specifies 7 different color bands - CB_u ; $0 \leq u < 7$ by splicing the visible spectrum

Color band combination CBC_v	Color band 'u' for CBC _v		
	Band i	Band j	Band k
CBC ₁	6	2	0
CBC ₂	6	1	0
CBC ₃	5	2	0
CBC ₄	5	1	0
CBC ₅	4	2	0
CBC ₆	4	1	0
CBC ₇	3	2	0
CBC ₈	3	1	0
CBC ₉	2	1	0

Table 5.2: Color bands combinations as outlined in IEEE 802.15.7

range into 7 contiguous segments as shown in Table 5.1. The center wavelength of each segment as represented on CIE-CS is illustrated in Figure 5.1. Note that even though center wavelengths of CB₄, CB₅ and CB₆ are 47 nm – 50 nm apart, the distance between their chromaticity coordinates is very small. The CIE-CS is designed such that the SPD resulting from identical flux emitted by the three primary sources maps to coordinate (1/3, 1/3) which is shown in Figure 5.1. We can define a color sector on the CIE-CS as the region enclosed by a color band on the perimeter and coordinate (1/3, 1/3). Though not explicitly mentioned in the standard, it is assumed that SPD of each LED_n must belong to a different color sector. To study the performance of CSK independent of specific LED characteristics, it is generally assumed that the chromaticity coordinate of an LED belonging to a color sector corresponds to the center wavelength of a color band CB_u at the perimeter of the sector as illustrated in Figure 5.1.

To implement CSK using 3 types of LEDs, the standard defines different sets of 3 color bands and calls each set a color band combination (CBC). The 3 different types of LEDs forming a CBC are ordered in a descending manner based on the center wavelength of the color band they belong to and each such band is called ‘band i’,

m	M = 4	M = 8	M = 16
0	C_j^v	$(2C_4+C_5)/3$	C_j^v
1	$(C_i^v+C_j^v+C_k^v)/3$	$(2C_a+C_b)/3; C_a=(C_b+C_3+C_5)/3; C_b=(C_4+C_5)/2$	$(C_0+C_3+C_5)/3$
2	C_k^v	$(2C_a+C_b)/3; C_a=(C_b+C_3+C_7)/3; C_b=(C_4+C_7)/2$	$(C_3+C_6+C_{10})/3$
3	C_i^v	$(C_5+C_7)/2$	$(2C_0+C_9)/3$
4		C_j^v	$(C_0+2C_8)/3$
5		C_k^v	$(2C_0+C_8)/3$
6		$(2C_4+C_7)/3$	$(C_0+C_8+C_9)/3$
7		C_i^v	$(C_4+C_5+C_6)/3$
8			C_i^v
9			C_k^v
10			$(C_0+2C_9)/3$
11			$(C_9+C_{10}+C_{15})/3$
12			$(2C_8+C_9)/3$
13			$(C_4+C_8+C_{12})/3$
14			$(C_6+C_{12}+C_{15})/3$
15			$(C_8+2C_9)/3$

Table 5.3: Design rules to compute constellation points for M -ary CSK. Each row computes C_m , the chromaticity coordinate for m^{th} codeword for any given CBC_v . C_n^v is the chromaticity coordinate of color band $n \in \{i, j, k\}$ belonging to CBC_v .

‘band j’ and ‘band k’ respectively. 9 such CBC_v ; $1 \leq v \leq 9$ are defined in the standard and are outlined in Table 5.2. The generalized notation CB_n^v is used to indicate color band of type $n \in \{i, j, k\}$ belonging to CBC_v . Thus in Table 5.2, the cell representing row for CBC_v and column for band n provides index u for the color band represented by notation CB_n^v . Using this notation $\text{CB}_i^1 \equiv \text{CB}_6$ while $\text{CB}_j^2 \equiv \text{CB}_1$ and so on.

For an M -ary CSK using CBC_v , the design rules to compute the M different constellation points are provided in the standard and their values are outlined in (A. Yokoi and Bae, 2011). Let $C_n^v \equiv (x_n^v, y_n^v)$ be chromaticity coordinate corresponding to CB_n^v . Let $C_m \equiv (x_m, y_m)$; $0 \leq m < M$ be chromaticity coordinate corresponding to m^{th} codeword. Then Table 3 outlines the design rules for computing the constellation points. C_n^v can be looked up from Table 5.2 and Table 5.1. Using these values, remaining C_m can then be computed using rules from Table 5.3. Normalized constellation design rules for M -ary CSK are illustrated in Figure 5.2. Points I, J and K represent normalized coordinates for the n color bands comprising a CBC.

5.2 CSK system outline

CSK is implemented in conjunction with IM/DD over the optical channel. This channel can be modeled as a linear time invariant system with AWGN and mathematically represented as in Eq.(5.1)

$$\mathbf{Y} = \mathbf{H}\mathbf{X} + \mathbf{W} \quad (5.1)$$

where \mathbf{X} is an N_{tx} dimensional vector containing transmit optical powers for each band n , \mathbf{H} is a $N_{rx} \times N_{tx}$ dimensional channel matrix, \mathbf{W} is a N_{rx} dimensional noise vector and \mathbf{Y} is an N_{rx} dimensional receive vector. Channel matrix \mathbf{H} includes the responsivities of the receive elements.

In M -ary CSK, $N_{tx} = 3$ types of LEDs are used to generate M different SPDs

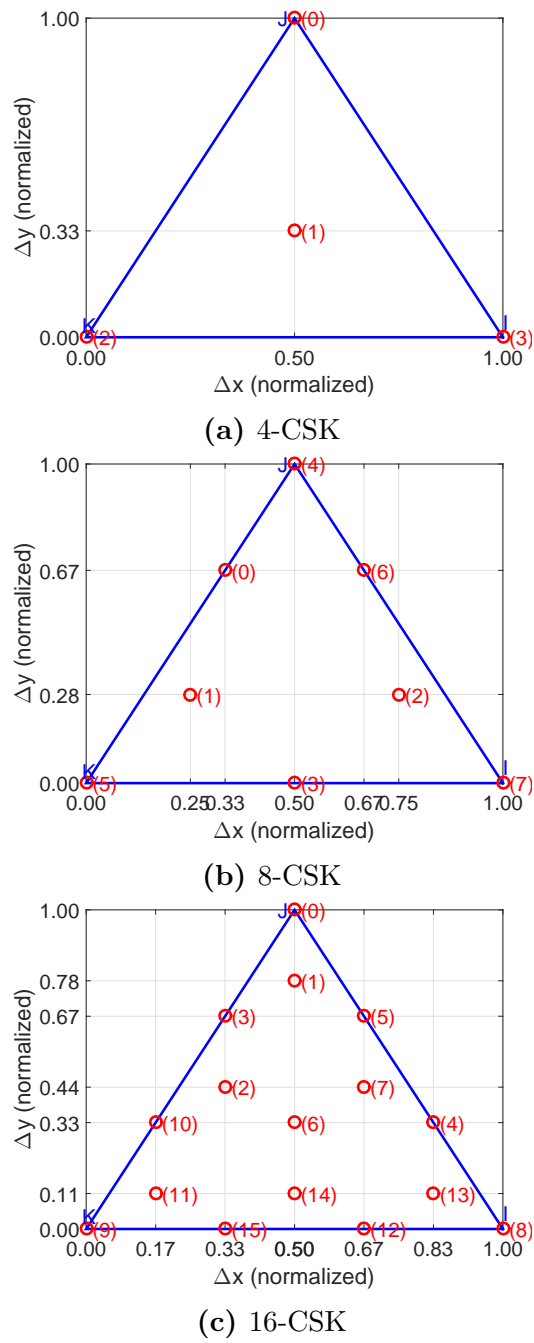


Figure 5.2: M -ary CSK (normalized) constellation design rules

corresponding to M different chromaticity coordinates. Each chromaticity coordinate represents a codeword that encodes $\log_2(M)$ bits. In order to transmit information, the luminaire irradiates an SPD corresponding to the desired transmit codeword. The clock rate at the luminaire is of the order of tens of MHz. This rate is much higher than which can be perceived by human eye as flicker. In addition, the CSK signaling chain can include a scrambler that ensures data and thus codewords are pseudo-randomly distributed thus mitigating color flicker.

At the receiving elements, each SPD produces a different electrical response signal. The signal output from each receiving element is corrupted by shot noise of variance σ_{sh}^2 due to ambient light as in Eq. (2.10) and thermal noise of variance σ_{th}^2 due to trans-impedance amplifier as shown in Eq. (2.12). The SNR can then be defined as in Eq.(5.2).

$$\text{SNR} \triangleq \frac{\text{Tr}\{\mathbf{H}\mathbf{X}\mathbf{X}^*\mathbf{H}^*\}}{\sigma_{\text{nt}}^2} \quad (5.2)$$

where $\text{Tr}\{\cdot\}$ is the matrix trace operator, $*$ indicates transpose and $\sigma_{\text{nt}}^2 = \sigma_{\text{sh}}^2 + \sigma_{\text{th}}^2$ is the total noise variance. SNR in decibel is then computed as $10\log_{10}(\text{SNR})$.

Having received vector \mathbf{Y} , least squares estimate of transmitted vector ($\hat{\mathbf{X}}$) can be made by Eq.(5.3).

$$\hat{\mathbf{X}} = (\mathbf{H}^*\mathbf{H})^{-1}\mathbf{H}^*\mathbf{Y} \quad (5.3)$$

After estimating vector $\hat{\mathbf{X}}$, an estimate of transmitted chromaticity coordinates can be made and transmitted information can then be decoded. The process of transforming chromaticity coordinates to optical power and vice-versa gives rise to two different system models as described in further sections.

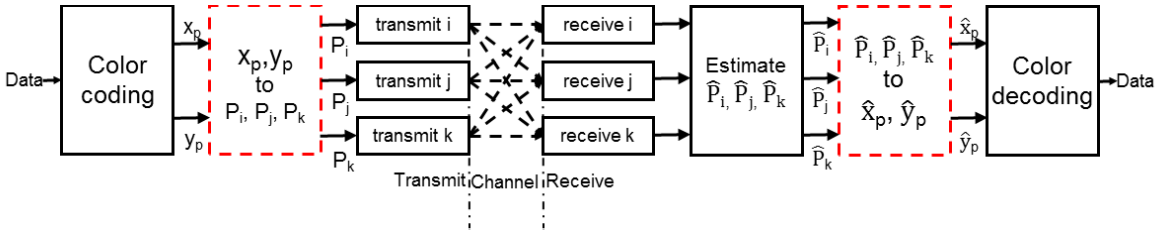


Figure 5·3: CSK signal chain block diagram

5.3 Linear system model

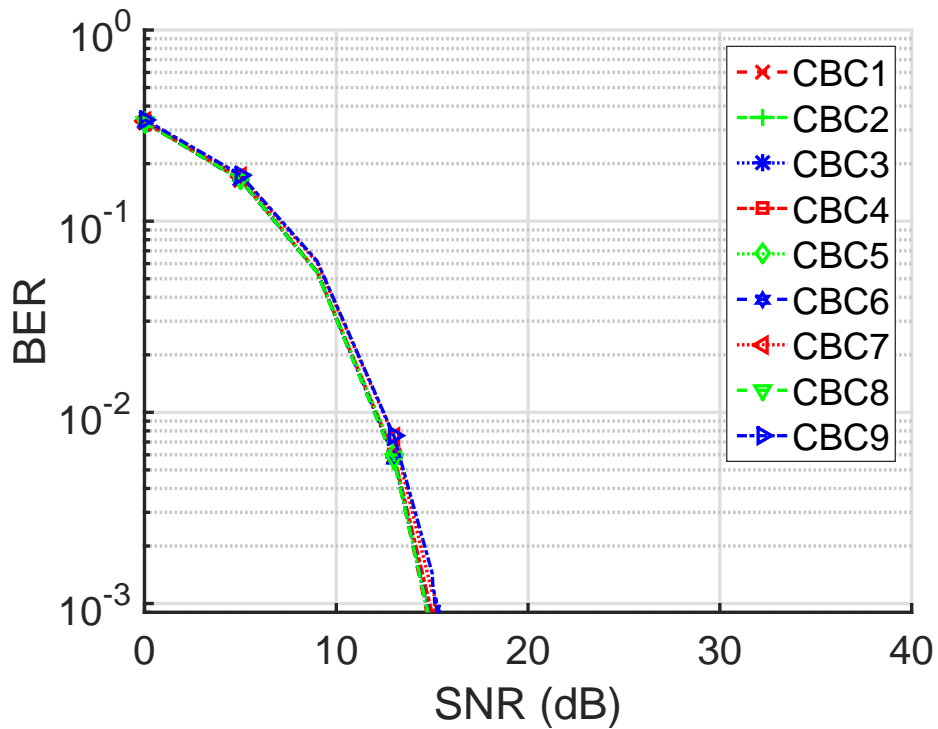
The linear CSK model treats the CIE-CS as a linear space to analyze CSK performance. This implies the inherent assumption that when irradiance from multiple transmitting elements is combined, the chromaticity coordinates of the resulting SPD is a linear combination of the chromaticity coordinates of the SPDs of individual transmitting elements. If $P_n; n \in \{i, j, k\}$ is the normalized radiant flux at the transmit or receive device associated with band n , Eq.(5.4) below taken from the standard provides the implied mathematical relationships between chromaticity coordinates of all bands and that of resultant SPD.

$$\begin{aligned} x_p &= P_i x_i + P_j x_j + P_k x_k \\ y_p &= P_i y_i + P_j y_j + P_k y_k \\ 1 &= P_i + P_j + P_k \end{aligned} \tag{5.4}$$

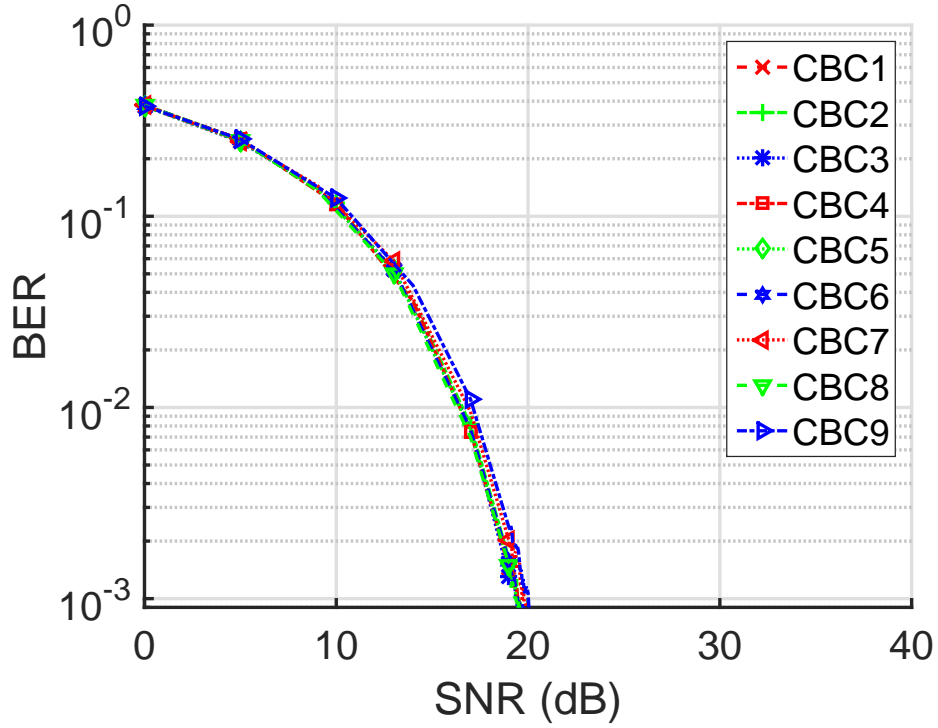
A block diagram of the CSK signaling chain is shown in Figure 5·3. At the transmitting element, the encoded information bit-stream is mapped to chromaticity coordinates (x_p, y_p) as computed from Table 5.3. Using Eq.(5.4), normalized P_n values are computed which are then scaled to achieve a user requested illumination target and thus transmit irradiance. A vector of scaled P_n values then forms the transmit vector \mathbf{X} . Without loss of generality, unity E/O conversion at transmitter and unity responsivity (O/E conversion) at the receiver is assumed. Receiving element

for band n senses the incident flux and generates an electrical signal proportional to it. AWGN is then added to each band n in the form of vector \mathbf{W} . The receiver output in presence of noise is represented by \mathbf{Y} . With the knowledge of the channel state and the receiver output, a least squares estimate of transmit vector $\hat{\mathbf{X}}$ is made using Eq.(5.3). Each element of $\hat{\mathbf{X}}$ then provides the estimates of transmitted flux represented by \hat{P}_n . Using these values, (\hat{x}_p, \hat{y}_p) are estimated using Eq.(5.4). NN decoder then estimates the transmitted coordinate and recovers the transmitted information. Thus for the linear system model, Eq.(5.4) represents the $(x_p, y_p) \rightarrow P_n$ and $P_n \rightarrow (\hat{x}_p, \hat{y}_p)$ transformations for the red dashed blocks of Figure 5·3.

Monte-carlo simulations are performed to compute performance of M -ary CSK under the linear model for all CBC_v and Figure 5·4 shows the results. Performance of all CBCs is similar except CBC_7 and CBC_9 which perform slightly worse, but only by a margin of about 0.6 dB. This performance is as expected. As seen from Table 5.2, CBC_7 is composed of CB_3 , CB_2 and CB_0 whereas CBC_9 is composed of CB_2 , CB_1 and CB_0 . Thus from values in Table 5.1 and Figure 5·1, it can be seen that constellation points for other CBCs are the most spread out and have the large minimum distance between constellation points where as that for CBC_7 and CBC_9 have the shorter spread and have the smaller minimum distance between constellation points. SNR of at least 15 dB, 20 dB and 25 dB are needed to achieve a target minimum BER of 10^{-3} under the linear model for $M = 4, 8$ and 16 CSK respectively.



(a) 4-CSK



(b) 8-CSK

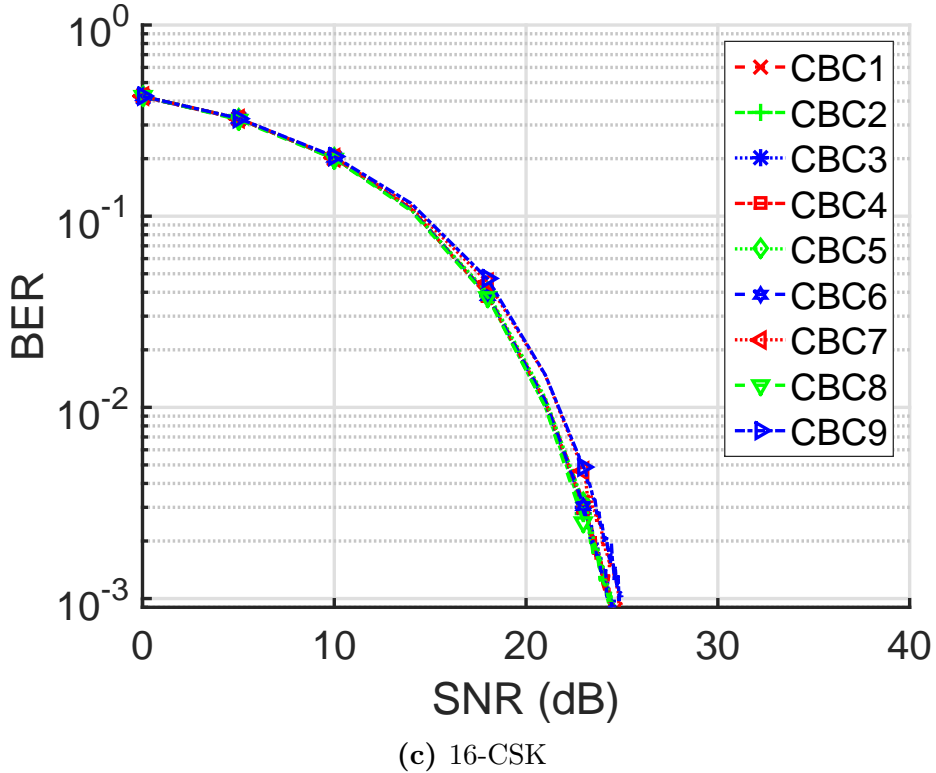


Figure 5.4: CSK linear model BER vs SNR performance for all CBCs

Figure 5.5 shows received symbols for CBC_2 , whose constellation points are the most spread out, under the linear model. As expected, noise is spread normally along x and y dimensions forming a circular envelop around all constellation points. For $M = 8$ and $M = 16$, empty non-interfering regions devoid of received symbols can be seen in the figures. This indicates that these constellations could be better packed by defining additional points in the non-interfering regions. The constellations can then be further optimized to achieve better spectral efficiency. Note that in Figure 5.5 (a), (b) and (c), some of the received symbols are located outside the color gamut (triangle IJK as outlined in Figure 5.2) formed by the sources for i, j and k bands. This would appear to violate the relationships on the CIE-CS model between coordinates of SPDs of individual sources and that of the resultant SPD formed by mixing the fluxes in different ratios. However, at the receiver, the received signals are influenced by noise

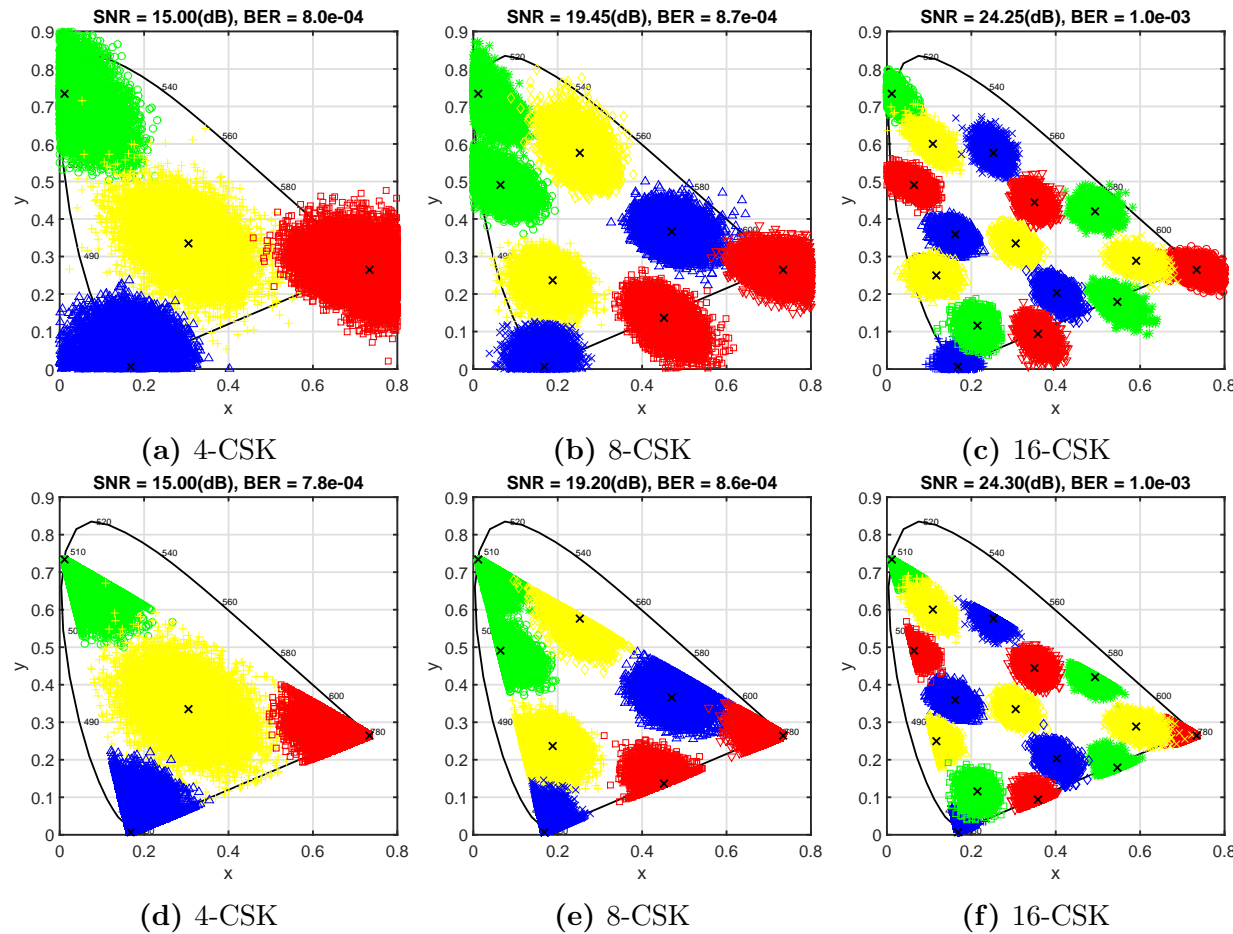


Figure 5.5: Received symbols for CBC₂ (a),(b),(c): Receiver output not clipped (d),(e),(f): Negative values of receiver output clipped at zero

(bipolar, zero-mean Gaussian) resulting in bipolar received values. Received signals with negative values when mapped back to the CIE-CS, can cause received ‘noisy’ symbols to lie outside of the gamut.

Since the transmitted radiant fluxes are always non-negative, it is possible to clip the receiver output prior to estimating the transmitted radiant flux. When negative receiver output is clipped at zero, estimated symbols are illustrated in Figure 5·5 (d), (e) and (f). This clipping shows that the mapping back to CIE-CS is sensical. It can also be seen that at target BER of 10^{-3} , the clipping does not introduce any significant change in performance when compared to that without clipping.

While this linear system model is instructive to study M -ary CSK modulation and carry out a first order performance analysis, a practical CSK system incorporating human eye’s visual perception, is non-linear due to non-linearity of the CIE-CS. The $(x_p, y_p) \rightarrow P_n$ block at the transmitter and its counterpart and $\hat{P}_n \rightarrow (\hat{x}_p, \hat{y}_p)$ at the receiver (red colored dashed blocks in Figure 5·3) introduce this non-linearity which significantly alters the M -ary CSK performance for a practical implementation. The effects of these practical constraints on a CSK system are studied in next few subsections.

5.4 Non-linear system model

To understand the source of non-linearity in the CSK system, let’s take a look at the CIE-CS which empirically models the human eye’s visual perception of color for a stimulating SPD. Let $S_n(\lambda)$ be the SPDs of the transmit LEDs and P_n be the radiant flux associated with band n . Thus the aggregate transmitted SPD is given by Eq.(5.5).

$$W(\lambda) = \sum_{n \in \{i, j, k\}} P_n S_n(\lambda) \quad (5.5)$$

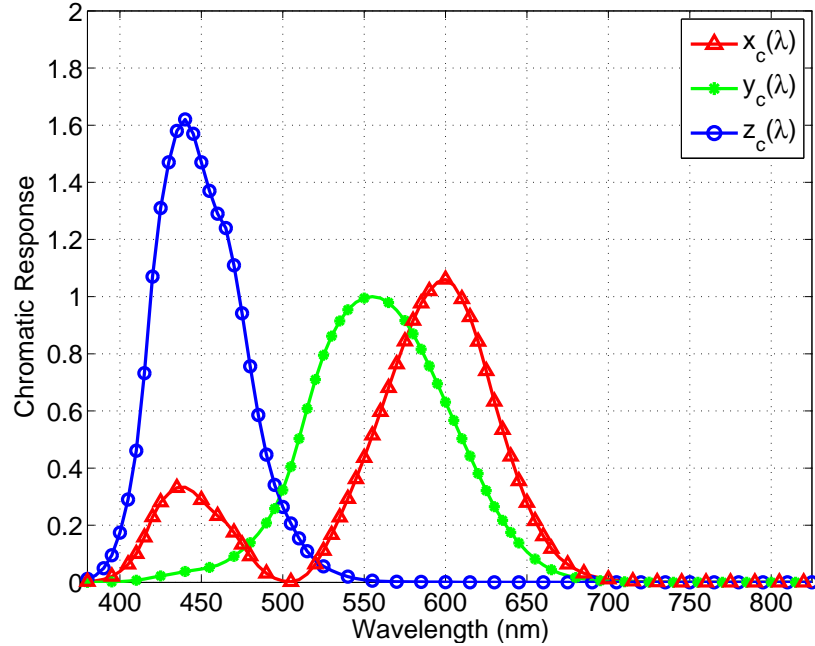


Figure 5.6: CIE 1931 XYZ color matching functions

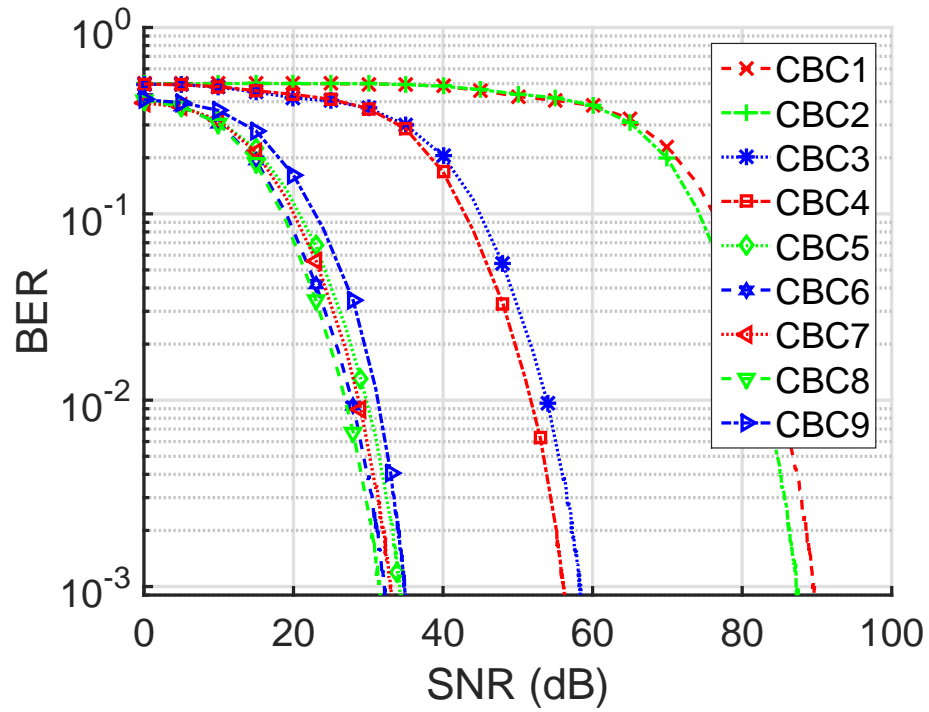
CIE-CS specification outlines three color matching functions - $x_c(\lambda)$, $y_c(\lambda)$ and $z_c(\lambda)$ as illustrated in Figure 5.6. The tristimulus values for the three primary sources as defined in the CIE-CS are given by Eq.(5.6) and the chromaticity coordinates (x_p , y_p) of the resultant SPD $W(\lambda)$ are given by Eq.(5.7). From Eqs.(5.5-5.7) it can also be inferred that the relationship between P_n and (x_p, y_p) is non-linear.

$$\begin{aligned}
 X_W &= \int_{\lambda = 380 \text{ nm}}^{\lambda = 780 \text{ nm}} W(\lambda) x_c(\lambda) d\lambda \\
 Y_W &= \int_{\lambda = 380 \text{ nm}}^{\lambda = 780 \text{ nm}} W(\lambda) y_c(\lambda) d\lambda \\
 Z_W &= \int_{\lambda = 380 \text{ nm}}^{\lambda = 780 \text{ nm}} W(\lambda) z_c(\lambda) d\lambda
 \end{aligned} \tag{5.6}$$

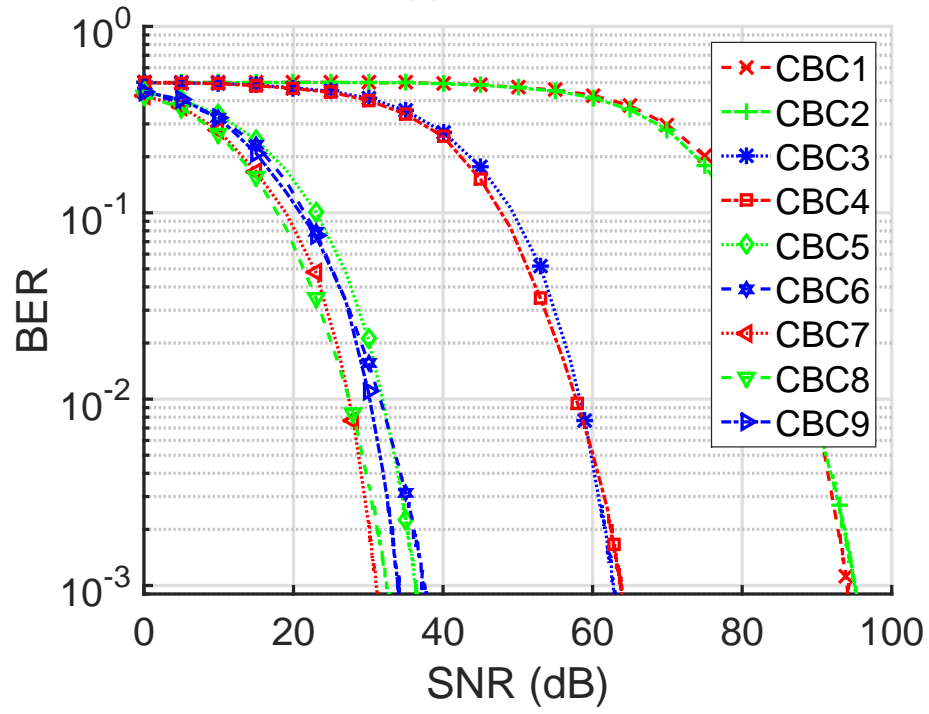
$$x_p = \frac{X_W}{X_W + Y_W + Z_W}; \quad y_p = \frac{Y_W}{X_W + Y_W + Z_W} \tag{5.7}$$

As outlined in prior sections, M -ary CSK modulation transmits information by varying the chromaticity coordinates of transmit SPD. In a practical implementation, a table of unique transformation ratios $P_i:P_j:P_k \rightarrow (x_p, y_p)$ can be pre-computed for each of the M constellation points. Referring back to Figure 5.3, at the transmitter the data is color coded to obtain (x_p, y_p) coordinate to transmit. Given this coordinate, corresponding flux ratios $P_i:P_j:P_k$ can be looked up from the pre-computed table. The target illumination requirements provide the total radiant flux to output from the transmitting sources. With the flux ratio and the total radiant flux information, individual P_n for each band n can now be computed from Eq.(5.5). This transformation now forms the $(x_p, y_p) \rightarrow P_n$ block in the transmitter signaling chain. These transmitted flux are sensed by the receivers in presence of AWGN. The receivers generate an electrical output which is then used to compute an estimate of transmitted radiant fluxes \hat{P}_n . Eqs.(5.5-5.7), which now constitute the $\hat{P}_n \rightarrow (\hat{x}_p, \hat{y}_p)$ block in the receive signal chain, can then be used to estimate the transmitted coordinate (\hat{x}_p, \hat{y}_p) . Thus, the AWGN added to the received signal undergoes a non-linear transformation during $\hat{P}_n \rightarrow (\hat{x}_p, \hat{y}_p)$ process which skews the noise in the chromaticity plane of the CIE-CS. This causes additional performance penalties in a practical CSK system.

Figure 5.7 shows performance of all the CBCs under this non-linear model. These curves are obtained by monte-carlo simulations similar to those performed for the linear model after substituting the $P_n \rightarrow (x_p, y_p)$ and $\hat{P}_n \rightarrow (\hat{x}_p, \hat{y}_p)$ blocks with the non-linear system model transformations. It can be observed that CBC₇ and CBC₈ perform relatively similar and are the best while CBC₁ performs the worst. Additionally, it is observed that CBC₁-CBC₄ perform significantly worse as compared to the rest. For CBC₁-CBC₄, the amount of radiant flux emitted by band i is 3-4 orders of magnitude greater than band j and 1-2 orders of magnitude greater than



(a) 4-CSK



(b) 8-CSK

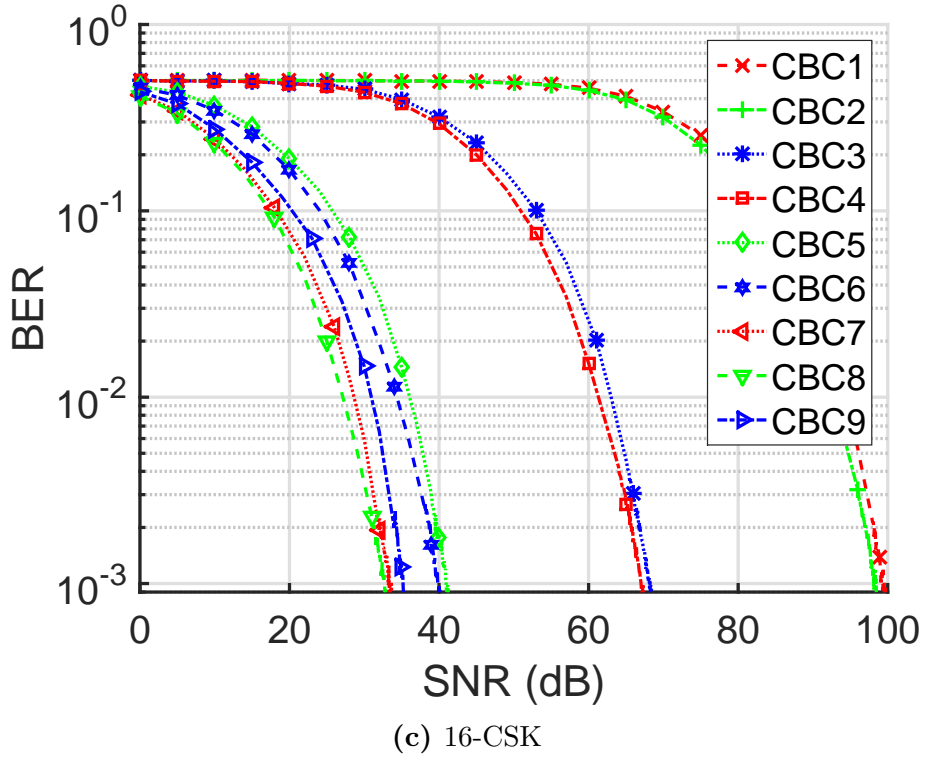


Figure 5.7: CSK non-linear model BER vs SNR performance for all CBCs

band k. Thus the $\hat{P}_n \rightarrow (\hat{x}_p, \hat{y}_p)$ conversion at the receiver is extremely sensitive to noise along the j and k bands as compared to that along the i band. This introduces significant errors in decoding received symbols.

Figure 5.8 and Figure 5.9 show received symbols for CBC_1 and CBC_8 under the non-linear model. Noise skew about the estimated coordinates can be observed in both figures. This noise skew is more prominent for CBC_1 where the signal power distribution along all bands is imbalanced. In contrast for CBC_8 , signal power is more uniformly spread across all bands. For Figure 5.8, the negative receiver output is not clipped at zero. As mentioned earlier, in presence of noise (zero mean and Gaussian), some receiver output values can be negative and thus such received symbols are located outside the color gamut when transformed to CIE-CS space. The effect of clipping negative receiver output at zero can be seen in Figure 5.9 where all received

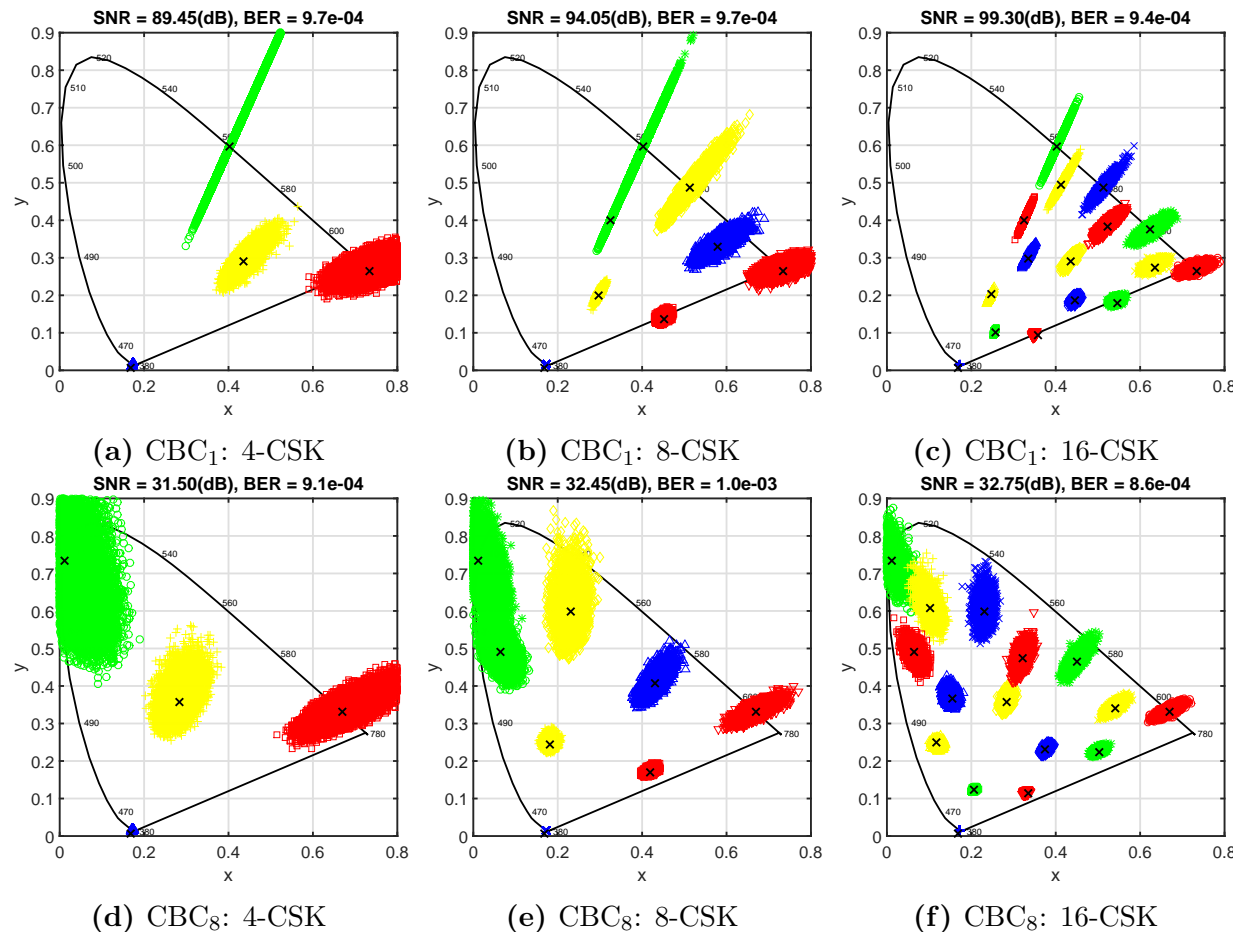


Figure 5·8: Received symbols for non-linear model when receiver output is not clipped

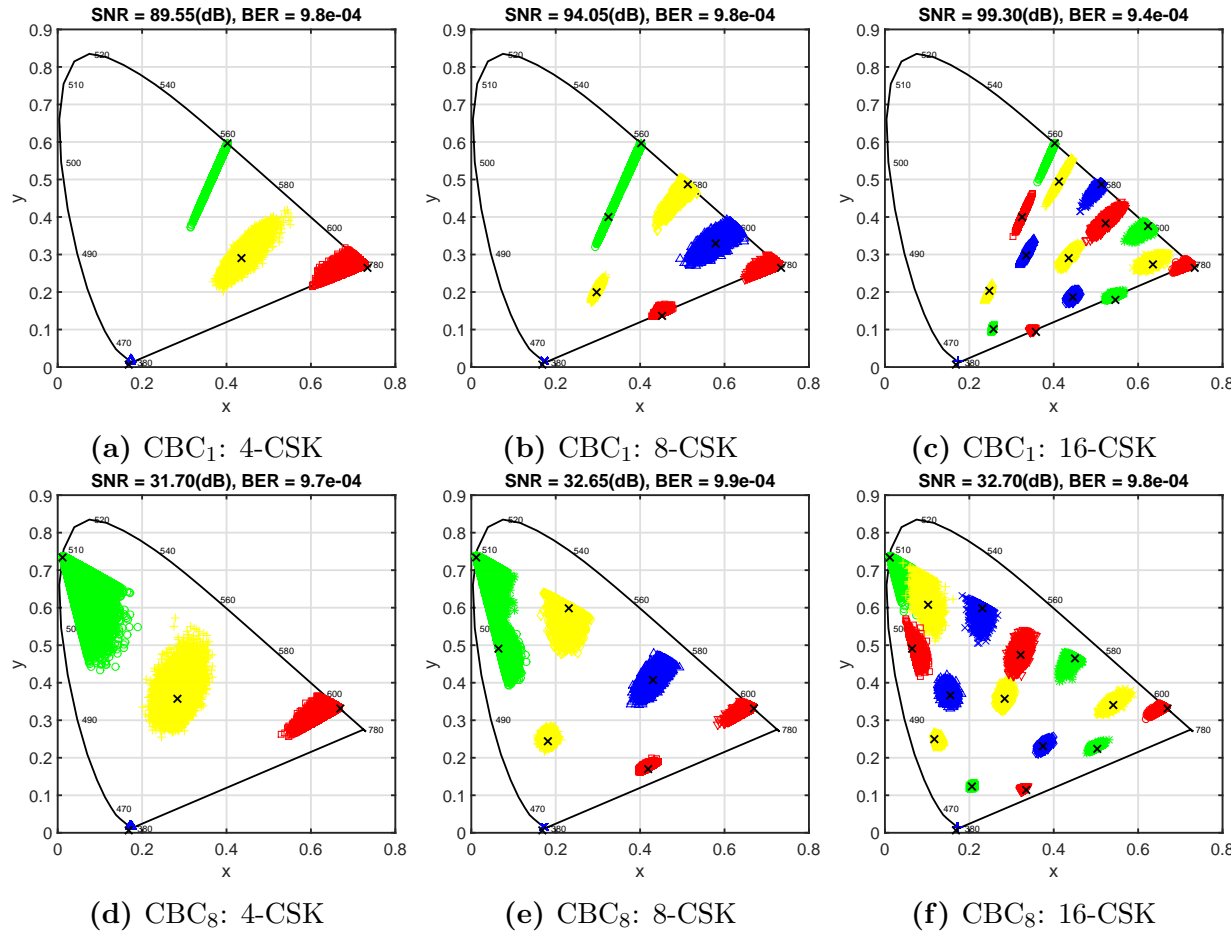


Figure 5.9: Received symbols for non-linear model when negative values of receiver output are clipped at zero

symbols now are located inside the color gamut. It can be seen that performance of both receiver signal processing techniques is similar, as such no one outperforms the other. It can be seen that AWGN introduced on \hat{P}_n gets skewed radially towards band k due to non-linearity in $\hat{P}_n \rightarrow (\hat{x}_p, \hat{y}_p)$ transformation and is no longer AWGN along the CIE-CS chromaticity plane. This generates an interesting outcome in that for CBC₈, about 30 dB of SNR is needed to achieve target 10^{-3} BER for all of $M = 4, 8$ and 16 CSK. This happens because with increase in order M , the additional constellation points as defined in the standard happen to occupy non-interfering regions of the chromaticity plane thus increasing spectral efficiency without incurring any SNR penalty up to a point. The non-linearity of the CIE-CS introduces performance penalties of at least 15 dB, 10 dB and 5 dB for $M = 4, 8$ and 16 CSK respectively over the linear system model.

5.5 CSK system performance under illumination constraints

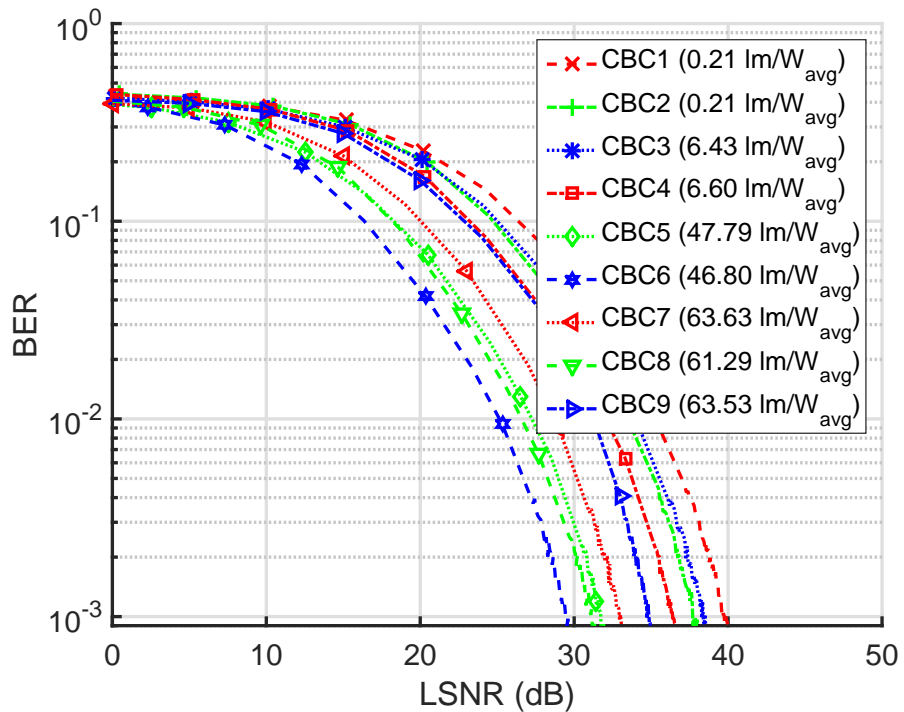
In an indoor optical wireless system using lighting devices for wireless downlink access the luminaires need to simultaneously service illumination and optical wireless broadcast missions. Under this model, different colored PHY (example: different CBC_v) irradiate different amounts of radiant flux to achieve the same illumination intensity level. Thus, it is unfair to use SNR as a metric to compare performance of modulation schemes at same BER target using different colored PHY without first normalizing for illumination targets. Thus, in this section we introduce LSNR as a metric that takes into account the differences in radiant flux emitted by different PHY to achieve the same illumination intensity level. It should be noted that the LSNR metric is not specific to CSK, but instead can be used more generally to compare performance of any two optical modulation schemes that are operated at the same optical intensity levels.

Consider optical modulation scheme(s) which can be implemented with two different constellations C_a or C_b . The fluxes emitted by the two constellations are scaled to achieve a target illumination intensity level. Let both constellations on average emit I lumens of luminous flux. Let the luminous efficacy for the two constellations be specified by η_a and η_b in lumens-per-watt respectively. Then the corresponding average radiant flux emitted by the two constellations is given by $W_a = I/\eta_a$ and $W_b = I/\eta_b$ watts respectively. Let us define a luminous ratio $L_{ab} \triangleq (\eta_a/\eta_b) \equiv (W_b/W_a)$. Thus, for every 1 Watt of radiant flux emitted by C_a , C_b must emit L_{ab} Watt of radiant flux to achieve the same illumination intensity level. Under the model where the luminaires service illumination along with communication, it is fair to compare the performance of the two schemes at these relative radiant flux levels instead of at the absolute radiant flux levels. Thus we define the LSNR metric in Eq.(5.8) as a means to compare performance of C_b versus that of C_a at same illumination levels.

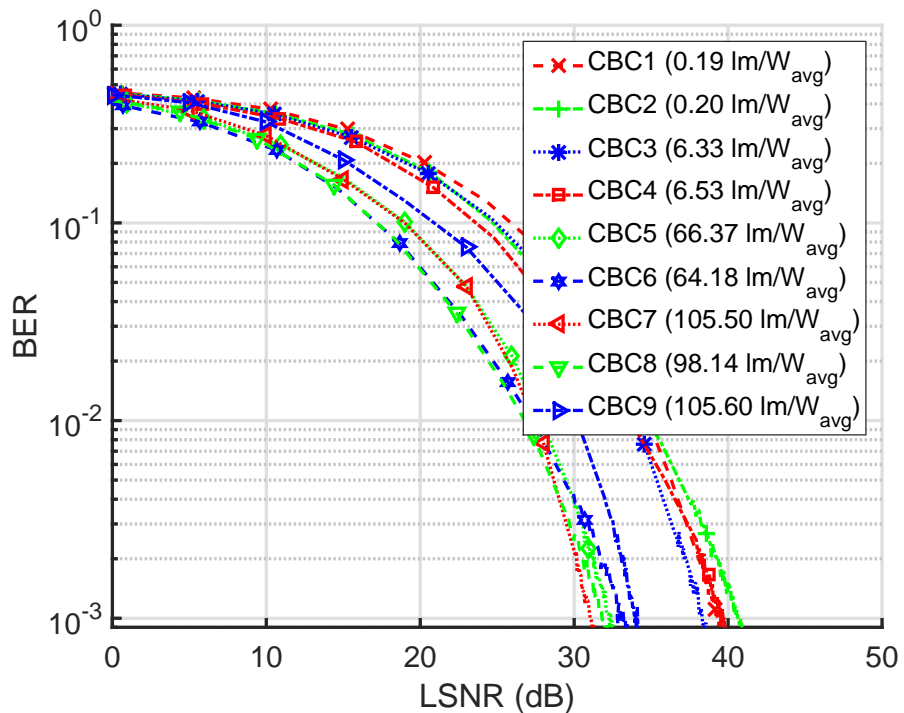
$$\text{LSNR}_{ab} \triangleq \frac{L_{ab}^2 \text{Tr}\{\mathbf{H}\mathbf{X}_b\mathbf{X}_b^*\mathbf{H}^*\}}{\sigma_n^2} \quad (5.8)$$

where \mathbf{X}_b is the average radiant flux emitted by C_b . Thus, after computing BER vs SNR for the scheme employing C_a , BER vs LSNR can be computed for scheme employing C_b to compare its performance relative to that employing C_a at the same illumination levels.

Figure 5.10 shows performance of the 9 CBCs under the non-linear model when normalized for illumination constraints. The efficacies of all CBC for different M are specified in the legends. These values are used to normalize the performance of M -ary CSK for all CBC using CBC with highest efficacy as the reference for LSNR calculation. CBC_7 , CBC_9 and CBC_9 are used as reference CBCs for $M = 4, 8$ and 16 CSK respectively. The effect of this is to shift all curves (except the reference) from Figure 5.7 towards left along the LSNR-axis depending on the L_{ab} values in Eq.(5.8).



(a) 4-CSK



(b) 8-CSK

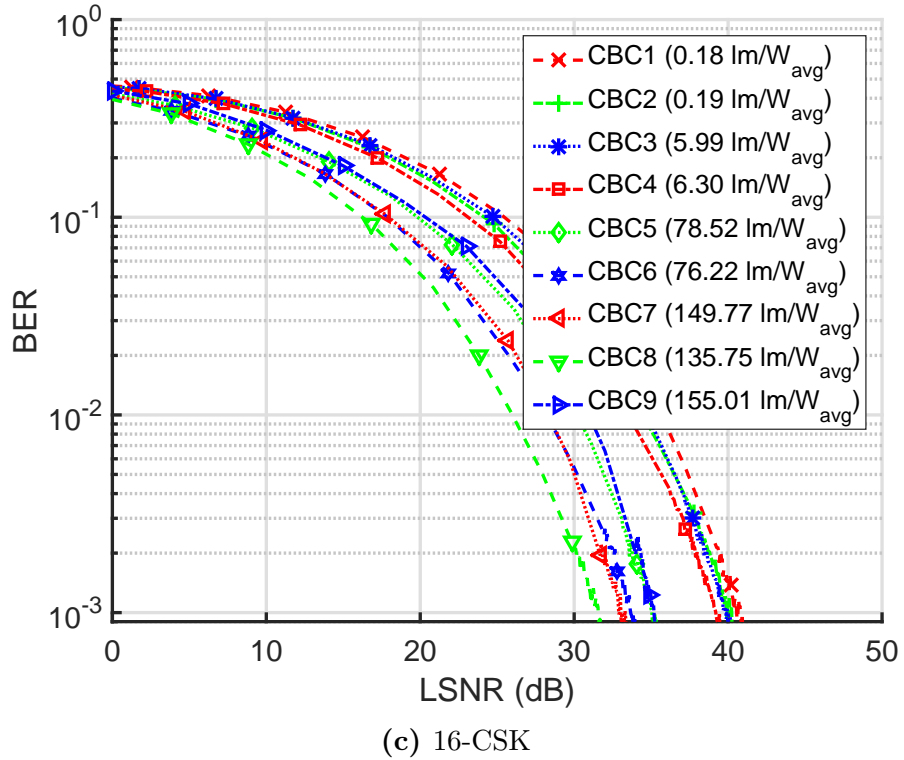


Figure 5.10: CSK BER vs LSNR performance for all CBCs

It can be observed that given a target illumination intensity level and for target 10^{-3} BER, CBC₆ performs the best for 4-CSK, CBC₇ and CBC₈ perform similar and better than others for 8-CSK and CBC₈ performs the best for 16-CSK. For CBC₁-CBC₄, due to their low luminous efficacy, one can use a much larger radiant flux to achieve target illumination levels and thus significantly improve their communication performance. However, this is achieved at the cost of poor energy efficiency. In contrast, CBC₇ and CBC₉ have relatively high luminous efficacy. This implies that these CBCs are restricted to emit a relatively lower radiant flux (and thus low signal powers) to achieve target illumination level thus affecting their communication performance.

In conclusion, this chapter studies the performance of all CBCs as specified for M -ary CSK in the IEEE 802.15.7 standard. Under the linear system model, all CBCs perform relatively well and need SNR of at least 15 dB, 20 dB and 25 dB to achieve

target BER of 10^{-3} for $M = 4, 8$ and 16 CSK respectively. The non-linear system model is then considered due to the unique non-linear visual perception characteristics of human eye. It is shown that the non-linearity of the CIE-CS causes the AWGN introduced to the received signal to get skewed and no longer remain AWGN when transformed to the chromaticity plane. Under the non-linear system model, CBC_7 and CBC_8 perform relatively similar and are better than all other CBCs. A performance penalty of at least 15 dB, 10 dB and 5 dB incurred for the practical non-linear model as compared to linear model for $M = 4, 8$ and 16 CSK respectively. A new LSNR metric is proposed to compare performance of any two schemes (and not just CSK) using the visible spectrum for wireless communication and lighting after normalizing signal powers to achieve a target illumination intensity level. Performance comparisons of M -ary CSK for all CBCs then reveal that CBC_6 performs the best for 4-CSK , CBC_7 and CBC_8 perform similar and better than others for 8-CSK and CBC_8 performs the best for 16-CSK .

For IM/DD signaling scheme, the receiver output is always expected to be non-negative in absence of noise. For some O-OFDM systems, clipping negative receiver output has been shown to improve performance by eliminating some noise. On the contrary, for M -ary CSK, the performance in presence or absence of clipping the negative receiver output does not seem to differ significantly. This does not imply that noise in the negative receiver output is orthogonal to signal itself. The negative receiver output pushes the received symbol outside the color gamut on the CIE-CS. In the presence of relatively high SNR, the received symbol is still located closer to the expected constellation point thus does not introduce any additional errors.

Optimal performance of CSK can be seen as a tradeoff between the illumination and communication missions. There is further scope to optimize the M -ary CSK constellations under the practical non-linear model by selecting optical sources centered

at different wavelengths than those considered in the standard. After characterizing skew for AWGN along the chromaticity plane, constellation points can be optimally positioned and optimal receiver architectures can be introduced to further improve the M -ary CSK performance.

Chapter 6

Metameric modulation

In this chapter, we propose metameric modulation¹ - a novel modulation scheme for VLC which can maintain constant perceived ambient lighting. By using $D > 3$ LEDs, it is possible to render same illumination chromaticity with different combinations of LEDs. These different illumination SPDs are indistinguishable to humans but are distinguishable to an electronic receiver and can be achieved due to principle of metamerism. Information is encoded in changes between these states and can be recovered by detecting intensity modulation in different wavelength bands.

6.1 Metamerism

The human eye is a sensory organ that enables humans to perceive electromagnetic radiation in a subset of the optical spectrum. Figure 6·1 (Jain, 1989) shows the typical photopic relative luminous efficiency function of our visual system under moderate to higher levels of illumination. The retina in the eye contains sensory receptors called rods and cones. A normal human eye has three kinds of cones - short (S), medium (M) and long (L) based on the relative wavelengths that induce the peak response. Photons at different wavelengths are absorbed differently by the rods and the three sets of cones. Figure 6·2 (Wandell, 1996) shows the normalized absorbance of photons by rods and cones over a range of wavelengths. The peak responses of the cones are 420 nm, 534 nm and 564 nm while that of the rods is 498 nm. Cones are responsible

¹This work is published in peer-reviewed IEEE proceeding (Butala et al., 2012).

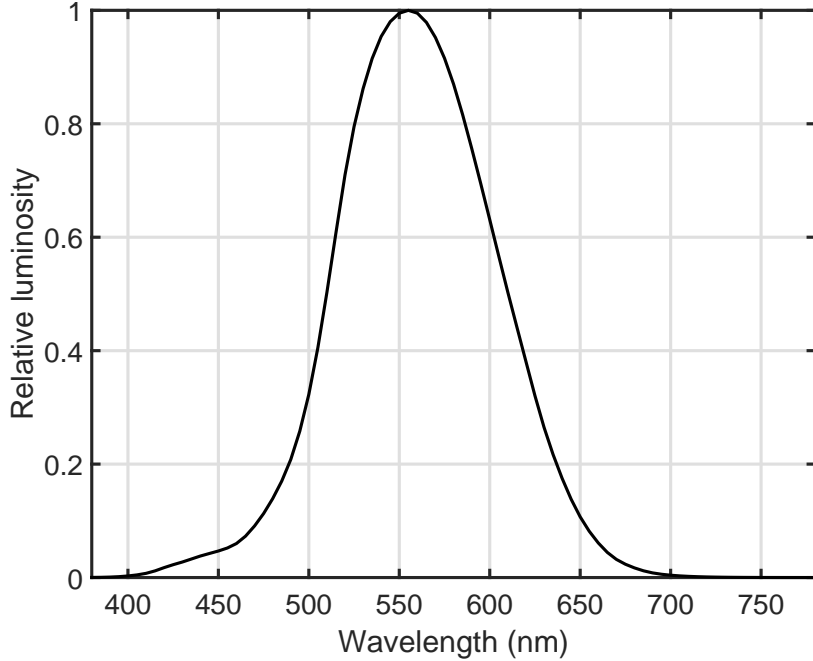


Figure 6·1: Typical photopic relative luminous efficiency function

for color vision. Let $S_i(\lambda); i \in \{S, M, L\}$ denote their spectral responses to stimulus over a range of wavelengths. Optical stimulus with an SPD $C(\lambda)$ will induce optical sensation α_i within the cones as described in Eq. (6.1).

$$\alpha_i = \int_0^{\infty} C(\lambda) S_i(\lambda) d\lambda \quad (6.1)$$

Grassmann's laws (Grassmann, 1854) of color matching develop the theory behind the psychovisual color space spanned by cones in the human eye, henceforth called the visual color space (VCS). This space is a subspace of the infinite dimensional universal color space (UCS), which contains all possible SPDs. This observation leads to another interpretation of Eq. (6.1) - the point $[\alpha_S, \alpha_M, \alpha_L]$ is a projection of a given SPD $C(\lambda)$ onto the VCS. Thus it is possible for multiple different SPDs to project onto the same point within the VCS and produce the same sensations, $[\alpha_S, \alpha_M, \alpha_L]$, in the human eye. These SPDs are sensed as the same color by the human

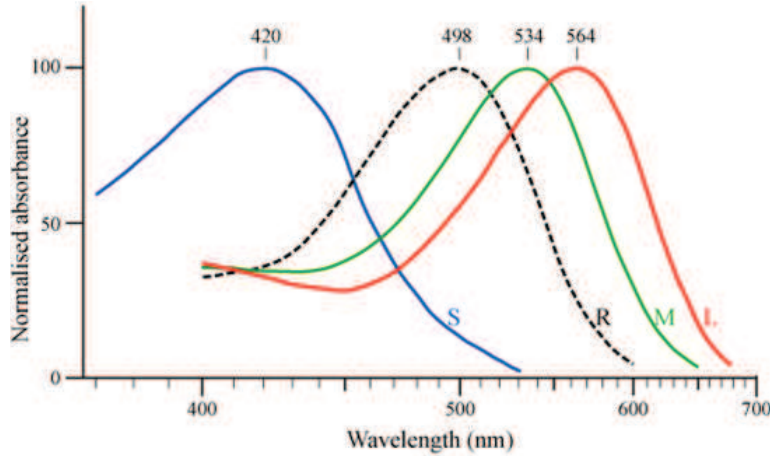


Figure 6.2: Normalized absorbance of photons by rods and cones (Wandell, 1996)

eye and are called metamerically equivalent. Light from three independent primary light sources can be mixed in varying amounts to generate arbitrary colors. Let's call this resulting color space the primary color space (PCS). The projection of the PCS onto the VCS is called the color gamut of the primaries.

Section ?? provides a mathematical model that incorporates visual perception and maps SPDs to a point on the chromaticity plane. Since metamerically equivalent SPDs generate the same sensation from human eye, they are mapped to the same chromaticity point on the CIE-CS. The color gamut on the CIE-CS is a polygon with chromaticity coordinate of the primary light sources as its vertices.

6.2 MM system outline

Metameric modulation (MM) is implemented by using multiple sets of primary light sources capable of providing user requested illumination color. If we have D sources and each primary set is rendered with K primary elements, there are $\binom{D}{K}$ possible primary sets. As the number of primary sets increases, the intersection of their color gamuts quickly approaches an empty set. However only M of the possible primary

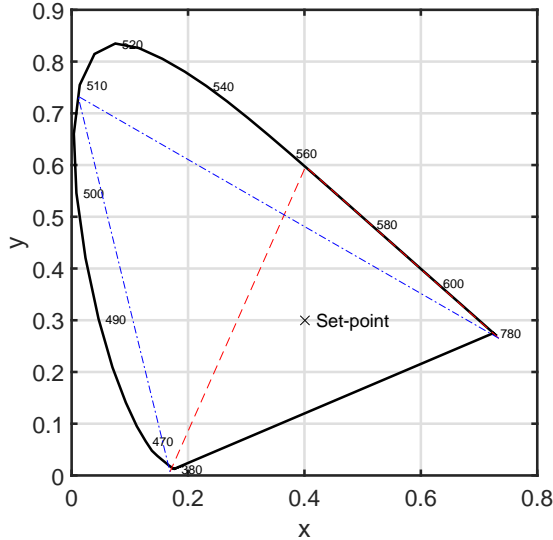


Figure 6.3: Example gamuts for MM with $D = 4$, $K = 3$ and $M = 2$

sets are selected so that the intersection of their color gamuts contain all of the desired lighting states. Figure 6.3 shows an example for $D = 4$, $K = 3$ and $M = 2$. The two sets of primaries, [Blue, Cyan, Red] and [Blue, Green, Red] have a significant overlap in their color gamuts. In this case they are capable of generating a set point with two different metameristic SPDs.

MM requires detection and discrimination of multiple wavelengths at the receiver. The necessary photodiodes must be designed such that when different primaries are activated to generate a desired ambient color, the receiver can detect which primary set is active while the lighting state appears the same to the human eye. The following derivation details how this can be achieved.

Consider $K = 3$ independent light sources that form one set of primaries. Let each $L_k(\lambda)$ be the normalized emission spectra of the k^{th} source such that Eq. (6.2) holds.

$$\int_0^{\infty} L_k(\lambda) d\lambda = 1 \quad (6.2)$$

Let α_i^k (6.3) be the spectral response induced by the k^{th} primary on the i^{th} class

of cones.

$$\alpha_i^k = \int_0^\infty L_k(\lambda) S_i(\lambda) d\lambda \quad (6.3)$$

Let $C(\lambda)$ be the SPD of the ambient color that we wish to maintain. Let each β_k be the amount of the corresponding $L_k(\lambda)$ needed to metamerically match $C(\lambda)$. Let α'_i (6.4) be the aggregate response evoked by the primaries on the i^{th} class of cones. Grassmann's laws of color matching uphold the linearity property of color addition over a wide range of luminances. Our typical ambient illuminance levels lie well within this range of luminances.

$$\alpha'_i = \sum_{k=1}^K \beta_k \alpha_i^k \quad (6.4)$$

The primaries must collectively evoke the same spectral responses in the human eye to match the color that is sensed due to $C(\lambda)$. Equating α_i in (6.1) with α'_i in (6.4) $\forall i$ leads to the color matching equation (6.5). Solving for β_k gives the relative amount of each primary that is needed to achieve a metamerical match with $C(\lambda)$.

$$\sum_{k=1}^K \beta_k \int_0^\infty L_k(\lambda) S_i(\lambda) d\lambda = \int_0^\infty C(\lambda) S_i(\lambda) d\lambda \quad (6.5)$$

Let $W(\lambda)$ be the SPD of the reference white against which the LEDs are calibrated. Let w_k be the amount of $L_k(\lambda)$ needed to metamerically match $W(\lambda)$. Each tristimulus value, t_k , of each primary is defined in (6.6). Varying t_k for each primary changes the relative amount of the light output from each source that is mixed and thus changes color.

$$t_k = \beta_k / w_k \quad (6.6)$$

Let the individual emission spectra of the k^{th} source from the m^{th} set of primaries be $L_k^m(\lambda)$. Now, let us assume we have P receivers selected as mentioned above. Let

Primary Set Index	Symbol
1	00
2	01
3	10
4	11

Table 6.1: MM symbol mapping

the effective receiver spectral responses be $S'_p(\lambda)$. This includes filter transmittance, concentrator gain and responsivity of the sensor and can be computed similar to Eq. (2.8) for a normalized white spectrum. When light from all sources of the m^{th} set of primaries is incident on the p^{th} photodiode, its current output, I_p^m , is given by (6.7).

$$I_p^m = \sum_{k=1}^K \beta_k \int_0^\infty L_k^m(\lambda) S'_p(\lambda) d\lambda \quad (6.7)$$

For a given color, the response matrix R_g is given by (6.8). It is possible to design a system where every column of matrix R_g would be distinct. One way of achieving this is by using optical filters with their peak transmittance aligned with peak primary source emissions. Optimal estimation of active primary set can be made by comparing output of the photodiodes with the columns of R_g .

$$R_g = \begin{pmatrix} I_1^1 & \dots & I_1^M \\ \vdots & \ddots & \vdots \\ I_P^1 & \dots & I_P^M \end{pmatrix} \quad (6.8)$$

The desired ambient lighting state can be specified by a point on the chromaticity plane of the standard CIE-CS. Table 6.1 shows example symbol map for $M = 4$. CIE-CS color space transforms can then be applied to specify the desired color within the M individual primary sets. Let t_k^m be the tristimulus value of the k^{th} primary of the m^{th} primary set. These primary sets can now generate distinct but metamerically equivalent SPDs. Switching between the different primary sets transmits symbols.

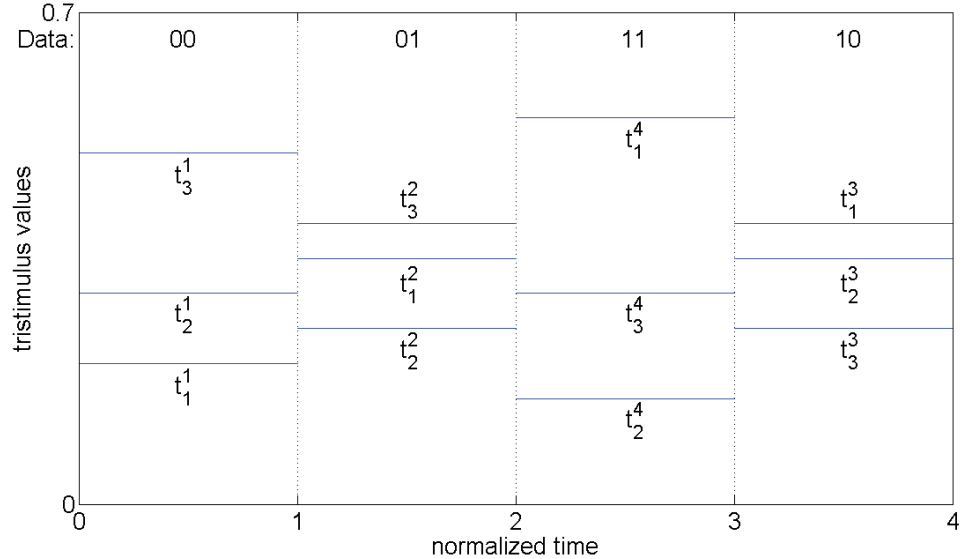


Figure 6·4: MM example timing diagram. Illustrates different metamerically equivalent SPDs being transmitted in different time slots.

Figure 6·4 illustrates MM using these primary sets to transmit a part of an encoded information stream (00011110_2). This is accomplished by switching primaries in the order 1-2-4-3. This order can then be detected by analyzing the received signal vector and data can be decoded. The embedded MM modulation is invisible to humans due to metamerism.

6.3 MM system performance

Performance of MM is studied using color bands and color band combinations as defined in the standard and outlined in section 5.1. Each set of LEDs generating a metameric color point can be implemented as a CBC. Block diagram for MM using CBCs is illustrated in Figure 6·5. For an M -ary MM, $\log_2(M)$ bits from the encoded bit-stream are mapped to one out of M possible CBCs. With knowledge of color set-point to generate and user requested illumination level, radiant fluxes $P_d; 1 \leq d \leq D$ to transmit are calculated. The LED drivers then drive all LEDs

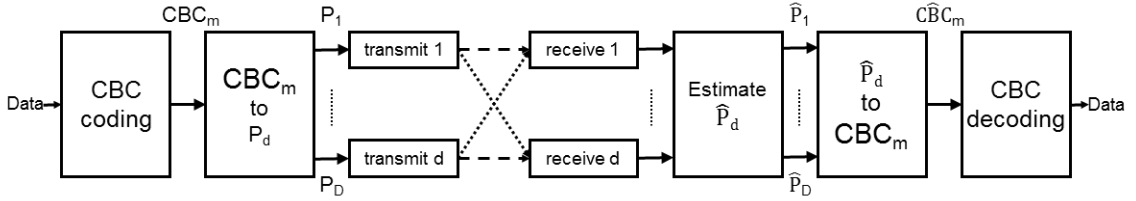
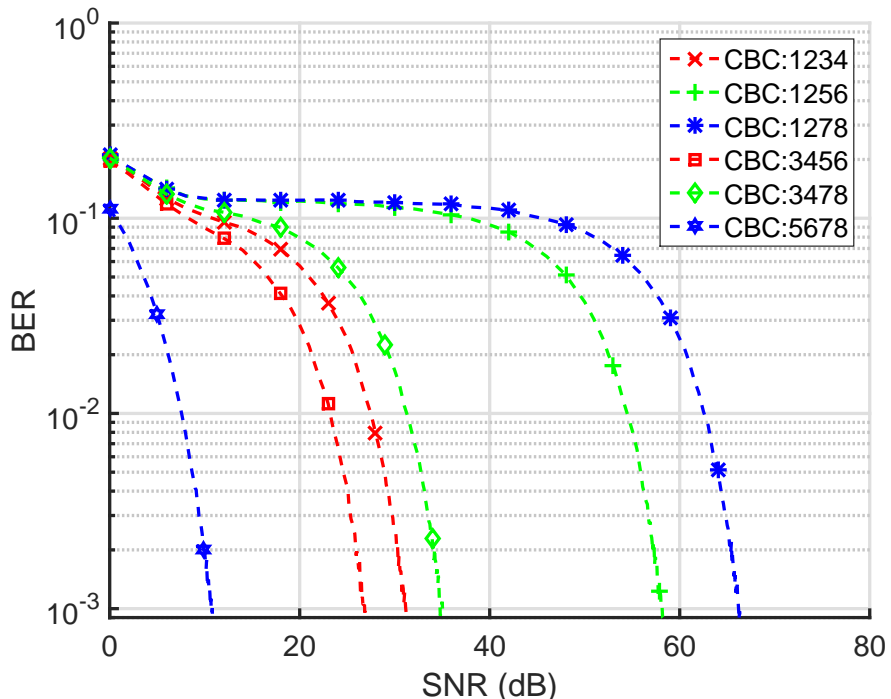
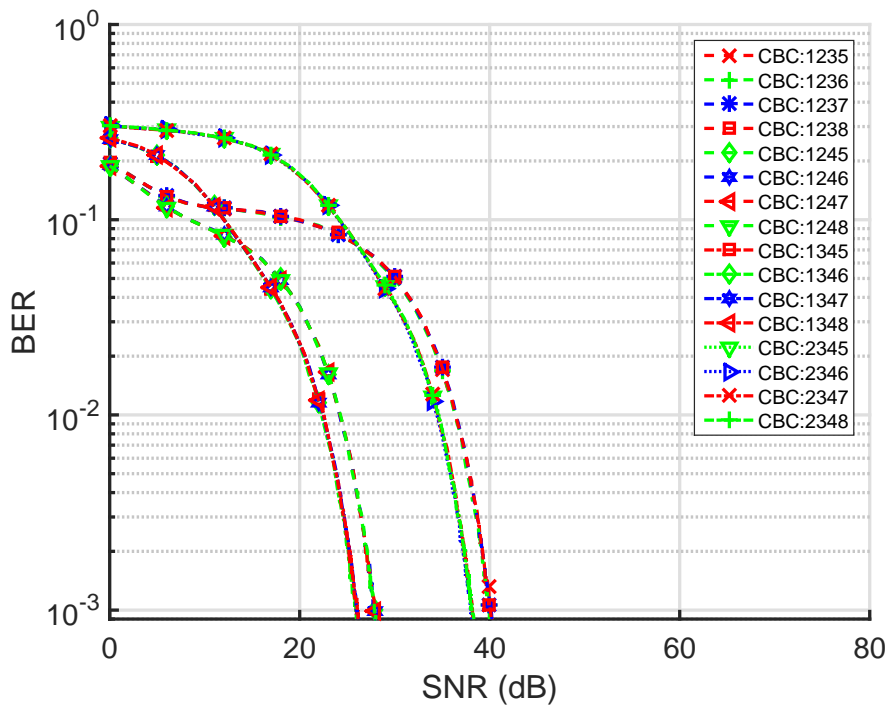


Figure 6·5: MM block diagram using IEEE 802.15.7 CBCs

to achieve desired illumination color and intensity using the CBC selected by the information to transmit. At the receivers, the incident radiant flux generates electrical signals which are used to estimate transmitted flux \hat{P}_d over each type of LED. Using the estimated fluxes, an estimate of active set of LEDs $\hat{\text{CBC}}_m$ can be made to recover transmitted information.

Figure 6·6 shows BER vs SNR performance for MM for $M = 4$ and 8 . For this analysis, a white chromaticity point of $(1/3, 1/3)$ is generated with the selected CBCs. 4-MM can be implemented with $D = 5, 6$ or 7 . 8-MM is implemented with $D = 7$. In absence of illumination constraint, 4-MM achieves the best performance with $D = 5$ using CBs from set $\{0, 1, 2, 3, 4\}$ for CBC set $\{5, 6, 7, 8\}$. Performance plots for 4-MM with $D = 6$ and 7 are also illustrated for comparison. Implementing 8-MM with CBCs as outlined in IEEE 802.15.7 requires about 60 dB of SNR and seems impractical. However, a different set of LEDs may be used to implement 8-MM to obtain a better performance.

Performance comparison of 4-MM at same illumination intensity level is illustrated in Figure 6·6. In this case, with $D = 5$, 4-MM with CBs from set $\{0, 1, 2, 4, 5\}$ for CBC set $\{3, 4, 5, 6\}$ outperforms others. CBC set $\{5, 6, 7, 8\}$ has a high luminous efficacy as compared to CBC set $\{3, 4, 5, 6\}$ and thus is constrained in radiant flux for signaling at a set illumination level. On comparing performance of 4-MM for all possible values of D , CBC sets $\{1, 2, 4, 5\}$, $\{1, 2, 4, 6\}$, $\{1, 2, 4, 7\}$ and $\{1, 2, 4, 8\}$ with $D = 6$ perform the best.

(a) 4-MM, $D=5$ (b) 4-MM, $D=6$

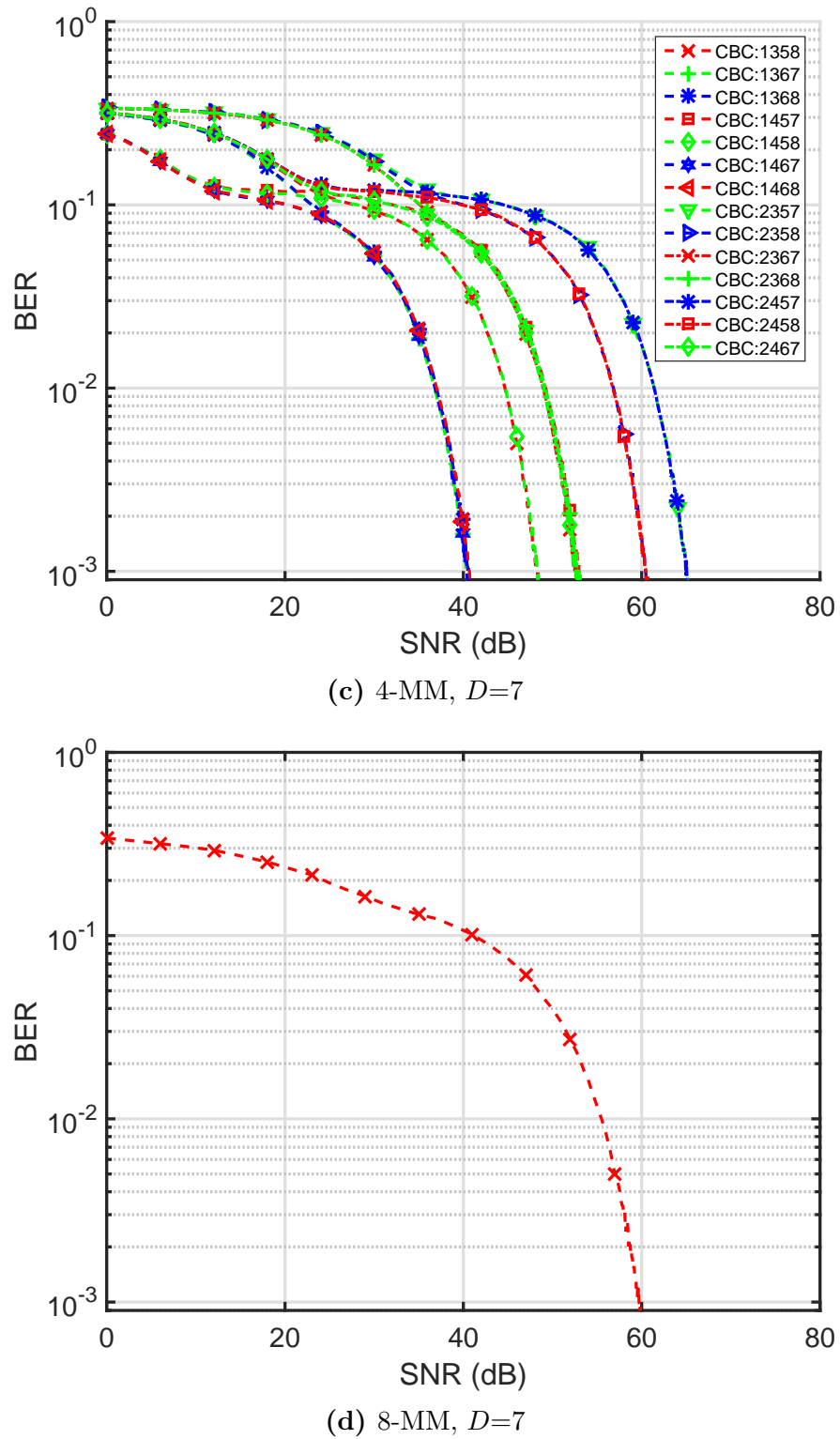
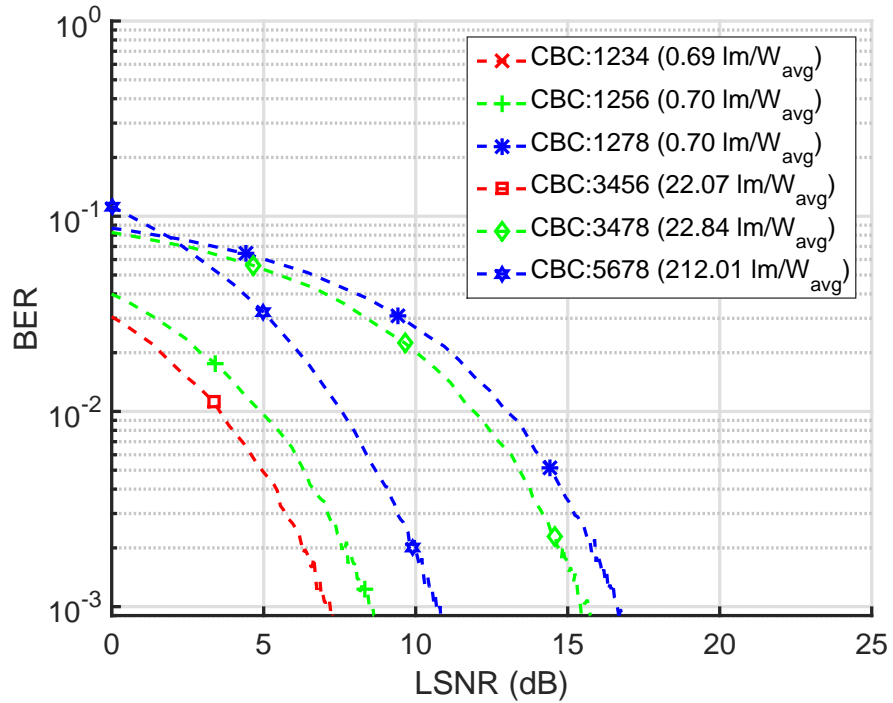
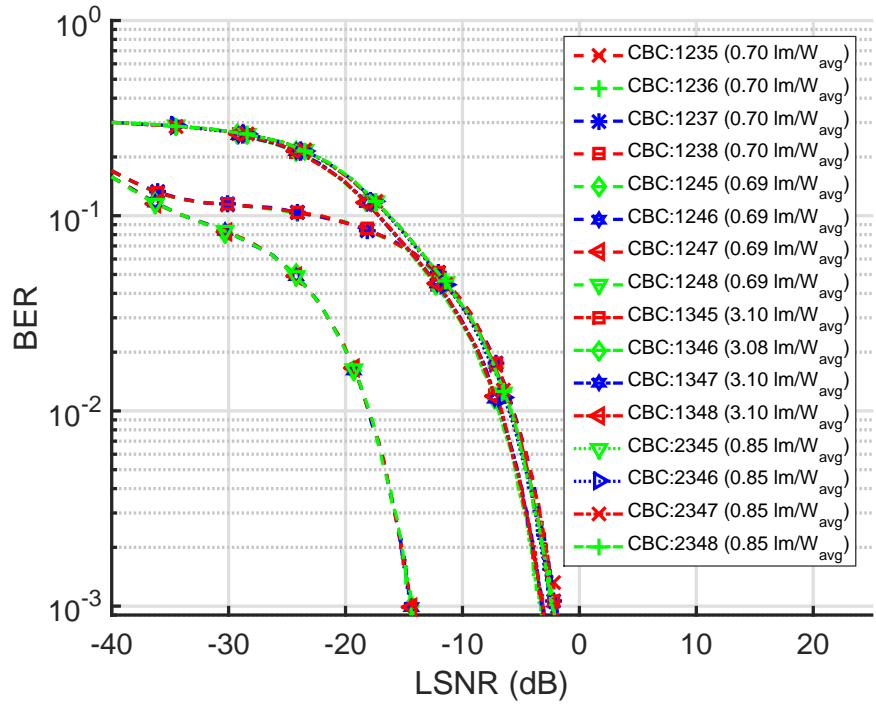


Figure 6.6: BER vs SNR for different combinations of CBC

(a) 4-MM, $D=5$ (b) 4-MM, $D=6$

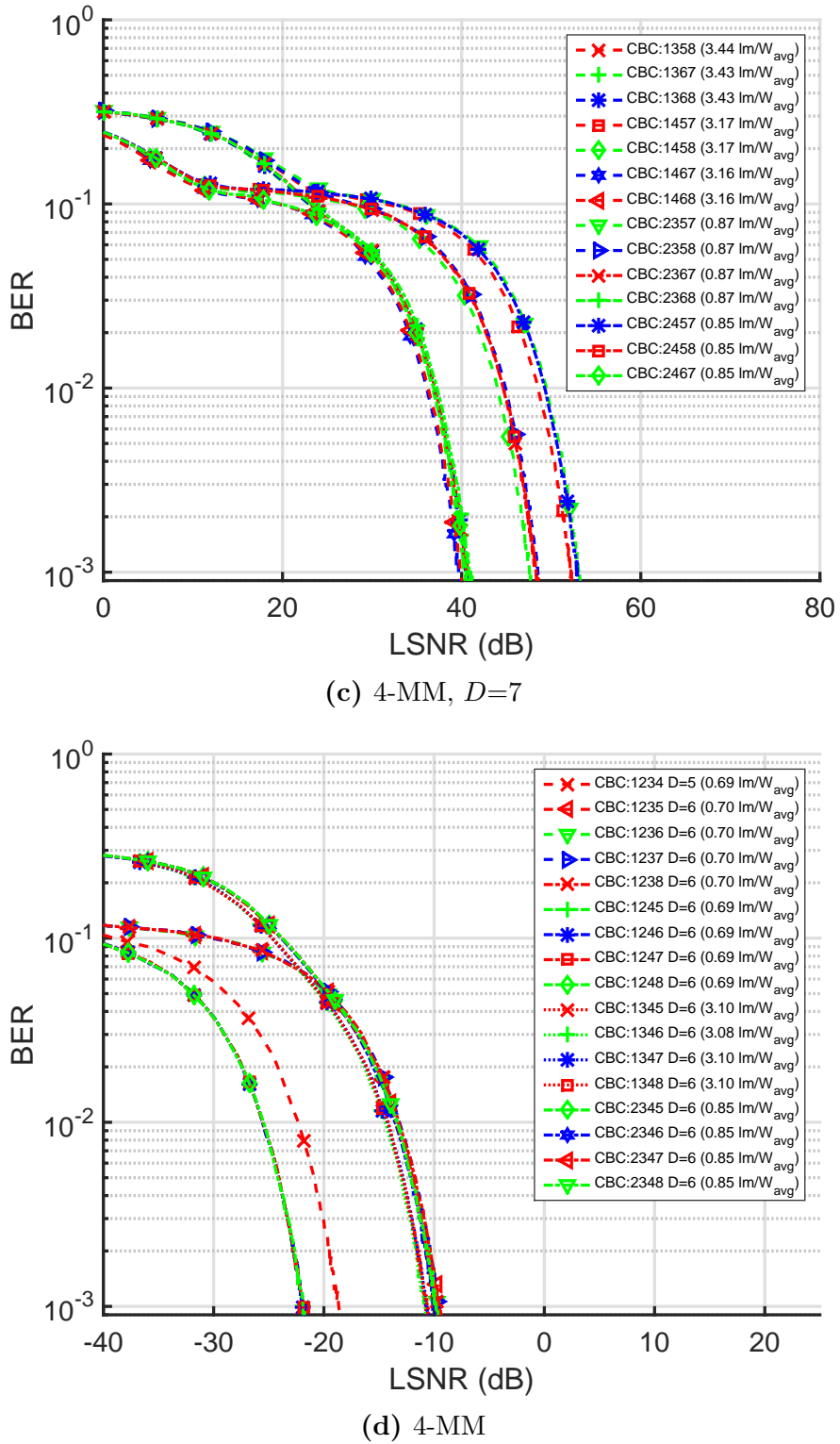


Figure 6.7: BER vs LSNR for different combinations of CBC

In this chapter, we have proposed MM, a novel modulation scheme for achieving constant color control in optical wireless communication using luminaires. This technique attempts to provide better color rendering for illumination while achieving wireless communication function. MM offers several advantages over CSK. In MM, to generate a set point, we can easily leverage MacAdams ellipses (Brown and MacAdam, 1949) to generate a color at a lower energy consumption point inside each ellipse. Such a technique cannot be applied to CSK because the average then would differ significantly from the set point. Additionally MM always generates the true requested ambient lighting state. The CSK constellation points always generate significantly different colors. Thus MM inherently has the ability to greatly reduce color flicker and improve color rendering.

Chapter 7

Optical wireless broadcast system design

The primary purpose of a lighting device is to provide illumination in indoor spaces. Any value added services within the luminaire must not disrupt this primary function. Thus it is important to seamlessly integrate OWC techniques while maintaining illumination targets. This chapter describes two such system designs.

7.1 Singular value decomposition based OWC system

MIMO VLC systems exploit the high SNR of a SISO channel offered due to typical illumination requirements to overcome the capacity constraints due to limited modulation bandwidth of LEDs. In this section, a singular value decomposition VLC (SVD-VLC)¹ MIMO system is outlined to integrate illumination commands with spatial MIMO OWC. This system can achieve high data rates while maintaining the target illumination and allowing the channel matrix to vary in order to support mobility in a practical indoor VLC deployment. The upper bound on spectral efficiency of the proposed SVD-VLC MIMO system is calculated assuming an imaging receiver. The relationship between the proposed system performance and system parameters such as power constraints, lens aperture and random receiver locations are described.

¹This work is published in peer-reviewed IEEE conference proceeding (Butala et al., 2013).

7.1.1 Native SVD system

In RF MIMO wireless communication systems where the channel state information (CSI) is known at the transmitter, SVD techniques apply coordinate system transformations to extract parallel independent links and maximize the capacity of the channel. The channel matrix \mathbf{H} can be decomposed into rotation and scaling matrices using SVD as

$$\mathbf{H} = \mathbf{U}\Lambda\mathbf{V}^* \quad (7.1)$$

\mathbf{U} and \mathbf{V} are unitary rotation matrices while Λ is a diagonal scaling matrix. Matrices \mathbf{H} and Λ have the same rank $\Gamma \leq \min(N_{tx}, N_{px})$. The diagonal elements of Λ ($\lambda_1 \dots \lambda_k \dots \lambda_\Gamma$) are the singular values of matrix \mathbf{H} and the squared singular values are the eigenvalues of $\mathbf{H}\mathbf{H}^*$. Now let us define new variables in rotated coordinate systems as

$$\mathbf{X}' \triangleq \mathbf{V}^*\mathbf{X} \quad (7.2)$$

$$\mathbf{Y}' \triangleq \mathbf{U}^*\mathbf{Y} \quad (7.3)$$

$$\mathbf{W}' \triangleq \mathbf{U}^*\mathbf{W} \quad (7.4)$$

Inserting the above definitions in MIMO channel model and then pre-multiplying both sides by \mathbf{U}^* transforms the MIMO channel model as

$$\mathbf{Y}' = \Lambda\mathbf{X}' + \mathbf{W}' \quad (7.5)$$

Figure 7.1 illustrates the transformed MIMO channel. \mathbf{X}' are the inputs for the data streams in the coordinate system defined by columns of \mathbf{V} and \mathbf{Y}' are the outputs in the coordinate system defined by columns of \mathbf{U} . Since \mathbf{U} is a unitary matrix, elements of \mathbf{W}' will be independent and identically distributed (IID) and have the same variance σ_n^2 as \mathbf{W} (Tse and Viswanath, 2005). Since Λ is a diagonal

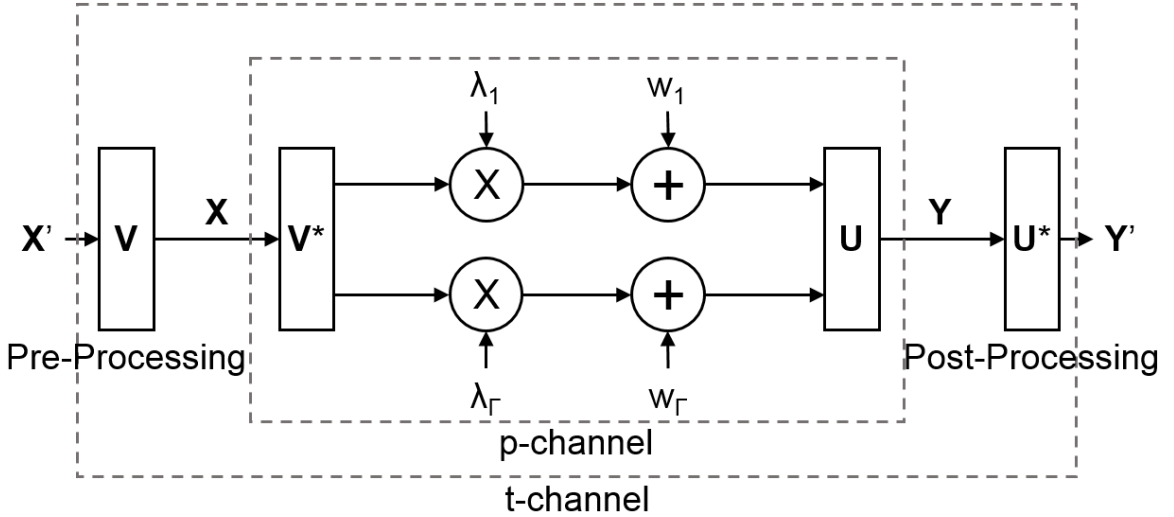


Figure 7.1: Native SVD system block diagram

matrix, extracting the simultaneous equations from Eq. (7.5) gives Γ simultaneous independent link models described by

$$y'_k = \lambda_k x'_k + w'_k; 1 \leq k \leq \Gamma \quad (7.6)$$

In RF MIMO systems, the aggregate transmit power is the binding constraint. The waterfilling algorithm (Goldsmith and Varaiya, 1997) provides a solution for allocate powers to the independent streams in order to maximize the channel capacity. As a result of this optimization, links with SNR greater than a threshold, are allocated power budget corresponding to their SNRs, while those with SNR below the threshold do not transmit any information. Let K'_k be these waterfilling power allocations. Then the capacity of the RF MIMO channel can be computed using Shannon's formulation (Shannon, 1948) and is given by

$$C_{\text{RF}} = \sum_{k=1}^{\Gamma} \log_2 \left(1 + \frac{\lambda_k^2 K'_k}{\sigma_n^2} \right) \quad (7.7)$$

7.1.2 SVD-VLC system outline

In the native SVD model, information streams are defined over inputs x'_k . Note $\lambda_k = 0$ for $k > \Gamma$ and thus no information can be transmitted over those links. At the transmitters, transformation \mathbf{V} multiplexes the streams over the physical channel. At the receiver, transformation \mathbf{U}^* demultiplexes the independent streams. These transformations are also called pre-processing and post-processing.

An SVD architecture with different power and offset allocation has been proposed for MIMO VLC communications in (Park et al., 2011). In this work, the aggregate sum of average radiated optical flux from multiple LEDs is constrained to be smaller than or equal to an upper bound in order to fulfill the eye safety requirements. Under this condition, it is still possible for the system to inadvertently violate the eye safety limit if the channel matrix is not full rank despite satisfying the stated constraints. Alternately, the system will under-utilize the capacity of the channel. Also, the illumination generated by that system changes with the channel matrix thus transitioning to a different illumination state every time the channel matrix is changed. Finally, the solution restricts itself to M -PAM and necessitates different optimization for different modulation schemes.

Native SVD does not impose any form of non-negativity or illumination constraint. The SVD-VLC architecture is derived from the native SVD architecture to perform OWC while satisfying illumination constraints. For indoor VLC system to provide illumination and optical wireless access simultaneously, the channel constraints are given by

Non-negativity constraint

For indoor VLC system, information is carried over an intensity signal which cannot be negative. Eq. (7.8) implies that input symbols should be defined to generate

positive values after pre-processing.

$$\mathbf{X} \geq \mathbf{0} \Leftrightarrow \mathbf{V}\mathbf{X}' \geq \mathbf{0} \quad (7.8)$$

Illumination constraint

In an indoor space, a user can specify a desired illumination state. This specifies the average radiant flux to be emitted by each luminaire. Eq. (7.9) states that the average radiant flux transmitted by each luminaire must equal the desired illumination state. Let \mathbf{P} be the vector that defines the average output radiant flux from each transmitter. Then \mathbf{P}' gives this constraint on the transformed links. This implies that the average signal value in the transformed space must be equal to the corresponding element of \mathbf{P}' .

$$E[\mathbf{X}] = \mathbf{P} \Leftrightarrow \mathbf{P}' = E[\mathbf{X}'] = \mathbf{V}^*\mathbf{P} \quad (7.9)$$

It is worth noting that \mathbf{X}' must satisfy the equation for all its elements irrespective of the channel gain of the corresponding transformed link. This implies that when the channel matrix \mathbf{H} or $\mathbf{\Lambda}$ is not full rank, the SVD-VLC architecture still expects the transformed links whose channel gain $\lambda_k = 0$ to maintain an average signal level as specified by this constraint. So even though these transformed links carry no information, it is vital to satisfy the average signal constraint to service illumination.

Input signal ranges

Eq. (7.10) specifies the set of values that \mathbf{X}' can take at any given instant of time provided the other constraints are satisfied.

$$\mathbf{M}[\mathbf{X}' \operatorname{sgn}(\mathbf{P}')] \geq \mathbf{0} \quad (7.10)$$

$\mathbf{M}[\cdot]$ is element by element magnitude operator. The above constraint states that the modulated signal for each luminaire can span either the non-negative or the non-

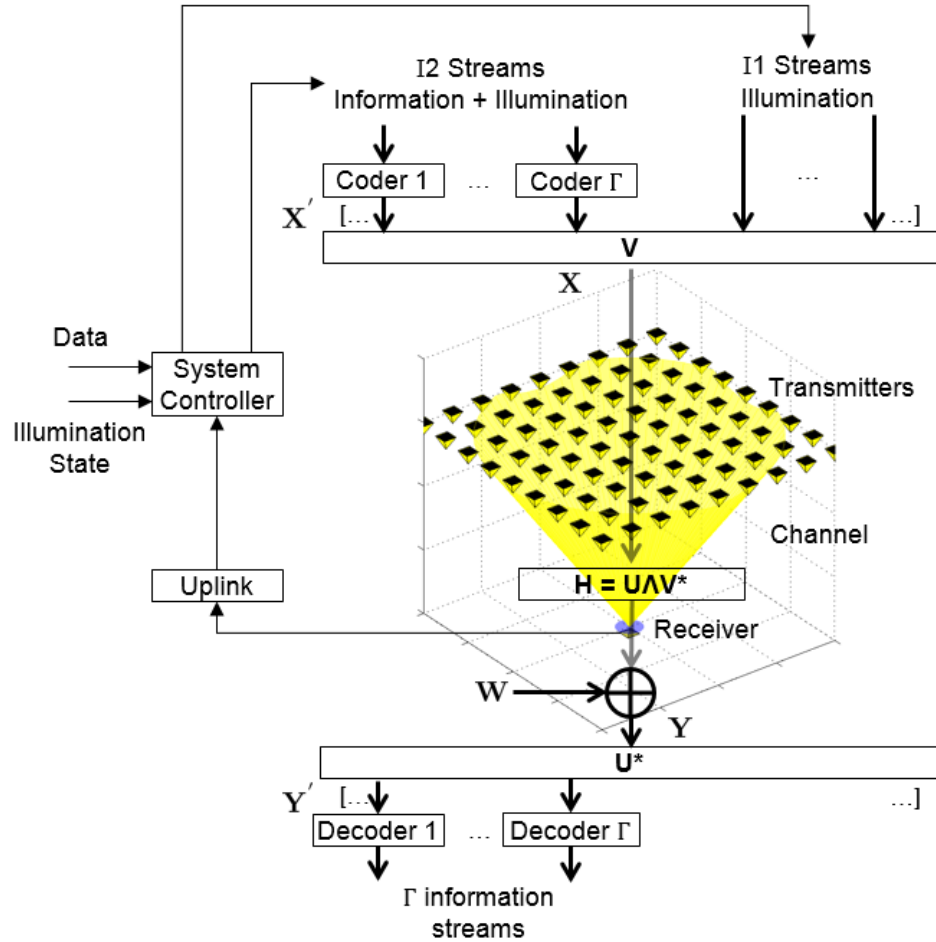


Figure 7.2: SVD-VLC system block diagram

positive but not both ranges of the Real number line as dictated by the illumination constraint.

SVD-VLC architecture

Figure 7.2 illustrates SVD-VLC system architecture. The system controller accepts information to be transmitted, illumination state and the estimated channel state for each user as inputs. During an active link, the information to transmit is relayed via an edge router. The illumination state requests can originate from indoor occupants or a ‘smart’ illumination controller. For most applications in indoor spaces, the user

is either static or mobile at a slow pace and thus a reasonably long coherence time can be assumed. In such a scenario, the channel state can be periodically estimated at the receiver from pilot signals and the state information can be transferred back to the system controller with a small overhead.

The system controller generates the different ‘optical’ streams to transmit. The ‘I1-streams’ are the $N_{tx} - \Gamma$ links that service only illumination. The ‘I2-streams’ are the Γ information + illumination bearing links. The I1 and I2 streams are pre-processed by \mathbf{V} to transform and multiplex them over the channel. This multiplexing generates and maintains the desired illumination state in the indoor space. At the receiver, the imaging optics separate the different optical streams. The TIAs for each pixel add white Gaussian noise to each link. Post-processing by \mathbf{U}^* demultiplexes the parallel links and recovers the Γ I2 streams. The streams can be jointly decoded to optimally recover the transmitted information. Thus the SVD-VLC architecture services the illumination while achieving high data rates over the VLC channel.

SVD-VLC spectral efficiency

The above signaling constraints reduce the maximum achievable spectral efficiency of the the optical channel when compared to an RF channel with AWGN at same total signal power and noise. The exact efficiency formulation for an indoor OWC channel with the above constraints can be obtained by information theoretic methods. However, it is instructive to treat the capacity formulation of Eq. (7.7) strictly as an upper bound to gain an insight into upper bounded performance gains.

7.1.3 SVD-VLC system performance

The upper bound on spectral efficiency of the optical MIMO channel with imaging receiver is analyzed and compared with an equivalent SISO channel. Table 7.1 outlines the system parameters used. For the MIMO channel, the luminaires are arranged in

Table 7.1: SVD-VLC system configuration parameters

Parameter		Value	Units
Room Length	L_{rm}	4	m
Room Width	W_{rm}	4	m
Room Height	H_{rm}	4	m
Transmiter grid pitch ¹	D_{tx}	0.5	m
Total number of transmitters ¹	$N_{tx}^L \times N_{tx}^W$	9x9	-
Transmitter Lambertian Order	m	1	-
Optics Field of View	ψ_c^o	60	degrees
Optics focal length ¹	f	5	mm
Optics transmission ¹	Q	1	-
Concentrator refractive index ²	η	1.5	-
Ideal filter transmission	$T(\lambda) \forall \lambda$	1	-
Sensor Side length	a_{rx}	5	mm
Pixel side length ¹	α_{rx}	1	mm
Pixel pitch ¹	δ_{rx}	1	mm
Total number of pixels ¹	$N_{px}^L \times N_{px}^W$	5x5	-
Responsivity	$R(\lambda) \forall \lambda$	0.4	A/W
Receiver bandwidth	B	50	MHz
TIA noise current density	I_{pa}	5	pA/ $\sqrt{\text{Hz}}$

¹ MIMO specific parameter

² SISO specific parameter

a grid at the a height of 3 m in the room and at a pitch of D_{tx} . The luminaires are assumed to be point sources with enough output luminous flux to provide the desired illumination. The SPD of the emitted flux is approximated using sum of Gaussians to that used in (Grubor et al., 2008). The receiver bandwidth is assumed to be 50 MHz (Zeng et al., 2008). For this analysis the receiver is always assumed located at the center of the length-width plane. The same sensor side length a_{rx} is maintained for the SISO photodiode and the imaging receiver. The case where the aperture collection area of the imaging receiver is the same as the area of the SISO receiver is also considered.

Figure 7.3 shows the upper bound on spectral efficiency of the SISO and MIMO channels over a range of signal power constraints and different lens aperture diameters

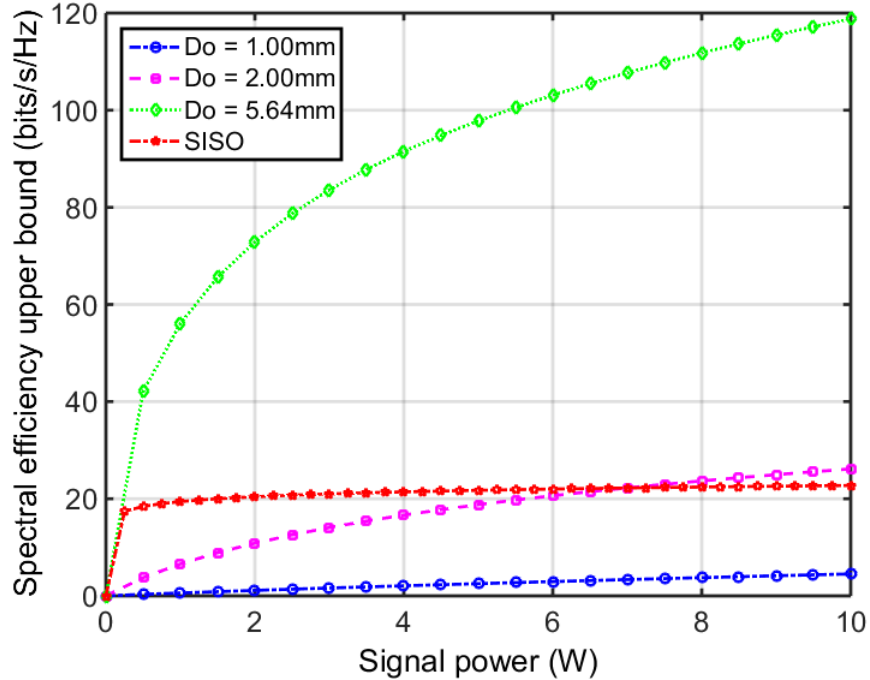


Figure 7.3: Spectral efficiency upper bound vs dimming

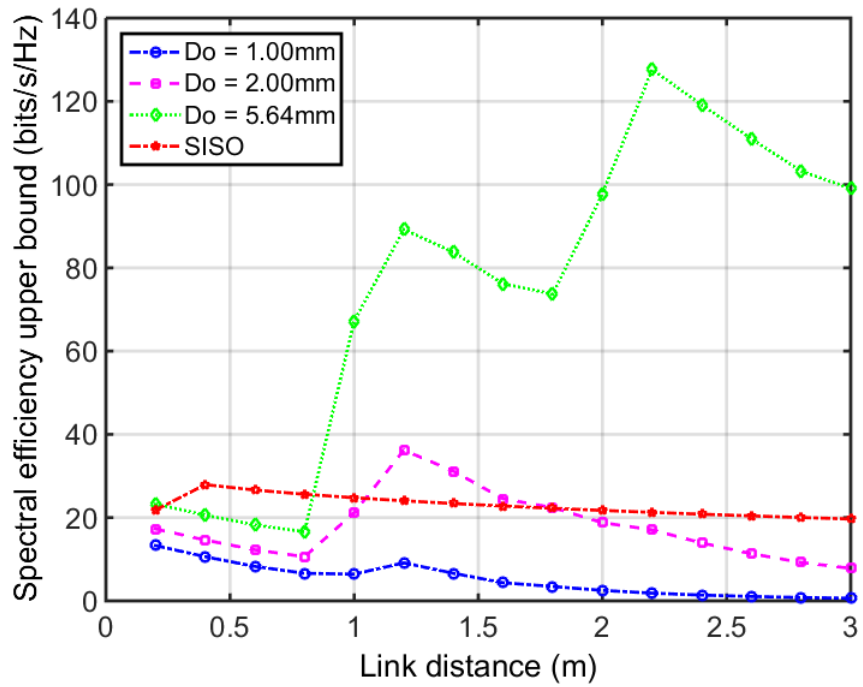


Figure 7.4: Spectral efficiency upper bound vs link distance

when the receiver is at the center of the 1 m plane. The upper bound on spectral efficiency of the MIMO VLC channel is then calculated at the same average power constraints as a SISO channel. As expected, the spectral efficiency of the imaging channel does increase with increasing aperture diameter. At aperture diameter of 5.64 mm, the imaging receiver and the SISO receiver collect the same amount of average radiant flux, however the MIMO channel shows huge spectral efficiency gains. This gain can be explained by the introduction of multiple parallel links due to the imaging receiver architecture and the reduction in ambient shot noise per channel as indicated in (Djahani and Kahn, 2000). While the imaging receiver collects the same amount of ambient flux as the SISO receiver, this flux can be assumed to be equally divided among all the pixels on the receiver due to imaging optics. Thus each link has greatly reduced ambient flux, thus reducing the noise. The limiting factor in this case is the thermal noise.

Figure 7·4 shows spectral efficiencies calculated at different link distances when the average signal power is 5 W. The link distance here is defined as the length of a vector from origin of the receiver coordinate system along $\hat{\mathbf{z}}$ when it intersects the transmitter plane. The SISO channel spectral efficiency monotonically decreases with increasing link distance. The spectral efficiency of the MIMO channel goes through regions of positive (increasing) and negative (decreasing) slopes.

As seen in Figure 7·5a, at the 1 m link distance, only 1 transmitter is in the receiver's FOV while adjacent transmitters are just outside the FOV. Increasing the link distance to 1.2 m causes the adjacent transmitters to enter the receiver FOV, increasing the number of parallel channels as seen in Figure 7·5b. The corresponding increase in spectral efficiency is greater than the small decrease caused by the increasing link distance. Thus the MIMO channel spectral efficiency curve has a positive slope upto 1.2 m. Between 1.2 m to 1.8 m, number of transmitters seen by receiver

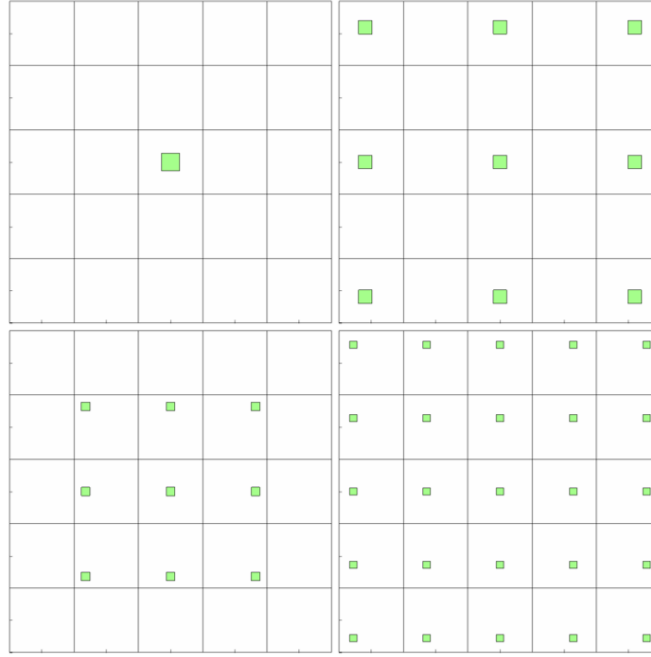


Figure 7.5: Spots (magnified for better illustration) as projected on the imaging receiver sensor plane at different link distances which are (a) top left: 1.0 m (b) top right: 1.2 m (c) bottom left: 2.0 m (d) bottom right: 2.2 m

remain the same as the link distance is further increased. This causes the spectral efficiency of each individual link to decrease thus causing an overall decrease in the channel spectral efficiency from 1.2 m to 1.8 m. Figure 7.5c shows the transmitters projected on the receiver at a link distance of 2.0 m where one can see more adjacent transmitters begin to enter the receiver FOV and at 2.2 m as in Figure 7.5d, the transmitters are completely in the receiver FOV thus causing an increase in spectral efficiency due to more parallel channels. From 2.2 m to 2.8 m, no more transmitters enter the receiver FOV and thus the overall spectral efficiency decreases with increasing link distance.

To illustrate generation and maintenance of an illumination state using the SVD-VLC architecture, three different scenarios for different illumination states were simulated using SVD-VLC. For these scenarios, the uniform illumination constraint was

Table 7.2: SVD-VLC simulation illumination constraints

Case	Dominant luminaire(s)	400lx Setpoint location
a	[1 3 3]'	[1 3 1]'
b	[3 1 3]'	[3 1 1]'
c	[1 1 3]’ and [3 3 3]’	[2 2 1]’

relaxed. Table 7.2 now outlines the new illumination constraints. The dominant luminaire(s) column specifies the transmitter(s) whose average output radiant flux was configured to be 20 x that as compared to each of the other transmitters. Setpoint location column specifies the location in the room where 400 lx illumination is requested. The combination of these two values specifies a unique illumination state for each scenario. The constraints were specified in this manner to prevent an unacceptably high illumination level at any other point on the illumination surface. A more complex illumination state can be imposed as a constraint to generate a particular light field, however this simple case is sufficient to illustrate the SVD-VLC behavior.

Receiver locations at four different time instants are chosen pseudo-randomly to simulate a varying channel matrix due to mobility. For each of the three scenarios, a 1024 length long data sequence was generated from a uniform distributed pseudo-random number sequence in the (0, 1) range. The data sequence was scaled to meet the average signal constraint specified by \mathbf{P}' and I1 and I2 streams were generated. After multiplexing these streams over the p-channel, the resulting illumination state was calculated as illustrated in Figure 7.6. Table 7.3 shows values for the illumination

Table 7.3: SVD-VLC simulation illumination results

Receiver		Illumination (lx)		
Location	Rank(H)	a	b	c
[1.6 0.6 1.0] ^T	16	399.99	400.29	400.22
[2.8 0.4 1.4] ^T	12	400.00	401.75	400.00
[0.2 0.8 1.0] ^T	12	399.81	399.92	401.26
[1.2 1.4 1.6] ^T	9	400.06	400.01	401.97

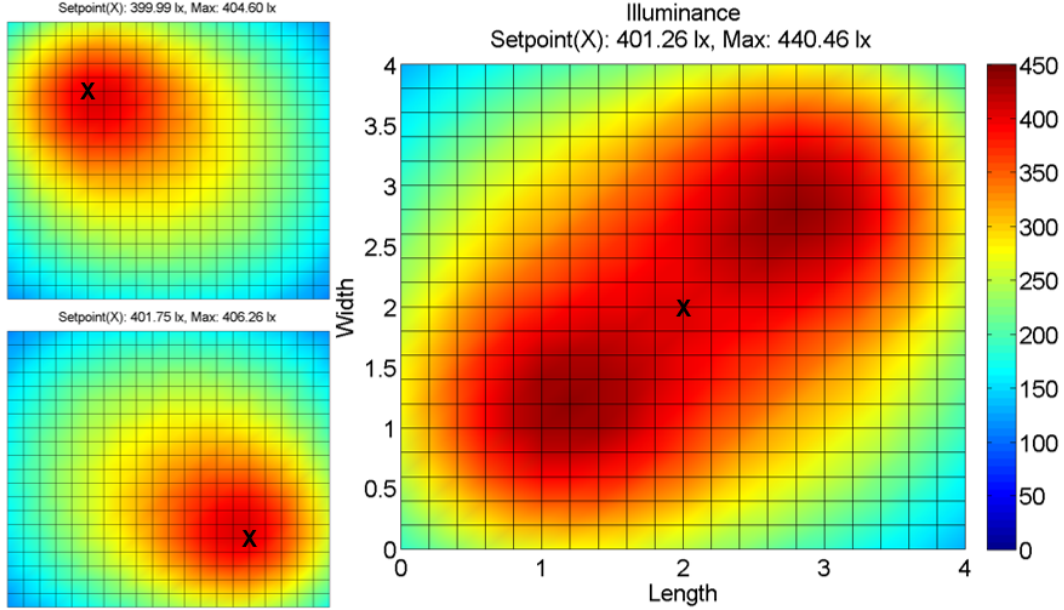


Figure 7·6: Generation and maintenance of illumination state by SVD-VLC. 'X' marks the setpoint location in the illumination plane at 1 m height. Scenarios: (a) Top left (b) Bottom left (c) Right

achieved at the setpoint location as the channel matrix varies with the receiver's location. It can be seen that despite the variations in the channel matrix, the illumination state remains nearly constant.

In this section, a novel SVD-VLC architecture is introduced to implement MIMO VLC channel with an imaging receiver while maintaining illumination. It is shown that for the same received radiant flux, MIMO channel with imaging receiver offers large spectral efficiency gains over the equivalent SISO channel. Additionally, the concept of using I1 and I2 streams to transmit information without affecting illumination is introduced. It is also shown that the system can achieve and maintain a user defined illumination state under changing channel conditions. SVD-VLC system does require the CSI to be known at the transmitter and receiver. While it may be possible in a pseudo-static indoor scenario to acquire this information with minimal resource overhead, it does add complexity to the system.

7.2 Multi-wavelength OWC system

Most VLC systems constructed to date focus on using a broad visible band generated by phosphor-converted LEDs, or by filtering to isolate the blue component from these sources. Multi-wavelength systems² consider additional wavelength bands that are combined to produce the desired lighting output along with OWC. Color combining, or mixing, realizes desired color temperature and intensity and represents a form of wavelength-division multiplexing. This section investigates the relationships between the colors comprising the lighting source for a range of lighting states, the spectral separation of communication channels, the relative intensities required to realize lighting states, how modulation can be most effectively mapped to the available color channels, and the design of an optical filtering approach to maximize SNR while minimizing crosstalk at the receiver. Simulation results based on a three colored VLC system are discussed using O-OFDM for each color. It is shown that the system is the most power efficient at 6250 K correlated color temperature, with transmitter spectral spread of 5 nm and filter transmittance width of 40 nm.

7.2.1 WDM system outline

Different colors including shades of white for illumination on the black body radiation curve can be produced by mixing different amounts of narrow-band SPDs emitted by different sources. The ability to combine multiple narrow-band sources to generate white light also provides the benefit of being able to transmit concurrent information streams over different color groups; thus enabling WDM. As discussed before, the MIMO OWC system can be represented by the model in Eq. (7.11)

$$\mathbf{Y} = \mathbf{H}\mathbf{X} + \mathbf{W} \quad (7.11)$$

²This work is published in peer-reviewed IEEE conference proceeding (Butala et al., 2014c).

\mathbf{X} is a vector containing radiant fluxes emitted by N_{tx} transmitting elements over different colors. \mathbf{H} is $N_{rx} \times N_{tx}$ dimensional channel matrix where each element h_{ij} represents channel gain from transmitter j to receiver i . \mathbf{W} is the N_{rx} dimensional AWGN vector. \mathbf{Y} is the vector of N_{rx} received electrical signals.

Lasers and LEDs produce a much smaller SPD spread as compared to incandescent and fluorescent sources and are thus preferable for WDM. LED emission can be modeled with a Gaussian distribution as in Eq. (7.12a) while laser emission can be modeled with a Lorentzian distribution as in Eq. (7.12b). Equations in (7.12) model emission spectra for the j^{th} transmitting element.

$$S_j(\lambda) = \frac{1}{\sqrt{2\pi\sigma_j^2}} \exp\left[-\frac{(\lambda - \lambda_j)^2}{2\sigma_j^2}\right] \quad (7.12a)$$

$$S_j(\lambda) = \frac{1}{\pi} \frac{0.5\Gamma_j}{(\lambda - \lambda_j)^2 + (0.5\Gamma_j)^2} \quad (7.12b)$$

where λ_j is the dominant wavelength of emission, σ_j is the measure of spread (deviation) from the dominant wavelength for the Gaussian model, and Γ_j is the full width at half maximum (FWHM) from the dominant wavelength for the Lorentzian model. At small SPD spread, most of the optical power is emitted at the dominant wavelength. At larger SPD spread the optical power is distributed across a larger wavelength range and starts overlapping across different transmitting elements, thus causing interference. White light with SPD $W(\lambda)$ can be generated by combining emissions from different transmitting elements. The chromaticity coordinates for $W(\lambda)$ can be then be computed by using Eqs. (5.6)–(5.7) as described in section 5.4.

Illumination color to rendered by luminaires is specified by correlated color temperature (CCT) in Kelvin units. To understand CCT, consider spectral radiance of a black body heated to temperature T Kelvin as stated by Planck's law and given by

$$S(\lambda) = \frac{2hc^2}{\lambda^5 \left[\exp\left(\frac{hc}{\lambda kT}\right) - 1 \right]} \quad (7.13)$$

where h is the Planck's constant, c is speed of light, and k is Boltzmann's constant. Replacing $W(\lambda) = S(\lambda)$ in Eqs. (5.6)–(5.7) chromaticity coordinates $[x, y]$ associated with a black body heated to temperature T can be computed. In this context T is known as the CCT for color represented by $[x, y]$. Recall that two different SPDs can generate the same chromaticity coordinates due to the principle of metamerism. A luminaire specified to render a CCT value will generate an SPD that is metamerically equivalent to the SPD emitted by a black body heated to specified CCT.

Traditionally luminaires have been specified to generate a certain CCT with colors at lower temperature appearing (ironically) warmer than those at higher temperatures. It is practical to generate colors off the black body radiation curve using different colored sources. This analysis considers only the colors generated on the black body radiation curve. As the CCT changes from a lower value to a higher value, the optical power available to transmit information on any color channel varies thus affecting the overall communication performance.

Optical filters can be manufactured to permit narrow-bandpass filtering using plasmonics (Xu et al., 2010; Yokogawa et al., 2012). Broad-bandpass optical filters that make use of interference are widely available. The transmittance of these filters can be modeled as Lorentzian functions of wavelength. The choice of the filter FWHM is a tradeoff to collect the maximum signal while rejecting interference and background illumination.

Responsivity of the receiving elements also affects the aggregate system performance. It depends on the quantum efficiency of the material of sensor. Reference (Z. Ghassemlooy, 2012) computes responsivity as

$$R(\lambda) = \frac{\xi\lambda}{1240} \quad (7.14)$$

where ξ is the quantum efficiency of the material, and λ is wavelength of interest. For

equal signal radiant flux, signals that span wavelength ranges with lower responsivity will perform poorly as compared to the rest.

Optical spectrum outside the visible range like infrared (IR) and ultraviolet (UV) spectrum can also be utilized for WDM. IR and UV do not generate chromatic response on human eye and thus do not contribute to visible illumination. Thus, as long as their emissions satisfy eye and skin safety regulations, using this additional optical spectrum can only boost the channel capacity.

7.2.2 WDM system performance

This subsection studies how the choice of design parameters like illumination CCT, transmitter SPD, and filter FWHM affect the performance of a multi-wavelength VLC system. Three transmitting elements with Gaussian emission spectrum at dominant wavelengths of red (627 nm), green (530 nm) and blue (470 nm) are selected. Using these transmitting elements, CCT range of [2500 7000] K is sought. SPD spread within [5 50] nm is considered. Figure 7.7 illustrates normalized SPDs needed to achieve the range of CCTs for transmitting elements with 5 nm spread.

Unique $t_R : t_G : t_B$ ratios are generated after varying the tristimulus values in the range [0 1] in 0.1 unit steps. Chromaticity coordinates for resulting SPDs are calculated. An initial characterization step generates a pre-populated table consisting of the tristimulus values and corresponding chromaticity coordinates. Chromaticity coordinates for each CCT are also pre-computed. From the pre-computed table, the tristimulus values that achieve the closest chromaticity are selected. The SPD is then scaled to achieve target illumination (400 lx) at the receiver that is located at a distance of 2 m from the transmitter. The surface normals of the transmitter and receiver are assumed to be parallel.

Optical filter's passband can be designed to center on the transmitting elements' dominant wavelengths. Optical filters for the simulation are modeled to have Lorentzian

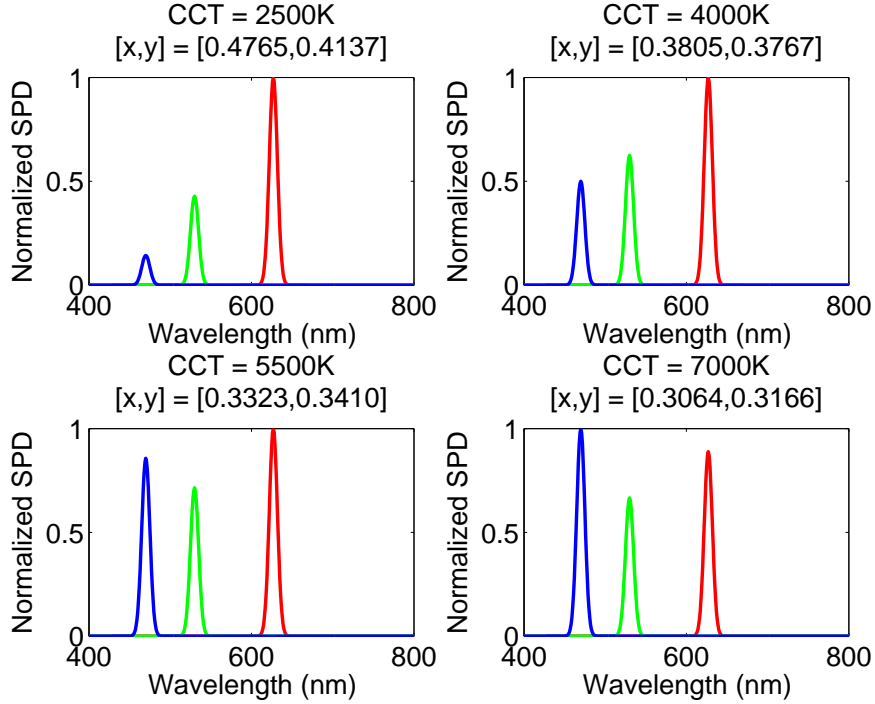


Figure 7.7: Transmitting element normalized spectral power distribution

transmittance with ideal value 1 at the dominant red, green and blue wavelengths mentioned above. Filter transmittance as a function of wavelength is illustrated in Figure 7.8. Filter FWHM considered for the analysis lie in [1 250] nm range.

The receiver sensor is assumed to be made of silicon. The assumed quantum efficiencies and responsivity of the sensor taken from online source is illustrated in Figure 7.9. The responsivity near the blue wavelength is about 0.29 A.W^{-1} and increases steadily to about 0.46 A.W^{-1} near the red before rapidly reducing as the energy of the incident photon approaches the bandgap energy of silicon.

To analyze the system performance with reasonable number of iterations, transmitting and receiving elements are restricted to the same deviations about their respective means. A random bit stream is then generated. Bits for each link are then communicated using asymmetrically clipped offset and DC-biased optical orthogonal

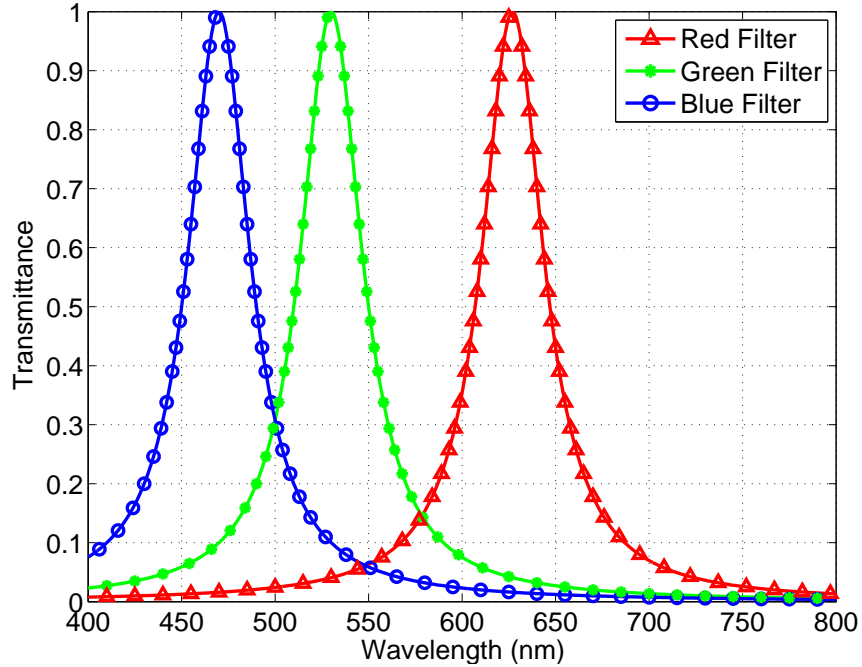


Figure 7.8: Filter transmittance for FWHM = 40 nm

frequency division multiplexing (ACO-OFDM and DCO-OFDM). Details on these optical OFDM techniques can be found in references (Carruthers and Kahn, 1996; Armstrong and Lowery, 2006). For this simulation, ACO-OFDM and DCO-OFDM are implemented with 64 sub-carriers and 64-QAM and 8-QAM modulation, respectively. This ensures that both schemes achieve similar bits/symbol with ACO-OFDM achieving 96 bits/symbol and DCO-OFDM achieving 93 bits/symbol. The DC level on each link is set to ensure the desired CCT is achieved at the 400 lx illumination level. This generates the transmit vector \mathbf{X} .

Having established $N_{tx} = 3$ transmitting and $N_{rx} = 3$ receiving elements, the 3×3 channel matrix \mathbf{H} can be computed. AWGN vector \mathbf{W} is generated and is then added to the transmitted vector. With the knowledge of the transmitted signal power and by varying the receiver noise, simulations over a range of $\text{SNR}_{\text{avg}}^{\text{tx}}$ as defined in Eq. (3.18) are carried out. Vector \mathbf{Y} then collects the received signal and the added noise and interference. The least squares estimate of the transmitted signal vector is

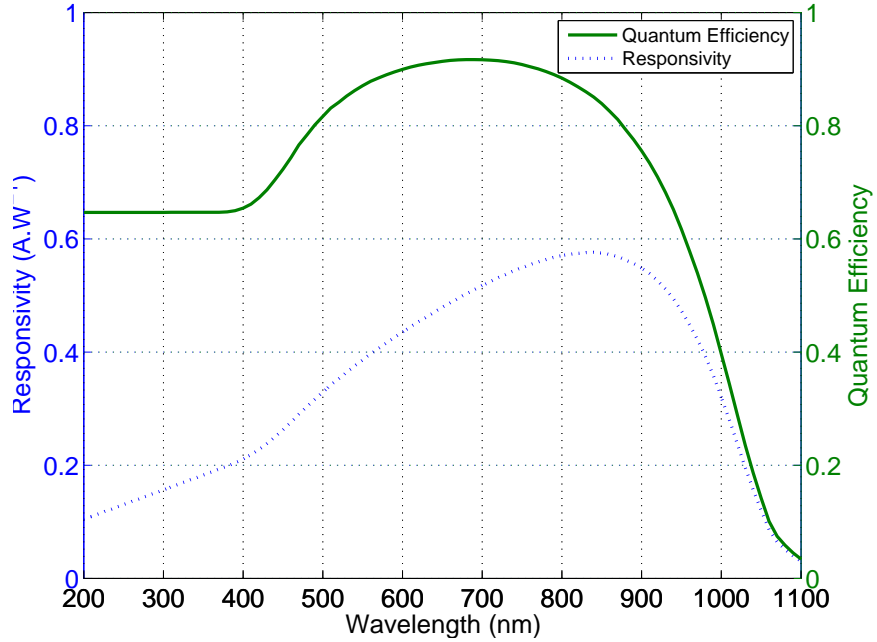


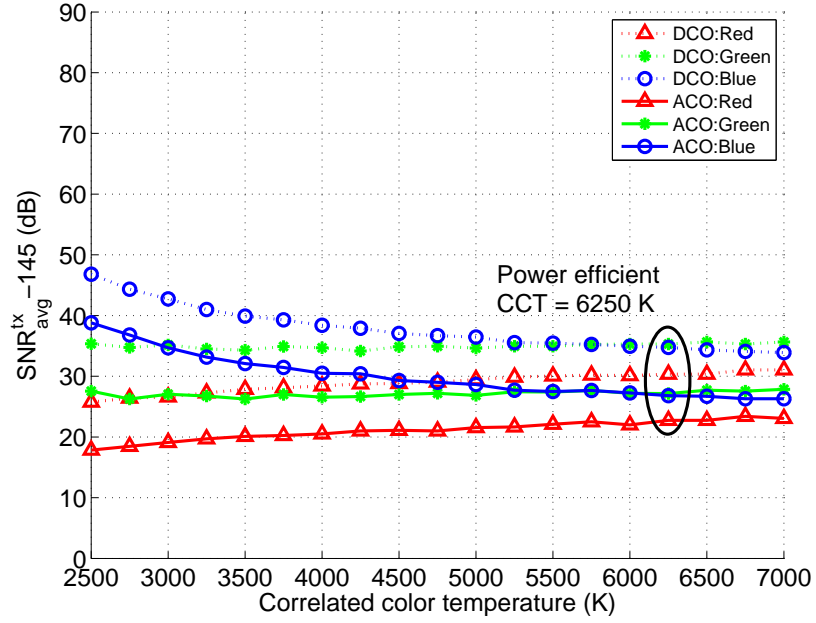
Figure 7.9: Receiver quantum efficiency and responsivity

computed as

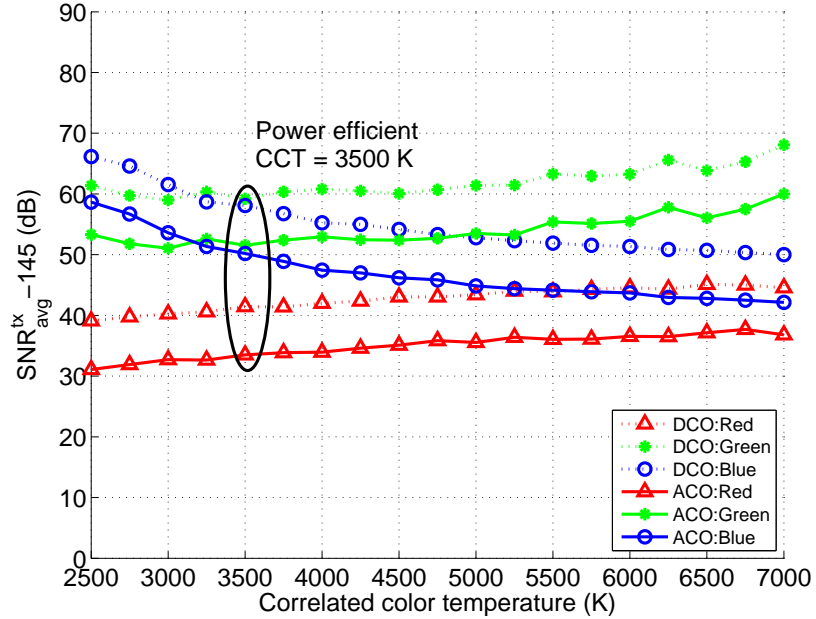
$$\hat{\mathbf{X}} = (\mathbf{H}^* \mathbf{H})^{-1} \mathbf{H}^* \mathbf{Y} \quad (7.15)$$

An estimate of the transmitted optical OFDM frame for each color is obtained by aggregating least squares estimates of the received signal vectors. Further signal processing on each optical OFDM frame gets an estimate of the transmitted QAM symbol. Decoding the QAM symbols provides an estimate of the transmitted bits. BER is then calculated by comparing the transmit and estimated bit-streams.

For each unique configuration yielded by varying the parameters, BER versus $\text{SNR}_{\text{avg}}^{\text{tx}}$ is empirically determined using monte-carlo simulations. Based on the simulation setup, the path-loss from the transmitting elements to the receiving elements is about 145 dB. To plot the change in system performance when each parameter is varied, the minimum $\text{SNR}_{\text{avg}}^{\text{tx}}$ needed to achieve target $\text{BER} \leq 10^{-3}$ is selected. Since ACO-OFDM is more power efficient compared to DCO-OFDM, for all the cases discussed below, ACO-OFDM needs lower transmit signal power to achieve the target



(a) Most power efficient operation point



(b) High inter-channel interference

Figure 7.10: $\text{SNR}_{\text{avg}}^{\text{tx}}$ vs correlated color temperature to achieve $\text{BER} \leq 10^{-3}$

- (a) Transmitter: $\sigma_r = \sigma_g = \sigma_b = 5 \text{ nm}$; Filter: $\Gamma_r = \Gamma_g = \Gamma_b = 40 \text{ nm}$
- (b) Transmitter: $\sigma_r = \sigma_g = \sigma_b = 50 \text{ nm}$; Filter: $\Gamma_r = \Gamma_g = \Gamma_b = 250 \text{ nm}$

BER as compared to DCO-OFDM.

The change in performance of the red, green and blue links as the CCT is varied from 2500 K to 7000 K is shown in Figure 7·10. At 2500 K, the SPD has a greater contribution from red, then green and then blue. Thus the red link achieves target BER at lower transmitted signal power. As the CCT increases, relative signal power from the red link decreases, that of the green remains similar, and that of the blue increases. Thus, with increase in CCT, the amount of aggregate transmit flux needed to achieve target BER from the red link starts increasing, that of the green remains relatively unchanged, while that of the blue decreases. For the specified multi-wavelength system, CCT = 6250 K provides the most power efficient operating point as illustrated in Figure 7·10a. Increasing the transmitting elements' SPD or the filter FWHM introduces increasingly more ICI. This causes the most power efficient operating point to shift towards CCT = 3500 K but with greater power requirements as seen in Figure 7·10b.

The change in performance of the red, green and blue links as the transmitting element SPD spread is varied from 5 nm to 50 nm is shown in Figure 7·11. As the SPD spread is increased, the performance of all three links degrade. This can be attributed to two factors. Initially, as the signal power is distributed across a larger wavelength range, with the filter transmittance function remaining the same, increasingly more signal gets rejected by the filter. Thus the receiver collects a smaller fraction of the signal power, degrading the performance. Secondly, as the individual SPDs spread enough, they start overlapping and causing ICI. The effect of ICI is more pronounced on the green link because it gets interference from both, red and blue. Thus transmitter consisting of transmitting elements with narrower emission spectra are more power efficient than those with wider emission spectra. Experiments in reference (Neumann et al., 2011) qualitatively measure color perception for illumination

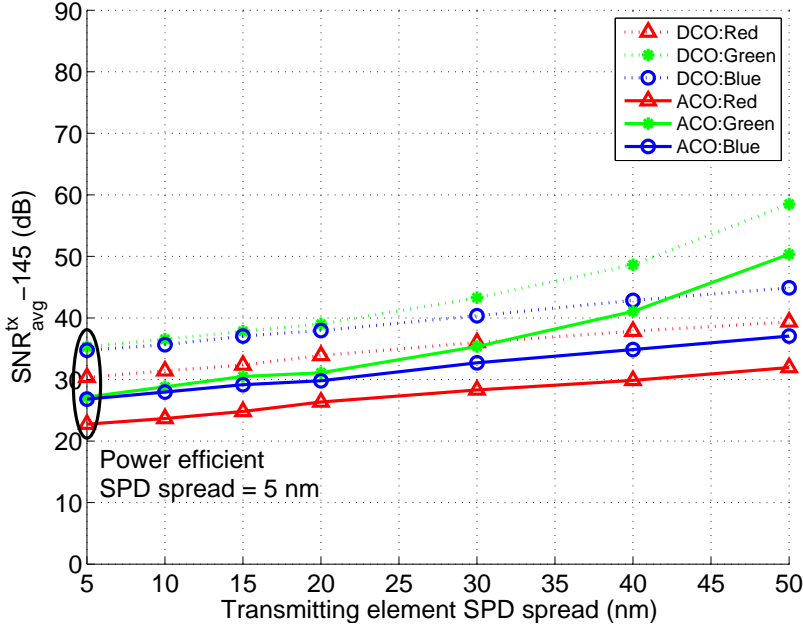


Figure 7.11: $\text{SNR}_{\text{avg}}^{\text{tx}}$ vs transmitting element SPD spread to achieve $\text{BER} \leq 10^{-3}$
Filter: $\Gamma_r = \Gamma_g = \Gamma_b = 40 \text{ nm}$; CCT = 6250 K

with narrow-band sources and find lasers could be used for general lighting. However, it is also commonly believed that sources with spiky emission spectra do not produce good quality of illumination because objects with reflectance spectra lying outside the spikes in the illumination spectra will be perceived to be poorly lit. The choice of the transmitting elements' SPD spread would be a tradeoff between the communication and illumination performance. For the specified multi-wavelength system, SPD spread = 5 nm provides the most power efficient operating point.

The change in performance of the red, green and blue links as the receiving element filter FWHM is varied from 1 nm to 250 nm is shown in Figure 7.12. As the filter FWHM increases, initially the system performance improves significantly. At these lower FWHM ranges, the filters transmit a smaller fraction of the signal to the sensors and thus performance is limited by the amount of signal power collected for each link. At higher FWHM ranges, along with additional signal, the filters permit

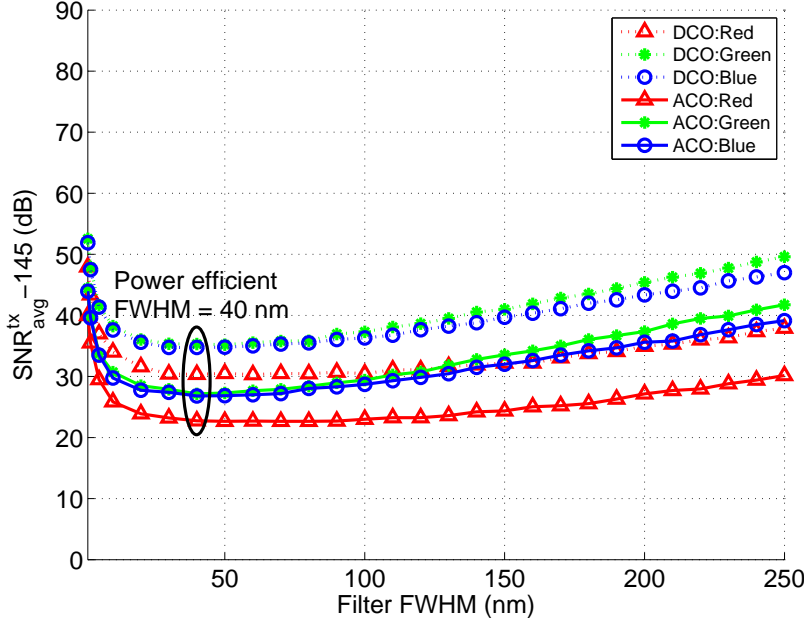


Figure 7.12: $\text{SNR}_{\text{avg}}^{\text{tx}}$ vs filter FWHM to achieve $\text{BER} \leq 10^{-3}$
Transmitter: $\sigma_r = \sigma_g = \sigma_b = 5 \text{ nm}$; CCT = 6250 K

increasingly more ambient light and interference from neighboring links, thus degrading the performance. For the specified multi-wavelength system, filter FWHM = 40 nm provides the most power efficient operating point.

In this section, design paradigm for a multi-wavelength VLC system in the context of variable illumination constraints is presented. VLC system performance is characterized for variations in illumination CCT, transmitter SPD spread, and the receiver filter transmittance FWHM. For the three colored system considered, the blue and the green links pose the performance bottlenecks because of the relatively lower contribution to the SPD and lower PD responsivity as compared to the red. As the ICI increases, the most power efficient CCT shifts towards lower temperatures. Transmitting elements with the smallest spectral spread provide the most power efficient operating point. The effect of increase in spectral spread is most pronounced in the green link because it suffers the most from interference from the blue and red links. Filters with narrow transmittance FWHM reject a lot of the signal power while

filters with a broad transmittance FWHM accept a lot of interference. Both of these affect the power efficiency of the system. For the setup considered, the most power efficient operating point is for ACO-OFDM at CCT = 6250 K, transmitting element SPD spread = 5 nm, and filter FWHM = 40 nm.

Chapter 8

Conclusions

Technology for wireless information access has enabled innovation of ‘smart’ portable consumer devices. These have been widely adopted and have become an integral part of our daily lives. Networking forecasts indicate a rapid rise in data consumption by portable devices in years to come. Wireless access infrastructure in its current state cannot keep pace with this rise in demand for wireless network access. Thus there is a need to create additional wireless bandwidth by not only improving utilization of current infrastructure but also exploiting additional spectrum.

Advances made in construction and manufacturing of solid state devices have created energy efficient LEDs. Lighting industry is rapidly adopting these devices for providing illumination in indoor spaces. Lighting fixtures are typically located to assist human activities and are thus uniquely positioned to act as access points. These trends have created a unique opportunity to utilize the unregulated optical spectrum and provide additional wireless network access.

This dissertation investigates MIMO OWC systems under illumination targets and improves upon the state of the art by better utilizing the spatial and color dimensions. Since the primary function of the luminaires is to provide illumination, incorporation of illumination targets while seamlessly providing wireless access is important for such systems to be practically adopted. Additionally indoor OWC systems must provide data rates equal to or greater than those provided by existing RF wireless technology to effectively mitigate the wireless bottleneck. Thus it is important to improve the

performance of optical modulation techniques and achievable spectral efficiencies by exploiting spatial and color dimensions.

Imaging receivers have been shown to reduce effect of shot noise on the optical communication channel (Djahani and Kahn, 2000). To analyze performance of OWC system with an imaging receiver, a novel receiver normalization framework is developed (Butala et al., 2014b). It is shown that incorporating an imaging receiver can improve performance of SM and SMP by up to 45 dB by effectively decorrelating the spatial streams. It is also shown that for an imaging OWC system at lower spectral efficiencies, SM performs better than SMP where as at higher spectral efficiencies, SMP performs better than SM.

SIS-OFDM, a spectrally efficient modulation technique has been proposed (Butala et al., 2014a). It improves upon the performance of modulation technique described in (Zhang et al., 2012) by carrying out SM on O-OFDM time domain samples rather than frequency domain subcarriers. This technique allows transmission of additional $3 \times N_{sc} \times k/4$ bits/symbol with ACO-OFDM and $(N_{sc}/2 - 1) \times k$ bits/symbol with DCO-OFDM where N_{sc} is total number of subcarriers and k is bits per underlying SM symbol.

LSNR, a metric to compare performance of different modulation techniques at the same illumination intensity levels is proposed. It is used to compare performance of CSK and MM.

Performance of CSK is studied under the linear system model as specified in the IEEE 802.15.7 standard (IEEE 802.15.7, 2011). Given the inherent non-linearity in human visual perception, a non-linear model for CSK is proposed. It is shown that the non-linearity causes performance penalties of 15 dB, 10 dB and 5 dB over the linear model for 4, 8 and 16-CSK when studied for CBCs specified in the standard. However there is scope for improvement by optimizing the CSK constellation for

skewed noise characteristics in the CIE-CS chromaticity plane.

MM has been proposed to provide OWC without data-dependent color flicker that may occur in CSK systems (Butala et al., 2012). MM always generates the true requested illumination color and has the potential to provide better color rendering. Performance of MM with different CBCs are compared and analyzed. It is shown that 4-MM with 6 LEDs forming CBC sets $\{1, 2, 4, 5\}$, $\{1, 2, 4, 6\}$, $\{1, 2, 4, 7\}$ and $\{1, 2, 4, 8\}$ outperform others.

An novel OWC system design using SVD techniques to combine illumination and communication information is described (Butala et al., 2013). It is shown that it is possible to achieve high data rate communications while maintaining requested illumination profile in indoor spaces. The system requires CSI to be known by the system adding some complexity.

A multi-wavelength OWC system design paradigm is also studied (Butala et al., 2014c). It is shown that as ICI increases, the most power efficient CCT shifts towards lower temperatures. Transmitting elements with smallest spectral spreads provide efficient communications. Filters with narrow FWHM reject a lot of signal power while those with wide FWHM accept a lot of interference.

As a part of smart lighting engineering research center, various prototypes and proof-of-concept demonstrations have been developed. CuSP, a color sensor platform was developed to support smart-room controls in indoor spaces. A prototype 4×4 MIMO OWC system was also specified in collaboration with university partners. 2×2 MIMO OWC system concept was prototyped and demonstrated.

References

- A. Yokoi, J. S. and Bae, T. (2011). Csk constellation in all color band combinations. Technical report, Samsung Electronics Co., Ltd.
- Armstrong, J. (2009). Ofdm for optical communications. *Lightwave Technology, Journal of*, 27(3):189 –204.
- Armstrong, J. and Lowery, A. (2006). Power efficient optical ofdm. *Electronics Letters*, 42(6):370 – 372.
- Azhar, A., Tran, T., and O'Brien, D. (2013). A gigabit/s indoor wireless transmission using mimo-ofdm visible-light communications. *Photonics Technology Letters, IEEE*, 25(2):171–174.
- Bai, B., Xu, Z., and Fan, Y. (2010). Joint led dimming and high capacity visible light communication by overlapping ppm. In *Wireless and Optical Communications Conference (WOCC), 2010 19th Annual*, pages 1–5.
- Baribeau, J. (2011). A lighting transformation, 2012 doe solid-state lighting r&d workshop. Technical report, US Department of Energy.
- Barry, J. R. (1994). *Wireless Infrared Communications*. Kluwer Academic Publishers, Norwell, MA, USA.
- Brown, W. R. T. and MacAdam, D. L. (1949). Visual sensitivities to combined chromaticity and luminance differences. *J. Opt. Soc. Am.*, 39(10):808–823.
- Butala, P., Chau, J., and Little, T. D. C. (2012). Metameric modulation for diffuse visible light communications with constant ambient lighting. In *Optical Wireless Communications (IWOW), 2012 International Workshop on*, pages 1–3.
- Butala, P., Elgala, H., and Little, T. D. C. (2014a). Sample indexed spatial orthogonal frequency division multiplexing. *Chin. Opt. Lett.*, 12(9):090602.
- Butala, P. M., Elgala, H., and Little, T. D. (2013). Svd-vlc: A novel capacity maximizing vlc mimo system architecture under illumination constraints. In *Globecom Workshops (GC Wkshps), 2013 IEEE*, pages 1087–1092.

- Butala, P. M., Elgala, H., and Little, T. D. (2014b). Performance of optical spatial modulation and spatial multiplexing with imaging receiver. In *IEEE WCNC'14 Track 1 (PHY and Fundamentals) (IEEE WCNC'14 Track 1 : PHY)*, Istanbul, Turkey.
- Butala, P. M., Elgala, H., Zarkesh-Ha, P., and Little, T. D. (2014c). Multi-Wavelength visible light communication system design. In *Globecom 2014 Workshop - Optical Wireless Communications (GC14 WS - OWC 2014)*, Austin, USA.
- Carruthers, J. and Kahn, J. (1996). Multiple-subcarrier modulation for nondirected wireless infrared communication. *Selected Areas in Communications, IEEE Journal on*, 14(3):538–546.
- Carruthers, J. and Kahn, J. (2000). Angle diversity for nondirected wireless infrared communication. *Communications, IEEE Transactions on*, 48(6):960 –969.
- Cisco VNI (2014). Cisco visual networking index: Forecast and methodology, 2013–2018. White Paper.
- Cossu, G., Khalid, A. M., Choudhury, P., Corsini, R., and Ciaramella, E. (2012). 3.4 gbit/s visible optical wireless transmission based on rgb led. *Opt. Express*, 20(26):B501–B506.
- Dissanayake, S., Panta, K., and Armstrong, J. (2011). A novel technique to simultaneously transmit aco-ofdm and dco-ofdm in im/dd systems. In *GLOBECOM Workshops (GC Wkshps), 2011 IEEE*, pages 782 –786.
- Djahani, P. and Kahn, J. (2000). Analysis of infrared wireless links employing multibeam transmitters and imaging diversity receivers. *Communications, IEEE Transactions on*, 48(12):2077–2088.
- Fath, T. and Haas, H. (2013). Performance comparison of mimo techniques for optical wireless communications in indoor environments. *Communications, IEEE Transactions on*, 61(2):733–742.
- Gancarz, J., Elgala, H., and Little, T. (2013). Impact of lighting requirements on vlc systems. *Communications Magazine, IEEE*, 51(12):34–41.
- Ganesan, S., Mesleh, R., Haas, H., Ahn, C. W., and Yun, S. (2006). On the performance of spatial modulation ofdm. In *Signals, Systems and Computers, 2006. ACSSC '06. Fortieth Asilomar Conference on*, pages 1825–1829.
- Goldsmith, A. and Varaiya, P. (1997). Capacity of fading channels with channel side information. *Information Theory, IEEE Transactions on*, 43(6):1986–1992.
- Grassmann, H. G. (1854). On the theory of compound colours. *Philosophical Magazine Series 4*, 7(45):254–264.

- Grubor, J., Randel, S., Langer, K.-D., and Walewski, J. (2008). Broadband information broadcasting using led-based interior lighting. *Lightwave Technology, Journal of*, 26(24):3883–3892.
- IEEE 802.15.7 (2011). IEEE Standard for Local and Metropolitan Area Networks—Part 15.7: Short-Range Wireless Optical Communication Using Visible Light. *IEEE Std 802.15.7-2011*, pages 1–309.
- Jain, A. K. (1989). *Fundamentals of Digital Image Processing*. Prentice Hall.
- Kahn, J. and Barry, J. (1997). Wireless infrared communications. *Proceedings of the IEEE*, 85(2):265 –298.
- Kahn, J., You, R., Djahani, P., Weisbin, A., Teik, B. K., and Tang, A. (1998). Imaging diversity receivers for high-speed infrared wireless communication. *Communications Magazine, IEEE*, 36(12):88 –94.
- Komine, T. and Nakagawa, M. (2004). Fundamental analysis for visible-light communication system using LED lights. *Consumer Electronics, IEEE Transactions on*, 50(1):100 – 107.
- Mesleh, R., Elgala, H., and Haas, H. (2010a). An overview of indoor ofdm/dmt optical wireless communication systems. In *Communication Systems Networks and Digital Signal Processing (CSNDSP), 2010 7th International Symposium on*, pages 566 –570.
- Mesleh, R., Elgala, H., and Haas, H. (2011). On the performance of different ofdm based optical wireless communication systems. *Optical Communications and Networking, IEEE/OSA Journal of*, 3(8):620 –628.
- Mesleh, R., Haas, H., Ahn, C. W., and Yun, S. (2006). Spatial modulation - a new low complexity spectral efficiency enhancing technique. In *Communications and Networking in China, 2006. ChinaCom '06. First International Conference on*, pages 1–5.
- Mesleh, R., Mehmood, R., Elgala, H., and Haas, H. (2010b). Indoor mimo optical wireless communication using spatial modulation. In *Communications (ICC), 2010 IEEE International Conference on*, pages 1 –5.
- Minh, H. L., O'Brien, D., Faulkner, G., Zeng, L., Lee, K., Jung, D., and Oh, Y. (2008). High-speed visible light communications using multiple-resonant equalization. *Photonics Technology Letters, IEEE*, 20(14):1243 –1245.
- Neumann, A., Wierer, J. J., Davis, W., Ohno, Y., Brueck, S. R. J., and Tsao, J. (2011). Four-color laser white illuminant demonstrating high color-rendering quality. *Opt. Express*, 19(S4):A982–A990.

- Park, K.-H., chai Ko, Y., and Alouini, M.-S. (2011). A novel power and offset allocation method for spatial multiplexing mimo systems in optical wireless channels. In *GLOBECOM Workshops (GC Wkshps), 2011 IEEE*, pages 823–827.
- Rahaim, M. and Little, T. D. (2015). Towards practical integration of dual-use vlc within 5g networks. *IEEE Wireless Communications*.
- Rajagopal, S., Roberts, R., and Lim, S.-K. (2012). IEEE 802.15.7 visible light communication: modulation schemes and dimming support. *Communications Magazine, IEEE*, 50(3):72–82.
- Roberts, R. (2013). A mimo protocol for camera communications (camcom) using undersampled frequency shift on-off keying (ufsook). In *Globecom Workshops (GC Wkshps), 2013 IEEE*, pages 1052–1057.
- Shannon, C. E. (1948). A mathematical theory of communication. *Bell System Technical Journal*, 27:379–423 and 623–656.
- Singh, R., O’Farrell, T., and David, J. (2013). Performance evaluation of ieee 802.15.7 csk physical layer. In *Globecom Workshops (GC Wkshps), 2013 IEEE*, pages 1064–1069.
- Tse, D. and Viswanath, P. (2005). *Fundamentals of wireless communication*. Cambridge University Press, New York, NY, USA.
- Tsonev, D., Chun, H., Rajbhandari, S., McKendry, J., Videv, S., Gu, E., Haji, M., Watson, S., Kelly, A., Faulkner, G., Dawson, M., Haas, H., and O’Brien, D. (2014). A 3-Gb/s Single-LED OFDM-Based Wireless VLC Link Using a Gallium Nitride μ LED. *Photonics Technology Letters, IEEE*, 26(7):637–640.
- Vucic, J., Kottke, C., Nerreter, S., Buttner, A., Langer, K.-D., and Walewski, J. W. (2009a). White light wireless transmission at 200+ mb/s net data rate by use of discrete-multitone modulation. *Photonics Technology Letters, IEEE*, 21(20):1511–1513.
- Vucic, J., Kottke, C., Nerreter, S., Habel, K., Buttner, A., Langer, K.-D., and Walewski, J. (2009b). 125 mbit/s over 5 m wireless distance by use of ook-modulated phosphorescent white leds. In *Optical Communication, 2009. ECOC ’09. 35th European Conference on*, pages 1 –2.
- Vucic, J., Kottke, C., Nerreter, S., Langer, K.-D., and Walewski, J. W. (2010). 513 mbit/s visible light communications link based on dmt-modulation of a white led. *J. Lightwave Technol.*, 28(24):3512–3518.
- Wandell, B. (1996). *Foundations of Vision*. Sinauer Press.

- Xu, T., Wu, Y.-K., Luo, X., and Guo, L. J. (2010). Plasmonic nanoresonators for high-resolution colour filtering and spectral imaging. *Nature Communications*, 1(59).
- Yokogawa, S., Burgos, S. P., and Atwater, H. A. (2012). Plasmonic color filters for cmos image sensor applications. *Nano Letters*, 12(8):4349–4354.
- Z. Ghassemlooy, W. Popoola, S. R. (2012). *Optical wireless communications: system and channel modelling with MATLAB®*. CRC Press.
- Zeng, L., O'brien, D., Le-Minh, H., Lee, K., Jung, D., and Oh, Y. (2008). Improvement of date rate by using equalization in an indoor visible light communication system. In *Circuits and Systems for Communications, 2008. ICCSC 2008. 4th IEEE International Conference on*, pages 678–682.
- Zeng, L., O'Brien, D., Minh, H., Faulkner, G., Lee, K., Jung, D., Oh, Y., and Won, E. T. (2009). High data rate multiple input multiple output (MIMO) optical wireless communications using white led lighting. *Selected Areas in Communications, IEEE Journal on*, 27(9):1654 –1662.
- Zhang, X., Dimitrov, S., Sinanovic, S., and Haas, H. (2012). Optimal power allocation in spatial modulation ofdm for visible light communications. In *Vehicular Technology Conference (VTC Spring), 2012 IEEE 75th*, pages 1–5.

Resume

Pankil M. Butala

pankil.butala@gmail.com

EDUCATION

Boston University, Boston, MA

2015

Doctor of Philosophy Candidate, Electrical and Computer Engineering

- Ph.D. Dissertation: Optical MIMO communication systems under illumination constraints.
- Developed low complexity spectrally efficient MIMO OFDM signaling schemes.

University of California, Los Angeles, CA

2007

Master of Science, Biomedical Engineering

- Designed multi-tap FIR/IIR digital filters.
- Developed java based GUI to parse DICOM images.

University of Mumbai, Mumbai, India

2006

Bachelor of Engineering, Biomedical Engineering

WORK EXPERIENCE

Multimedia Communication Laboratory & Smart Lighting ERC, Boston University, Boston, MA

2011 – 2015

Research Assistant

- Designed Xilinx FPGA based optical wireless 4x4 MIMO system with an imaging receiver and implementing OFDM variant as modulation at PHY.
- Developed a wireless, networked color sensor platform (CuSP) to deploy in smart spaces.
- Designed an iOS app and wireless, networked inertial sensors (FAM) for monitoring, detection and real-time classification of functional activity.

Advanced Analytical Technologies, Inc., Ames, IA

2009 – 2010

Software Engineer

- Developed GUI data analysis and controller software in C# for analytical laboratory instruments.
- Implemented real time control, digital signal processing, pattern search and match algorithms.

Enova Systems, Inc./HE-ITC, Torrance, CA

2007 – 2009

Software Engineer

- Developed embedded code in C/C++ for hybrid vehicle motor drive control modules.
- Developed an in house UI tool to obtain real time system diagnostic data.

PUBLICATIONS

- Trace-orthogonal PPM - Space time block coding under rate constraints for visible light communication 2015
Journal of Lightwave Technology, (33), 2, pp. 481-494
M. Biagi, A. M. Vigni, S. Pergoloni, **P. Butala** and T.D.C. Little
- Multi-wavelength visible light communication system design 2014
IEEE Globecom Workshop on OWC
P. Butala, H. Elgala, P. Z-Ha and T.D.C. Little
- Sample indexed spatial orthogonal frequency division multiplexing 2014
Chinese Optics Letters, (12), 9, pp. 090602
P. Butala, H. Elgala and T.D.C. Little
- Performance of optical spatial modulation and spatial multiplexing with imaging receiver 2014
IEEE Wireless Communications and Networking Conference
P. Butala, H. Elgala and T.D.C. Little
- SVD-VLC: A novel capacity maximizing VLC MIMO system architecture under illumination constraints 2013
IEEE Globecom Workshop on OWC
P. Butala, H. Elgala and T.D.C. Little
- Metameric modulation for diffuse visible light communications with constant ambient lighting 2012
International Workshop on OWC
P. Butala, J. Chau and T.D.C. Little
- Monitoring walking and cycling of middle-aged to older community dwellers using wireless wearable accelerometers 2012
Annual International Conference of the IEEE EMBC
Y. Zhang, K. Beenakker, **P. Butala**, C. Lin, T.D.C. Little, A. Maier, M. Stijntjes, R. Vartanian and R. Wagenaar
- Wireless system for monitoring and real time classification of functional activity 2012
Fourth International Conference on COMSNETS
P. Butala, Y. Zhang, T.D.C. Little and R. Wagenaar